Ilkka Pöllänen

THE EFFICIENCY AND DAMAGE CONTROL OF A RECOVERY BOILER

ACTA UNIVERSITATIS LAPPEENRANTAENSIS 892

Ilkka Pöllänen

THE EFFICIENCY AND DAMAGE CONTROL OF A RECOVERY BOILER

Dissertation for the degree of Doctor of Science (Technology) to be presented with due permission for public examination and criticism in the Auditorium 1318 at Lappeenranta-Lahti University of Technology LUT, Lappeenranta, Finland on the 16th of December, 2019, at noon.

Acta Universitatis
Lappeenrantaensis 892

Supervisor Professor Timo Björk
LUT School of Energy Systems
Lappeenranta-Lahti University of Technology LUT
Finland

Reviewers Professor Raimo von Hertzen
Department of Mechanical Engineering
University of Aalto
Finland

Professor Danny Tandra
Department of Mechanical Engineering
University of Toronto
Canada

Opponents Professor Raimo von Hertzen
Department of Mechanical Engineering
University of Aalto
Finland

Associate professor Mika Järvinen
Department of Mechanical Engineering
University of Aalto
Finland

ISBN 978-952-335-476-0
ISBN 978-952-335-477-7 (PDF)
ISSN-L 1456-4491
ISSN 1456-4491

Lappeenranta-Lahti University of Technology LUT
LUT University Press 2019

Abstract

Ilkka Pöllänen
The efficiency and damage control of a recovery boiler
Lappeenranta 2019
112 pages
Acta Universitatis Lappeenrantaensis 892
Diss. Lappeenranta-Lahti University of Technology LUT
ISBN 978-952-335-476-0, ISBN 978-952-335-477-7 (PDF), ISSN-L 1456-4491,
ISSN 1456-4491

Recovery boilers are needed to produce sustainable energy from sideline by-products of the biomass processing industry. Customers need boilers which have a reliable, long operation time without unnecessary shutdowns and with minimal cleaning costs of the heat surfaces. Sootblowing, i.e. removal of deposits from the recovery boiler heat surfaces, is critically important for a cost effective operation. This thesis is focused to develop a measurement device to predict the need for sootblowing by using the ash weight change information from the heat surfaces. The measurement devices are assembled parallel with hanger rods and they transform the measured strain values to ash weight values and deliver them further to the control system of the recovery boiler for monitoring. Measurements using the above mentioned devices have been done at the site and in the laboratory. The results obtained have been verified using analytical and numerical methods. Both results agree satisfactorily well.

The sootblower causes an excitation to the heat surface, when its steam jet hits the surface. This can lead to harmful vibrations of the platen and, furthermore, to fatigue failures. The theoretical objective is to create a costly effective calculation method which produces adequate information to determine fatiguing loads due to sootblowing. The developed cost-effective calculation method gives an opportunity to estimate the effect of the chosen sootblowing sequence to the fatigue durability of the structure.

Keywords: Recovery boiler, superheater, ash measurement, dynamic analysis, fatigue

Acknowledgements

This work has been carried out at the Department of Mechanical Engineering at Lappeenranta University of Technology, Finland, between 2014 and 2019.

This process from the beginning to the end has had a considerable role in my daily work as design engineer. I want to thank my supervisor, Professor Timo Björk, for his time and guidance to help me to improve the contents of the text. Furthermore, I want to express my deepest gratitude to the preliminary examiners and reviewers Professor Raimo von Hertzen and Professor Danny Tandra for their valuable contribution and comments.

I also want to express my great appreciation to the following people for their support and technical advices: Professor Heikki Martikka for his guidance and advice throughout the work, Mr. Jari Lindroos for his comments concerning grammar, Dr. Eerik Peeker for expertise in signal processing of data acquisition systems, Dr. Juha Kilkki for his valuable comments and advices in programming, Professor Esa Vakkilainen for his special understanding of the boiler process, Mr. Antti Ahola and Dr. Tuomas Skriko for their valuable comments concerning fatigue and Mr. Heikki Lappalainen for giving me the opportunity to make required field measurements at the site.

Thank you Päivi for your support and my children Siiri, Sanni, and Simo for your patience during these years.

Furthermore, I want to thank many of my colleagues for valuable comments and all those with whom I have had the pleasure to work during this project.

Ilkka Pöllänen
December 2019
Lappeenranta, Finland

Contents

Nomenclature

Latin alphabet

A	area, factor	mm^2, –
b	notation, width	–, mm
c	notation	–
C_o	constant	$\frac{mm/cycle}{(MPa\sqrt{m})^m}$
d	notation	–
E	Young's modulus	MPa
F	force, attention factor	N, –
G	shear modulus	MPa
I	second moment of area	mm^4
k	spring constant	N/mm
K_a	stress intensity factor	–
L	length	mm
M	moment	Nmm
N	factor of reliability	–
P	force	N
Q	shear force, factor	N, –
R, r	resistance, radius	Ω, mm
Re	yield strength	MPa
T, t	thickness, temperature	mm,°C
U	potential energy	J
x	x-coordinate, variable	mm, –
Y, y	factor, y-coordinate	–, mm
Z, z	safety margin, z-coordinate	–, mm

Greek alphabet

Δ	range	–
δ	displacement	mm
ε	strain	–
$\boldsymbol{\epsilon}$	error vector	–
θ	angle, flank	^{0}
Σ	sum	–
σ	normal stress	MPa
Ø	diameter	

Superscripts

m	material exponent

Subscripts

anal	analytical
b	bending
eq	equivalent
f	final
FEA	finite element analysis
hr	hanger rod
hs	hot spot
HT	at elevated temperature
i	initial
inn	inner
m	membrane
meas	measured
nom	nominal
nl	nonlinear
nlp	nonlinear peak
o	outside
out	outer
r	radius
s	structural
theor	theoretical
wf	weight function

Abbreviations

AI	artificial intelligence
CaO	lime
Cf	correction factor
CFD	computational fluid dynamics
CH_4	natural gas
Cl	chlorine
DAQ	data acquisition system
DCS	distributed control system
DE	differential evolution algorithm
DN	diameter nominal
ENS	effective notch stress
FAT	fatigue class
FE	finite element
FEA	finite element analysis
FEM	finite element method
LEFM	linear fracture mechanics
FFT	fast Fourier transformation
EN	European norm
GF	gage factor

M_a	weight function for the intensity factor
Na	sodium
NaOH	sodium hydroxide
Na_2S	sodium sulphide
Na_2SO_4	sodium sulphate
Na_2CO_3	sodium carbonate
O_2	oxygen
OLS	ordinary least squares method
PAD	pulsed amperometric detector
RBDA	recovery boiler dust analyzer
SPG	shock pulse generator
SG	strain gage
SO_4	sulphate
SIF	stress intensity factor
WF	weight function

1 Introduction

Recovery boilers are widely used as essential process components in the pulp manufacturing industry (Krotscheck & Sista, 2006). A recovery boiler is designed to perform several functions at the same time. Firstly, in a recovery boiler the combustion of the organic compounds of black liquor takes place. Secondly, the generated combustion heat is used to produce steam. The steam can be used further in the processes or for electric power production. Thirdly, pulping chemicals containing sulphur and sodium released from black liquor are recovered to the process. They are utilized as suitable compounds for further treatment in the chemical circulation loop (Gullichsen & Fogelholm, 2000).

The thermal efficiency of a boiler is at its maximum and the cost of the boiler is at its minimum when the deposit layer on the boiler heat surfaces, preventing heat transferring to steam, is kept minimal (Capablo & Salvadó, 2016). In recovery boilers, the deposits gain strength and thickness if they are allowed to grow uncontrolled (Frederick, et al., 2003). This observation supports the need for a real time deposit removing mechanism built into the structure. Left unchecked, these deposits sinter to form a strong and brittle deposit. During the sintering process these deposits gain strength, and in some instances can even render the improved nozzles ineffective (Mao, et al., 2001a). In the worst case the deposit layers can become so thick, that the sootblowers cannot remove the accumulated layers anymore, which leads to plugging of the heat surfaces and shut down of the recovery boiler. This decreases the pulp mill production and causes economic losses.

It has been estimated by using heat transfer models (Nschokin, 1979) that a 10 mm deposit layer may decrease the useful heat extraction by 10% or even more. Therefore, one of the most important activities for maintaining a high efficiency of the steam production is to remove the insulating deposit layers cost-effectively. This removal is done in most boilers using a steam jet to blow the deposit away with an optimal combination of steam jet volume and jet force. Significant steam savings can be achieved if the location of the ash on the heat surfaces is known. Then, the sootblowers can be oriented to clean only these beforehand determined, problematic areas on the heat surfaces. The saved steam can be used in other processes, such as electricity production.

A forceful flow removes the deposited ash efficiently, but it can cause harmful vibrations of the heat surfaces. In certain circumstances the tube stress response to these dynamic load excitations may become very extensive, increasing the risk of safety critical fatigue failures of a recovery boiler. Water leaks occur most frequently in the heat surfaces and, especially, in the tube joints. In present practice, the structure is designed only against static loads, while fatigue loads are ignored due to insufficient data on the loadings.

In this study it is shown that, based on proper measurements and calculations, the ash deposit distribution in the horizontal direction on the heat transfer platens can be determined, and an optimal sootblowing operation arranged. The dynamic loads obtained can be used to predict and control the fatigue endurance of the tube branch joints to obtain a long total lifetime for the recovery boiler.

1.1 Description of kraft pulping process

Cellulose pulp is used as raw material for paper and kraft manufacturing. The pulp production process begins with the handling of raw materials in the wood yard. In the chipper, rotating discs cut logs into small chips, which are then transferred by conveyors to the digester for cooking. To separate wood fibers and to partially dissolve the lignin and other extracts, the wood chips are impregnated with weak black and white liquor and simultaneously heated approximately to +140-170 °C using steam at a specific pressure to dissolve lignin and other compounds that hold cellulosic fibers together. After digestion the pulp is washed and fibers are separated. The residual flow is called black liquor. The brown pulp is further bleached to obtain its characteristic white color. The last phase of the pulp production process consists of drying and baling for shipment, or pumping it in a slurry form for further processing in the paper mill.

The weak black liquor separated in the washer is stored in storage tanks. On average, half of the wood in the raw material ends up in the black liquor. The weak black liquor is high in water content and as such can´t be used directly as a fuel in a recovery boiler. In the evaporation unit the dry solids content of the black liquor is increased by evaporating the excess water. The final concentration is usually 75% - 80% solids, which is required for efficient combustion in a recovery boiler. The dry solids content includes both the wooden raw material and cooking chemicals. The concentrated black liquor is sprayed into the lower part of the recovery boiler furnace by liquor guns. The droplets go through one evaporation and two combustion stages. In the first stage, the droplets dry rapidly in the hot combustion gas and lose their remaining moisture. Then, the dry material passes through the first volatiles release stage and releases various gaseous compounds which are combusted and form flue gas. In the third stage, the remaining char burns partly and the remaining material falls onto a char bed at the bottom of the recovery boiler furnace. (Vakkilainen, 2006a)

In the recovery process the spent cooking chemicals in weak black liquor are converted to active alkali, sodium hydroxide (NaOH) and sodium sulphide (Na_2S). The recovery boiler is designed to convert sodium sulphate (Na_2SO_4) into sulphide (Na_2S). This can be achieved by maintaining a reduced atmosphere in the char bed. The reacted chemicals inside the char bed are in a molten phase and form a melt. The melt exits through the melt spouts into a dissolving tank where it is mixed into the weak white liquor to form green liquor. Next the green liquor is pumped into the causticizing plant, where it reacts with lime (CaO) to convert sodium carbonate (Na_2CO_3) to sodium hydroxide, also known as caustic soda (NaOH) (Vakkilainen, 2006b).

A recovery boiler needs constant cleaning to maintain good heat recovery and high capacity. Plugging of the heat transfer surfaces due to ash deposit accumulation can cause expensive unscheduled shutdowns. The accumulation can be controlled by sootblowers. These devices have rotating lance tubes, which move back and forth while simultaneously spraying steam jets through two nozzles near the tip of the lance (Tandra, et al., 2010). The steam jets hit the deposits and blow them off the boiler tube surfaces. The operating pressure is typically between 20 and 30 bars. The steam consumption of the sootblowers is approximately 2-10 kg/s depending on how many sootblowers are operated simultaneously. This means 2 – 10% of the total amount of the superheated steam generated by the boiler. An ideal sootblowing operation blows away all deposits using an optimal amount of steam.

1.2 Deposit removal from recovery boiler tube surfaces

In order to optimize the need for sootblowing of the recovery boilers, efforts have been made over the years to develop methods based on different measurement methods. At present, a common practice is to measure the steam, water and flue gas temperatures and the flue gas pressure drops (Frederick & Vakkilainen, 2002).

Currently, the best way to estimate the need for sootblowing is the so-called intelligent sootblowing application from DCS (Distributed Control System) vendors, using process-measured quantities such as temperature and pressure with calculations. Information provided by these indirect measurements, however, give only limited data on the success of the deposit removal operation as only coarse data for large sections can be obtained. The effectiveness of the cleaning can be improved by, e.g., adding a measurement system for the mass change of the individual superheater heat transfer platens.

1.2.1 Targeted sootblowing

The objective of targeted sootblowing is to control the sootblowers in such a way that the heat surfaces stay clean and prevent plugging of the boiler. This leads to higher boiler efficiency, minimal usage of deposit removal steam, and longer running times without unnecessary shutdowns. The trend in sootblowing technology is to develop intelligent and accurate methods for guiding the cleansing to the right target at the right time.

There are several methods to estimate the overall need for deposit cleaning for the boiler. One drawback is that these methods do not indicate accurately enough the locations needing immediate cleaning.

In intelligent sootblowing different physical quantities are measured from the boiler. These are, for example, temperature and pressure differences from different locations of the boiler, and the amount of dust as well as its consistency.

Differences between the inlet and outlet temperatures of the heat surfaces tell how efficiently heat is transferred from the combustion gases to the heat surfaces. Similarly, the magnitude of the pressure differences allows one to estimate the risk of plugging in certain spots of the boiler.

A specific software is used to process the data obtained from the measurements. This software is able to describe the process using given starting data and measured results. Information on how and where sootblowing should be done to ensure the highest possible heat exchange rate is obtained as a result of these calculations.

One typical method utilizes a continuous measurement of the flue gases. Important information for decision can be obtained from the mass concentration and chemical composition of the flue gases. Elements of interest are sodium (Na) and chlorine (Cl). The measurement system consists of a suction probe inserted inside the flue gas duct and a vacuum pump for introducing a sample into the on-line dust analyser. The results of an analysis yield the total dust concentration and chemical composition of the flue gases. The measurement system has a high sensitivity to dust concentrations (g/m^3) and chemical compositions in a wide range of flue dusts from combustion processes. The analysis of the results revealed that during deposit removal the dust concentration rises 5-6 times higher compared to the case of no deposit removal. By combining information from dust concentration output and sootblowing sequence history it is possible to determine almost optimal sootblowing sequences for heat transfer surfaces in order to get maximal dust removal. Because the removed dust has a tendency to reattach, this method does not provide reliable information on e.g. superheater surface cleanliness. (Tamminen, et al., 2001).

1.2.2 **Damages on the heat surfaces**

Less attention has been paid on the durability fatigue analysis of the heat surfaces, caused by the dynamic loads due to e.g. sootblowing. The design of the heat surfaces has been conventionally based on almost solely on the static dimensioning of pressure loaded elements according to the corresponding standards. This design convention has resulted in using the same standard size tubing and shapes even in safety critical tubing areas.

This has resulted in costly fracture induced leaks and repairs. These problems could have been prevented by optimal re-designs of a few safety critical tubing assemblies. Now, when the global trend in boiler construction is to enlarge the size of the boiler and, simultaneously, achieve lighter structures and higher total efficiency, the need of improved design is obvious.

Fractures of the heat surface tubes constitute a common damage in recovery boilers. The fractures can occur at certain platen tubes running to tube branch joints. Fractures cause water leaks into the furnace.

These have long known to cause dangerous explosions due to sudden vaporization of water (Nelson, et al., 1996). In the report (Ortega & Bécar, 2008) failures of the heat surface tube joint welds in the lower chambers are described. According to the report, the fractures occur at the weld and their peripheral lengths range from one third to a complete revolution. The report does not indicate any reasons for the fractures.

A direct observation of the locations of highest fracture risks with a combined steam leak is not technically feasible. At present, their existence may be only indirectly concluded by analysing their influence on the overall process parameters. Weld fractures of the tube allow the water circulating in the heat surface tubing to leak into the combustion chamber causing an explosion risk.

One possible cause for the fractures may be the loads generated by the flue gases and the sootblowing jet forces acting excessively on the heat surfaces. These load excitations raise damaging vibration responses. Another possible cause can be unexpected time varying support conditions at the lower end area.

The platen tubes are joined to the feeder which may act as a torsional tubular spring. This may shift some eigenfrequencies closer to resonance frequencies in the location of the damaged tube joints. The first and second eigenmodes are bending modes, while the third one is a torsion mode (Pöllänen, et al., 2015). Even if the lower support is nearly a revolute joint with ideally zero bending moment, bending moments occur further from the revolute joint due to tube curvature. If the platens are vibrating at the torsional mode, torsional moments are generated which cause variable bending moments at the tube joints. The approach in this thesis is based on FE- modelling, analytical calculations and the measurement system.

1.3 Goals and methods

The main goal of this thesis is to develop a measurement device to predict the need for sootblowing by using the ash weight change information from the heat surfaces. The first subgoal is therefore to design, construct and test a device for measuring reliably the ash accumulations on heat transfer surfaces via support rods in real time. The second subgoal is to create a calculation method which is user friendly and which produces adequate information from the dynamical behaviour of the platens to determine fatiguing loads due to sootblowing. The third subgoal is to increase the fatigue life of the tube branch joints. Since it depends on the product of stress concentration factor and nominal maximal stress, the aim was set to obtain stress concentration models depending on the dimensionless main design variables defined as the diameter and wall thickness ratios of the header and branch pipe. A general view of the issues related to sootblowing is presented in Figure 1.1.

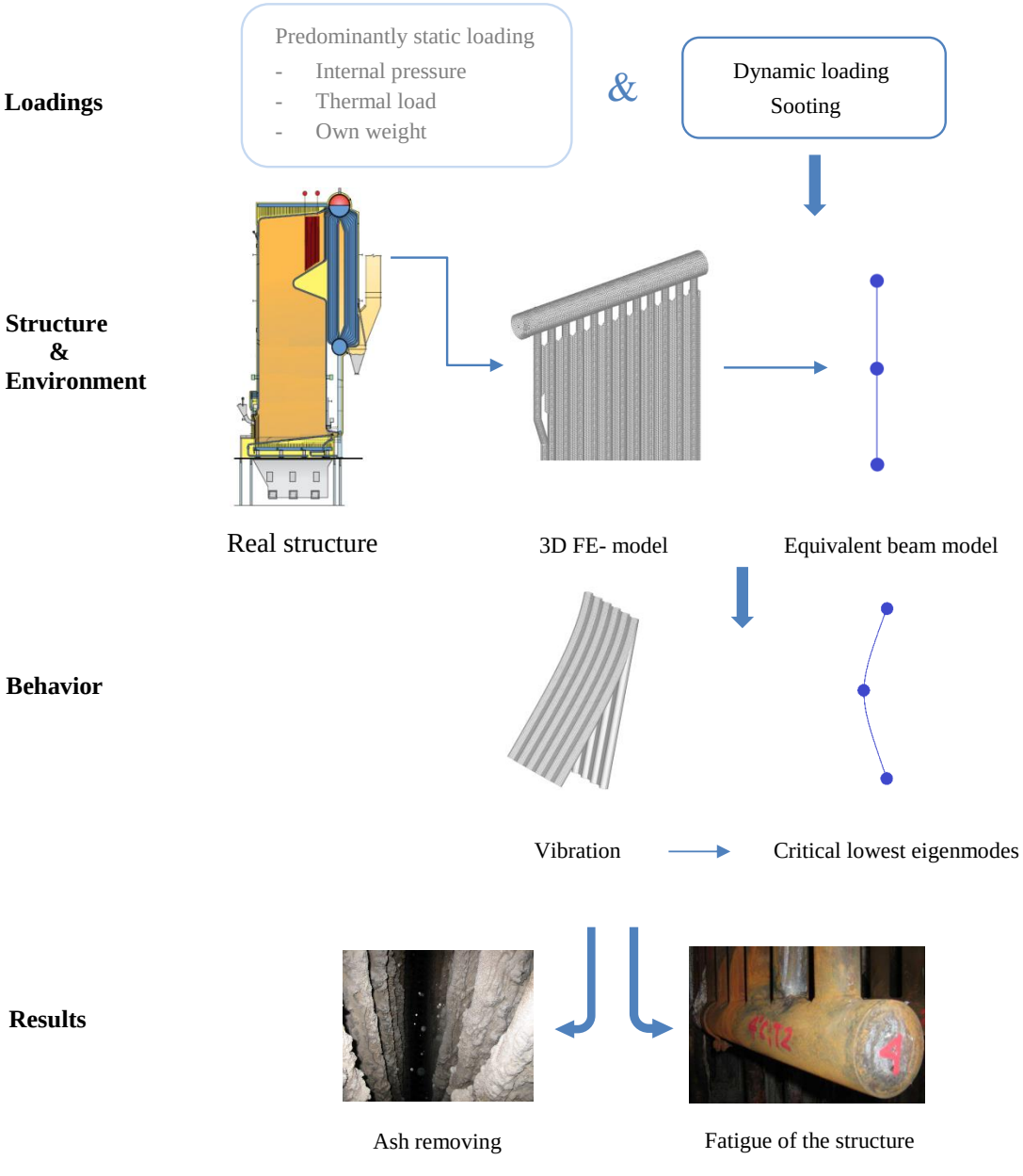

Figure 1.1: A flow sheet of the challenges due to sootblowing.

1.4 Scientific Contribution

The main objectives of this thesis were to find methods to reduce downtime, damages and costs associated with the fouling of the heat transfer surfaces of recovery boilers. The obtained results and scientific findings of the work are clarified using the following question and answer procedure:

The aim of the soot blowing operation applied to the heat transfer surfaces of a recovery boiler is to remove a certain amount of ash. This amount is correlated with the success of the soot blowing. The measurement of the amount of soot mass is very challenging in the aggressive environment of the furnace due to its high temperature and falling soot mass particles. Is it possible to measure the amount of ash on the heat transfer surfaces from the structure outside the furnace?

The goal is to develop a new measurement device to predict the need for sootblowing by using the ash weight change information from the heat transfer surfaces, and to control the efficiency of the sootblowing. This device can be connected to the hanger rods of a recovery boiler and it can transform the rod elongations to an equivalent ash weight value.

Is the performance of the measurement device adequate for real time monitoring of the sootblowing?

The goal is to investigate whether the ash accumulations on the heat transfer surfaces can be reliably measured via hanger rods in real time using the developed device. The device is equipped with strain gauges and Wheatstone bridge and the signal obtained can be monitored in real time.

When the steam jet of a sootblower hits the heat transfer surfaces they start to vibrate. Excessive soot blowing jet forces can cause serious fatigue damages to the tube branches. In view of these deleterious scenarios some questions can be posed.

What is the influence of different soot blowing sequences in causing or preventing fatigue damages? Is it possible to increase the fatigue durability at the critical branch joints on the heat transfer surfaces?

The goal is to study the dynamical behaviour of the heat transfer platens subject to fouling, in order to determine fluctuating loads due to sootblowing. Due to the complexity of the structure, numerical methods are used to get answers to the above mentioned challenges.

It is well known that a complete and detailed FEA with shell or solid elements of a heat transfer surface is very time-consuming and tedious. It is known that simplified FEA models may give a satisfactory accuracy with much less labour.

Are the results obtained with the simplified FEM model developed in this work accurate enough? Is it possible to obtain a loading history accurate enough for the fatigue calculations?

The goal is to create a new concept to control simultaneously both the efficiency of the sootblowing as well as the fatigue of the critical parts of the heat transfer surfaces by replacing the complicated structure of the heat transfer surface by an equivalent beam model.

There are many alternatives to manufacture the tube joints by using different geometric variables, such as the tube diameter or thickness. Is it possible to find an optimal solution in terms of lowest stress concentration factor among several design parameters?

The goal is to develop a new calculation method for stress concentration evaluation utilizing the dimensionless main design parameters defined as the diameter and wall thickness ratios of the header and branch tube. This can be used to predict the fatigue life of the structure by the aid of the stress concentration factor and nominal maximal stress.

What is the influence of the tube branch cross section and its shape on the fatigue durability of the tube joint?

The goal is to come up with new types of tube joints to increase the fatigue life of the tube branch connections. Based on the research results of this work, a non-circular cross section of the branch tube can be used to improve its fatigue durability under certain circumstances.

1.4.1 Literature review

Several methods have been developed for solving fouling and plugging problems of the recovery boilers. A widely used method (Tamminen, et.al., 2001), (Välimäki & Salmenoja, 2004) is based on a continuous measurement of the composition (K, Cl) of the dust and it's amount in the flue gas. It was found that the amount of dust due to sootblowing depends on the dust composition and operation conditions. This information can be used to estimate the effectiveness of different sootblowing strategies.

The effectiveness of the sootblowing can be described as a capability of removing brittle deposits by sootblowing (Kaliazine, et.al., 1997), (Pophali, et.al., 2013). According to experimental tests the pressure of the steam jet has a very important role in determining the sootblower efficacy. This information is useful when discussing the savings of the steam consumption.

The behaviour of a steam jet is a strongly nonlinear problem and it is difficult to find a closed form solution. In practice, only numerical modelling methods (CFD) are available (Doroudi, et.al., 2015). This method has been used to develop more complex models describing the interaction of the jet and the tube. The goal is to maximize the deposit removal by a minimum amount of steam (Moskal, et.al., 1997).

Swedish Värmeforsk (Thermal Engineering Research Insitute) has studied sootblowing in all 14 Swedish recovery boilers. The goal was to explain differences in cleanability and sootblowing efficiency. They found that it is difficult to identify the relation between cleanability and the sootblowing systems. In the report some findings and relations are mentioned. Four recovery boilers are equipped with an intelligent soot blowing system. Two of them have a low and the other two a high availability. This difference was explained by varying conditions. They observed that the sooting sequences can be used to improve the efficiency of the recovery boiler (Svedin, et.al., 2008).

The force caused by a steam jet has been studied by two field measurements of recovery boilers in Sweden (Miikkulainen, 2011). This study is based on the previous research work "Measurement of sootblower jet strength in kraft recovery boilers by Tran et.al." The field measurements confirmed the results of the preliminary findings. The results showed that the jet force increases nearly linearly with respect to the lance pressure.

The results of the sootblowing depend a lot on the location of the accumulated ash. Typically, in the superheater section, it can be difficult to remove deposits using conventional sootblowers (Tandra & Jones, 2010). The function of conventional sootblowers is based on the brittle break-up mechanism. New sootblower design takes into account both the brittle break up and debonding mechanisms, which improves the removing of the deposits.

However, there are no widely used measurement methods, that can measure reliably ash mass changes on the heat surfaces from the external supporting system of the platens. In this work, a new measurement device for ash mass changes, and a method for estimating the effect of the sootblowing sequences on the fatigue durability of the branch connections, are presented.

The author of this thesis has studied ash weight measurements and dynamic behavior of the heat transfer surfaces in the related publications:

- Pöllänen, I., Martikka, H. (2009). Design of process equipment beam joints to withstand creep and fatigue – International Conference on Processing, Fabrication, Properties, Applications. *Technical University- Berlin, Germany.*

- Martikka, H., Pöllänen, I. (2009). Multi-objective optimization by technical laws and heuristics – *Memetic Computing, Volume 1, Number 3 / November 2009, pp. 229-238.*

- Martikka, H., Pöllänen, I. (2005). Optimal design of fatigue loaded piping branch connections. *Computer aided optimum design in Engineering IX. WIT Press, Southampton, Boston, pp. 391-400.*

- Pöllänen, I. (2008). Beam joints under stress relaxation. *Machine Design 2009, pp. 255-260.*

- Martikka, H., Pöllänen, I. (2013). Beam dynamics design using analytical methods for optimizing heat transfer plates dynamics behavior. *Mechanical Engineering Research, Vol 4, No.1.*

These publications have laid the foundations for this thesis and have given a deeper understanding of the above issues.

1.5 Limitations of the scope of the thesis

The present field of research is broad and multidisciplinary. The following subjects are outside the scope of this work:

- Vertical mass distribution of the ash deposit on the heat surfaces. It is not possible to obtain this information on the basis of present measurements.
- Thermal fatigue is excluded, because thermal expansion of the platens is not restricted and they can move freely in vertical and horizontal directions.
- The real excitations caused by sootblower jets on the heat surfaces are not considered here. They can be measured with special apparatus. This task has been initiated.
- Influence of the combustion gas flow in the fatigue analysis is also excluded.
- Corrosion in the furnace.
- Chemical reactions, as burning in the furnace.

2 Research methods

From the point of view of a boiler user the most undesirable malfunction of a recovery boiler may lead to its shutdown causing significant economic losses. There are many reasons for shutdowns, but this thesis is focused on two main reasons.

One reason for shutdown is the fracture of some critical branch tube joint of a heat surface. The reason discussed here is fatigue fracture due to dynamic loading, caused by an excessive sootblowing jet force and internal gas vibrations. The remedy is to analyze the jet impact excitation and adjust the force to a safe level. A too small force will not clean enough, whereas a too large force may cause fatigue fractures.

The second reason for shutdowns is plugging of the recovery boiler. The gas flow in the channel between heat transferring tubes is blocked and heat transfer is reduced. During normal operation, ash is accumulated on the heat surfaces and it has to be removed or at least reduced by sootblowing before plugging.

Prevention of these events can be done by two means. One is to control the jet force. The second is to obtain information on momentary maximal soot accumulations and to guide the soot blowing robot right on the target. Thus, steam is not wasted on surfaces which are sufficiently clean but concentrated on the largest pluggages before they plug a channel.

Evaluating the result of the sootblowing is difficult to do with internal measurements due to a high temperature in the furnace. In most cases this restricts the use of internal measurement devices. An alternative way to evaluate the results is to measure axial forces in the hanger rods. By equipping hanger rods with measurement devices, a good understanding of the ash mass changes on the heat surfaces can be obtained. In this work, an innovative measurement device, developed for the axial force measurement of the hanger rods, is presented.

A good approximation of the dimensions of the measurement device can be achieved by analytical calculations based on the assumption of linear behavior of the measurement device. This is a realistic assumption, because the axial displacements in the hanger rods are very small during normal operation. An essential part of the preliminary design is to search out existing designs for this kind of devices. These are very inspiring and perhaps include similar solved problems.

The use of FEM is necessary to confirm the analytical results. A complete finite element analysis (FEA) gives more detailed information to improve the performance and reliability of the structure, and it shows possible deficiencies in the hand calculations. It also reduces the number of prototypes needed and, therefore, saves a lot of testing efforts.

The next step is the decision of manufacturing of the prototype and testing. Preliminary testing provides more information about the behavior of the real measurement device, and the obtained information allows us to update the preliminary calculations more accurate.

Full scale testing will be done after testing the prototype. Field measurements at site require several important arrangements such as safe working on the top of the recovery boiler and a plan of the assembly of the measurement devices. A connection between the DAQ (Data Acquisition System) of the measurement device and the DCS of the mill needs a very careful planning to avoid unnecessary interference in the DCS.

Occasional fatigue failures in the heat surfaces are a common reason for shutdowns. They can occur very quickly after the first startup, or after a long period of use. The location of the failure occurs typically at the junction of the header. In some circumstances the heat surface can vibrate due to sootblowing causing fatigue. The magnitude of the loadings can be evaluated by using a simulated time history analysis. The durability of the branch connection can be calculated using LEFM (Linear Fracture Mechanics), (Anderson, 2005; Schijve, 2009) and ENS (Effective Notch Stress approach), (Radaj, 2006).

3 Fouling and damages of the heat transfer surfaces

The aim of this section is to describe the basics of the heat transfer surface fouling by deposit and methods of controlling it. The burning of black liquor generates ash, which covers the heat transfer surfaces with insulating deposit layers preventing heat transfer and lowering the energy production efficiency. Consequently, there is a need to control the thickness of the deposit layer. The ash accumulated on the heating surfaces can be removed by several methods. Typically, deposit removal is done by sootblowing robots. Presently, only overall measurements are made in industry. These measurements provide information on the distribution of temperature, pressure and chemical composition of the combustion gases. This information is too general for the needs of target cleansing.

3.1 Fouling prevention and cleaning methods

The black liquor used as fuel in recovery boilers has a high ash content with low melting point, and the fly ash released by its combustion easily attaches on the heat transfer surfaces. The ash accumulating on the heat transfer surfaces becomes an insulator and prevents the transfer of heat from the flue gases to the circulating medium. The deposits on the heat transfer surfaces can grow and become so extensive that the velocity of the flue gases between the heat transfer surfaces increases, which subsequently leads to an increase in the pressure losses. In the worst case, the boiler will be clogged with ash and has to be shut down. This causes loss of production and financial losses.

Three main factors have an impact on the fouling of the heat transfer surfaces: the amount of particles, their adhesion properties, and how often the heat transfer surfaces are cleaned. When the heat transfer surfaces are kept as clean as possible, the process is optimised, which naturally has a direct impact on the financial costs. It should also be noted that issues such as the adhesion properties of ash depend to a large extent on the properties of the liquor and raw materials of the mill, and can be hardly influenced. Fouling is also beneficial, because the dust causing fouling also reacts with the sulphur dioxide in the flue gases, reducing the emissions of the boiler.

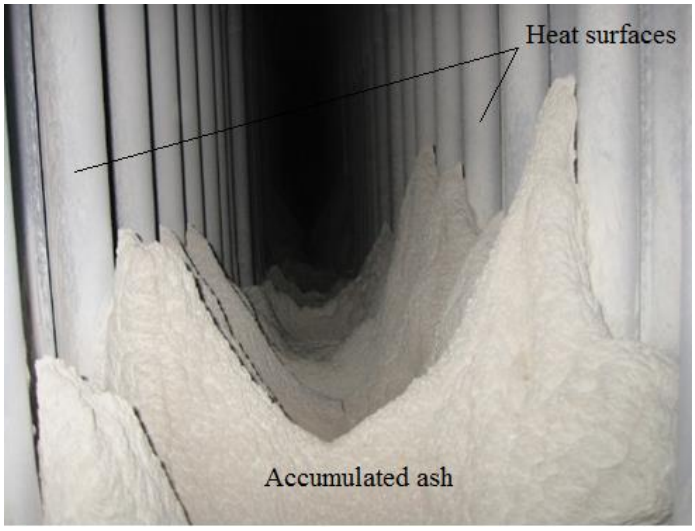

Figure 3.1: Ash deposits on the heat transfer surfaces.

In the colder parts of the boiler, such as in the economiser and on the boiler bank, very fine dust generated by combustion tends to accumulate on these surfaces through various deposition mechanisms, initially forming soft deposits. Over time, the deposits accumulating on the surfaces harden and sinter into crystalline layers which are difficult to remove. If the cleaning interval is kept shorter than the sintering period, the amount of ash removed can be about the same as the amount accumulating on the surfaces between the cleaning cycles. (Jameel, et al., 1994)

Cleaning can be performed in a number of ways. The best known methods are steam cleaning, acoustic cleaning and gas pulse cleaning.

Steam cleaning is by far the most common method for cleaning the heat transfer surfaces. The steam used in a steam sootblower is taken directly from the turbine or from high-pressure steam through a reduction valve, where the pressure of the high-pressure steam (approx. 100 bar) is reduced to 20-30 bar. The temperature of the steam used for cleaning is about 50-100 ^{o}C higher than the temperature of the corresponding saturated steam. This prevents the erosion wear of the heat transfer surfaces caused by hitting of water droplets.

The steam sootblower consists of a lance tube with two opposing nozzles mounted near the tip of the lance. During cleaning, the velocity of the steam in these nozzles is higher than the speed of sound.

The jets hit the deposit, breaking up and removing it from the tube surface. During cleaning, the lance of the sootblower rotates and pushes forward in the cleaning passage.

The length of the lance tube can be as much as 16 metres, and its length is limited by its bending downwards due to gravity. After the lance is fully inserted, it's direction of rotation will be changed and the lance retracts back to its original inactive state. (Kaliazine, et al., 1997)

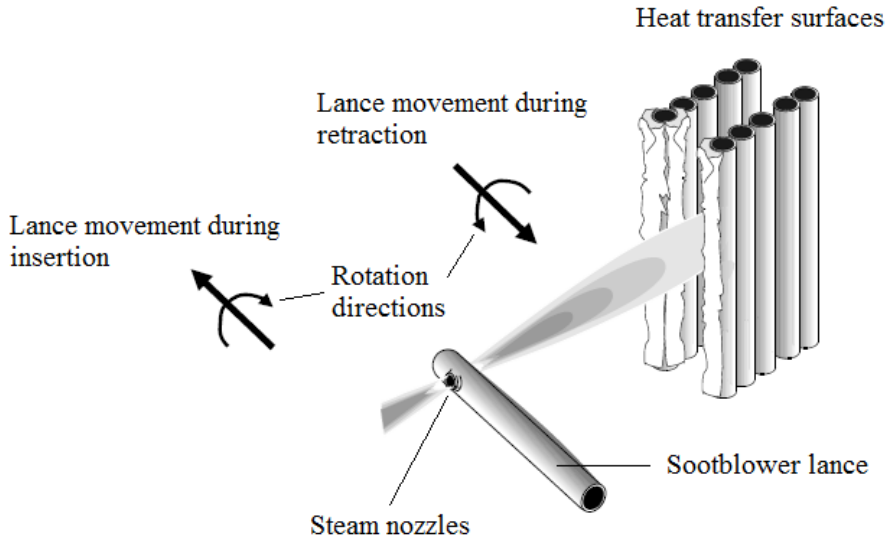

Figure 3.2: Cleaning process of a boiler bank by a sootblower.

Conventional sootblowers as described above have little or no knowledge of where the nozzles are positioned with respect to the heat transfer surfaces and the helical movement by the conventional sootblower cannot be easily adjusted, which makes the sootblower poor in intensity. A more advanced way to clean the heat surfaces is to use the so-called smart sootblowers.

The smart sootblower is equipped with two motors that independently control the traversing and rotating motion of the lance tube. This allows the nozzles of the sootblowers to be positioned in such way as to minimize the jet-tube interaction, hence dedicating all the jet power to remove deposits (Tandra & Shah, 2010). The cleaning strategy is shown in the figure below (Clyde- Bergman, Inc).

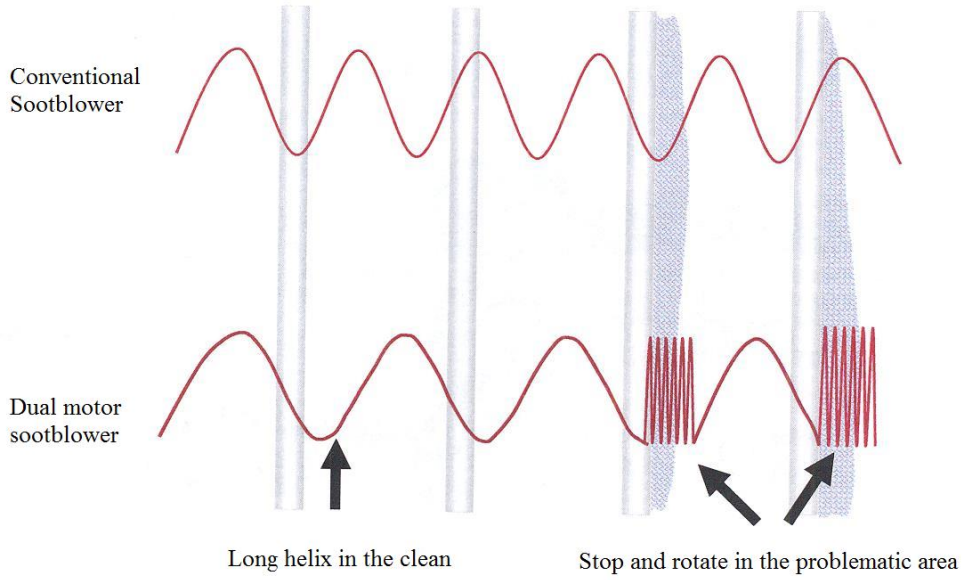

Figure 3.3: Dual motor sootblower's stop and rotate strategy.

In acoustic cleaning deposit build-ups on the heat exchange surfaces and other areas in the furnace are removed by means of sound pressure at frequencies varying in the audible region of 60-250 Hz. It is known by experience that the deposit removal would be more efficient if still lower frequencies were utilized. But lower frequencies have been observed to excite resonances of the structure. Therefore, frequencies below 60 Hz are avoided.

The sound pressure waves exert a vibrational excitation on the deposited particles. If they are loosened enough they are carried out of the boiler by the flue gases. Every deposit particle has its own mass and natural frequency. Maximal loosening of deposit is obtained if particles are excited at their natural frequency, i.e., at resonance. Away from the resonance the deposit particles remain on the heat exchange surface.

The efficiency of removal of the deposited particles depends on the mass, size, moisture content, cohesion strength, and density of the particles. These properties change as a function of temperature and time. The optimal size of the particle is considered to be less than 5.0 mm and moisture content percentage less than 8.5 %.

The highest usable temperature depends on the melting point of the particles. Acoustic deposit removal has been used at temperatures below 1000 ^{o}C. The sound pressure needed for acoustic deposit removal is produced by acoustic wave generators.

The wave generator is usually installed in a hole located on the boiler wall or roof so that the horn shaped part is left in level with the boiler's inner wall or partly inside it.

Acoustic soot remover consists of a horn and a wave generator. The structure of the acoustic soot remover is shown in detail in Figure 3.4. Compressed air at 6-7 bars is introduced into the wave generator usually from the plant's own compressed air distribution network. The wave generator's air inlet has a magnetic valve which, when opened, lets compressed air flow in continuously through the hole located at the bottom of the generator (1), thus causing the inner membrane (2) to bend. This allows the air to flow through the mating surface of the body and the membrane to the horn (3). The spring force caused by the bending of the membrane and the backpressure formed between the membrane and cover will press the membrane back on the mating surface (4). The continuous air flow forces the membrane to vibrate back and forth as described above. Membrane opening and closing frequencies are adjusted by regulating the length of the horn. (Nirafon, 2019)

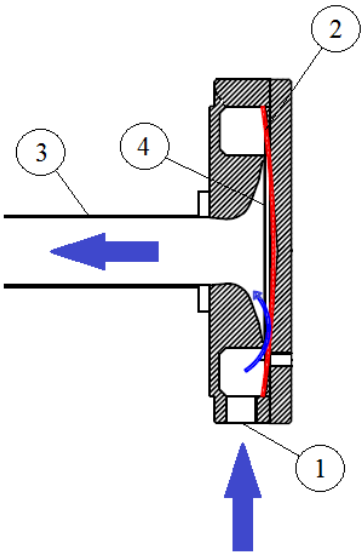

Figure 3.4: A wave generator.

Gas pulse cleaning is used to remove ash that has been accumulated on the heat transfer surfaces. It is based on the use of very strong shock pulses of short duration exerted on the flue gas flowing in the furnace of the boiler and on the heat transfer surfaces. These pulses make the gas to vibrate causing pressure waves to remove the deposits.

The pressure waves are typically created by a shock pulse generator (SPG) installed on the wall surface or ceiling of the boiler. The operation of the SPG is based on the explosion of a suitable mixture of oxygen (O_2) and natural gas (CH_4), and on the resulting rapid increase in pressure in a separate combustion cylinder. Figure 3.5 shows the key components of the SPG (Prostreram, 2019).

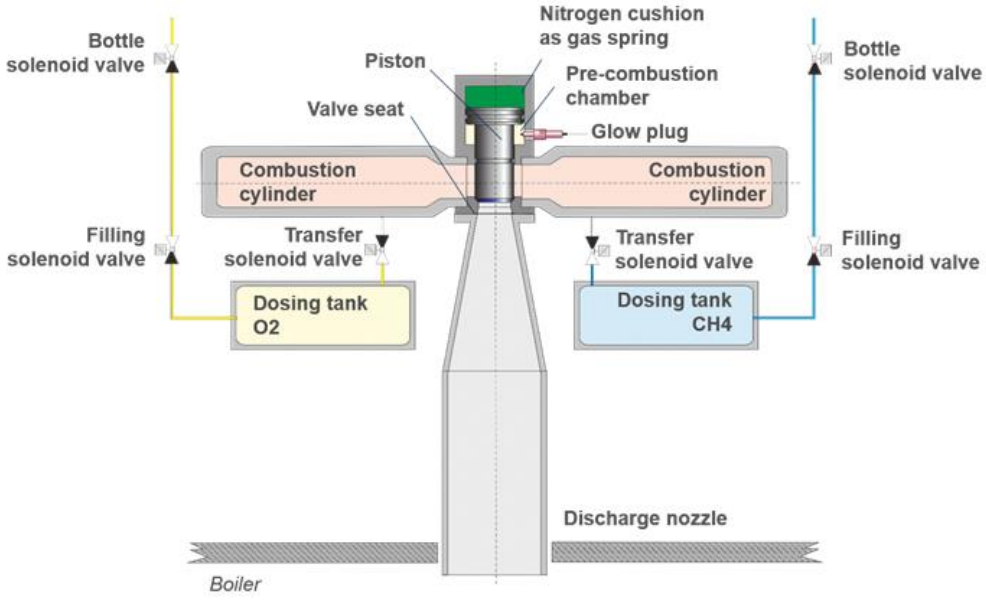

Figure 3.5: A schematic diagram of the shock pulse generator.

Oxygen and natural gas are conveyed into the dosing tanks through separate pipelines. The pipelines are equipped with valves that close when the dosing tanks are full. From the dosing tanks, oxygen and natural gas are led to a shared combustion cylinder, where they mix in the right proportion, forming an explosive gas mixture. The gas mixture is ignited in a pre-combustion chamber by means of a spark. When the gas explodes, it forces the piston to move upwards and at the same time the high-pressure combustion gas of approx. 250 bar discharges from the discharge nozzle (usually DN 125) into the furnace. The length of the discharging pressure wave varies, but the length of the effective pressure wave can be more than 10 m depending on the type of the device. Gas pulse cleaning can be used at temperatures above 1000 ^{o}C.

An old method to clean heat surfaces from deposit is to apply dynamic rapping impulses to the header tubes using manual force or air pressure cylinders. The heating surfaces are excited to vibrate. Inertial forces are applied on the deposit mass particles.

When these forces exceed the adhesion force then the particles are detached and fall down (Clyde Bergemann, 2019).

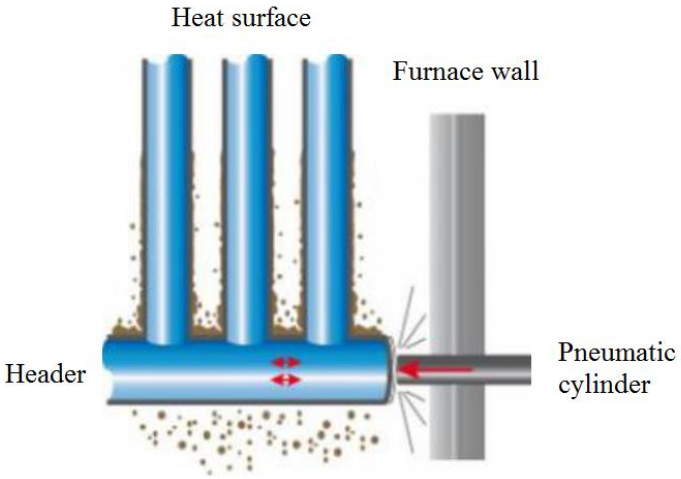

Figure 3.6: Rapping system.

3.2 The structures supporting the heat transfer surfaces

Supporting of the upper parts of the heat exchange surfaces is realized using the hanger rods. The role of the hanger rods is to transmit the mass force of the heat transfer surface with the deposit originated in the structure as well as that created in the combustion of the black liquor to the outside tertiary beams and further to the frame structure of the boiler. Supporting of the lower parts of the heat exchange surfaces is realized using the joining pipes located in the collection chamber to the structures outside the boiler. The joining piping must be designed so that it allows free vertical expansion of the heat surfaces. The supports are designed to allow a horizontal movement of the heating surfaces even under relatively small horizontal load. A horizontal load of varying magnitude is created during steam cleaning when the steam released from the rotating nozzle of the steam pipe hits the heat surface.

Horizontal supporters can be installed to decrease the horizontal movement caused by vibrations and to prevent fatigue damage at different points of the heat surface. A proper positioning and number of the supporters to minimize the vibrations is not always feasible. A typical construction of an economizer is shown in Figure 3.7 (Vakkilainen, 2005c).

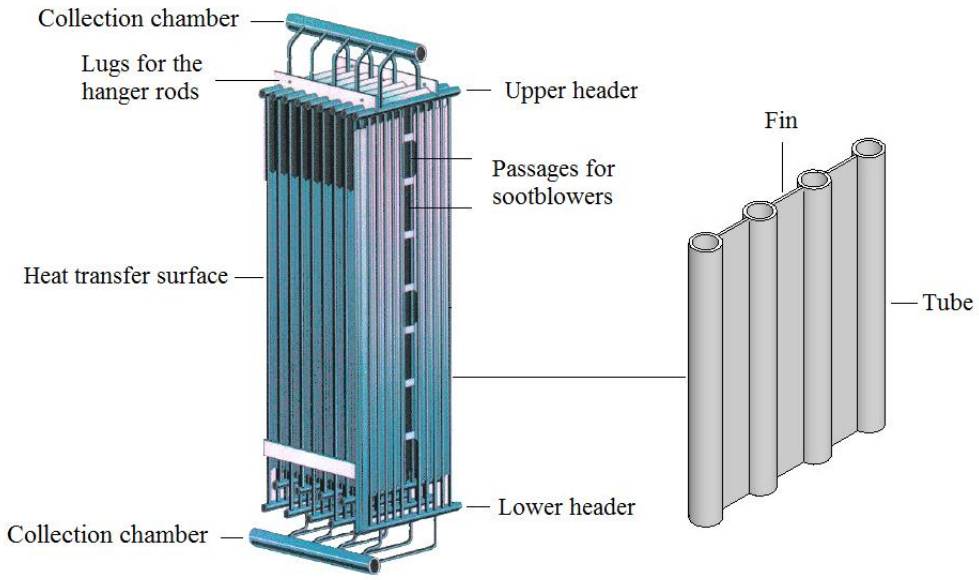

Figure 3.7: Vertical flow economizer.

3.3 Indications for the demand of soot removal

Figure 3.8 shows the basic parts of the support system of the heat surfaces. Loadings due to dead and operational weight of the boiler are transmitted via the tertiary beams (1) to the primary beams (2) which are connected at both ends to the boiler house. Hanger rods (3) are connected to the top of the heat surfaces (4) with pinned joints. The hanger rods are assembled symmetrically on both sides of the heat surfaces, and they go through drilled holes in the tertiary beams. The ends of the hanger rods (5) are equipped with nuts, which allow the rods to move vertically upwards, but not downwards.

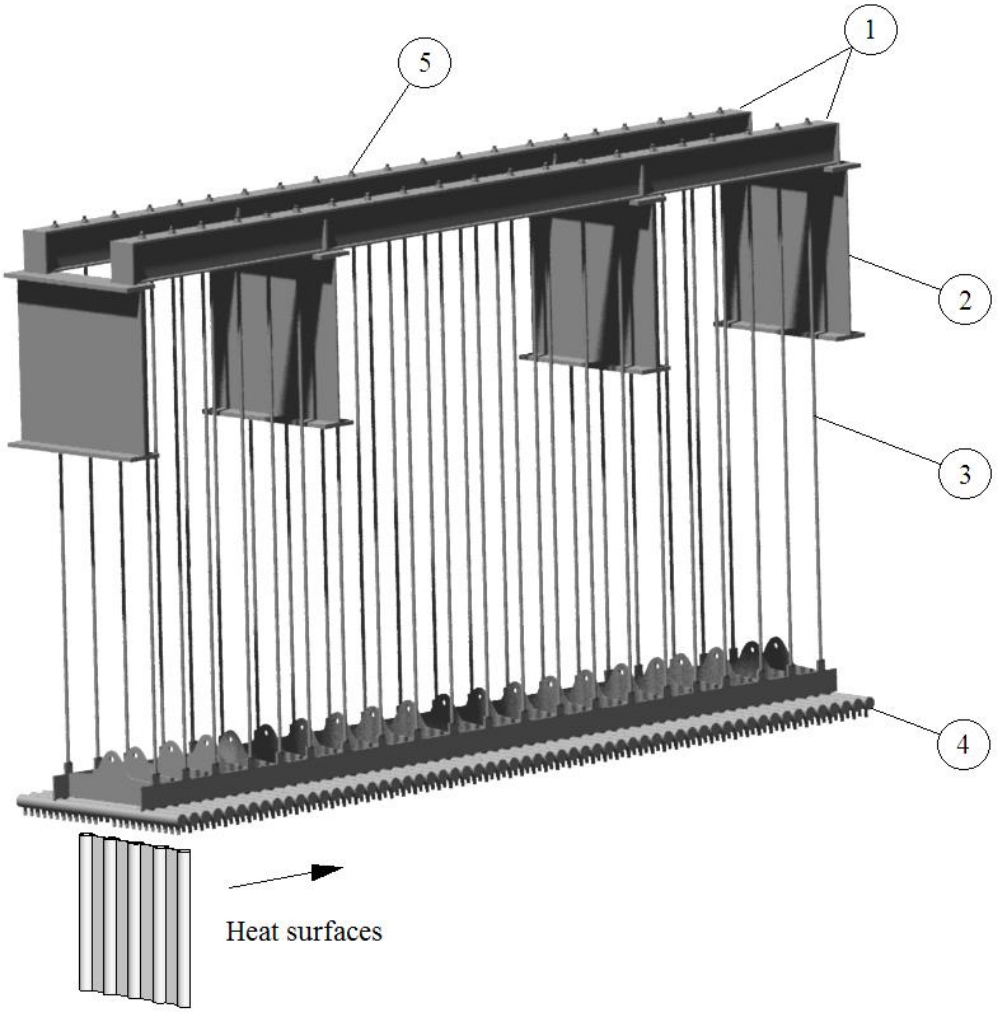

Figure 3.8: A typical supporting structure of the heat surfaces.

An accumulation of ash on the heat transfer surfaces causes tensile forces in the hanger rods. The dimensioning of the cross section area of the hanger rods is based on the dead load of the heat surface and the maximum allowable weight of the accumulated ash. The variable mass of the ash is typically much smaller than the platen mass. However, changes in ash mass can be measured directly from the hanger rods by strain gages, for example, provided that their sensitivity is high enough. This prospect gave motivation to develop a sensitive load cell to measure ash weight changes on the heat surface. This is discussed in more detail in Chapter 4.

The need for cleaning can be assessed by measuring the dust content of the flue gases by means of an ash analyser (RBDA, Recovery Boiler Dust Analyzer), specifically developed for this purpose. The main purpose of the analyser is to measure the amount of dust rather than the properties and composition of the dust. Various conclusions can be drawn about the operation of the recovery boiler on the basis of the amount of dust. This type of analyser is designed to provide information about the need for cleaning and its optimisation. The operation of the analyser is based on collecting flue gas particles from the flue gas duct of the recovery boiler, dissolving the particles in water, measuring the sodium content of the solution obtained and determining changes in the sulphate, SO_4 and chloride contents by using a separate measurement device PAD (Pulsed Amperometric Detector). The measurement results, the voltage response (mV) of sodium, the voltage response (mV) of the PAD cell and the temperature (°C) of the sample solution are saved on computer for further processing. As the concentration of the substances measured in the ash-water solution increases, the corresponding voltage response increases approximately linearly. If the cleaning intervals become longer, the amount of ash on the heat transfer surfaces increases, resulting in an increase in the amount of dust that is released during cleaning. (Sinkkonen, 2011)

Temperature measurement sensors are located in the furnace of the boiler. These are primarily used for monitoring the operation of the combustion process. But they are not typically used to predict the fouling of the surfaces. However, information obtained from the temperature measurement points near the heat transfer surfaces, such as superheaters, boiler bank and economiser, can be used to predict the fouling of the heat transfer surfaces. An increase of the operating temperature is probably caused by an increase of fouling of the heat transfer surface. The locations of maximal fouling are not easy to pinpoint by this method. One reason is that there are only a limited number of temperature measurement points in flue gas side.

The boiler furnace is designed so that the flow of the flue gases is forced to flow between the heat transfer surfaces. As the ash accumulates on the platens, it causes fouling. Then the transfer of heat from the flue gases to the heat transfer surface and to steam decreases. At the same time, the flow rate of the flue gases between the heat transfer surfaces increases. The concomitant pressure loss of the flue gases usually limits the maximum capacity of the recovery boiler. With high enough fouling the flue gas fan can no longer produce a sufficiently high pressure and flow. This causes losses in power production. Then, the load of the recovery boiler must be reduced. By placing the pressure measurement connections before and after the heat transfer surface, the pressure loss can be used to predict fouling and the need for cleaning. (Bajpai, 2017)

3.4 Fatigue failures

The heat transfer surfaces of recovery boilers – the boiler bank and the economiser – are manufactured by joining several planar structures together. The structure of an individual heat transfer surface is very simple. It consists of tubes and fins welded together as shown in Figure 3.7.

The branch tubes are connected to the header by drilling adjacent holes in the header in its longitudinal direction. According to the ASME design standard, there are restrictions on the diameter and thickness ratios of the header and the branch tube. When a shell or drum has a series of holes in a definite pattern, the net cross-sectional area between any two finished openings within the limits of the actual shell wall, excluding the portion of the compensation not fused to the shell wall, shall equal at least $0.7F$ of the cross-sectional area obtained by multiplying the center-to-center distance of the openings by the required thickness of a seamless shell, where the factor F is taken from Figure 3.10. In other words, referring to Figure 3.9, the cross-sectional area represented by the manufactured rectangle $5 \rightarrow 6 \rightarrow 7 \rightarrow 8$ shall be at least equal to the effective area of the rectangle $1 \rightarrow 2 \rightarrow 3 \rightarrow 4$ multiplied by 0.7 F, in which the value of F is obtained from Figure 3.10 and t_r is the required thickness of a seamless shell. (ASME, 2009)

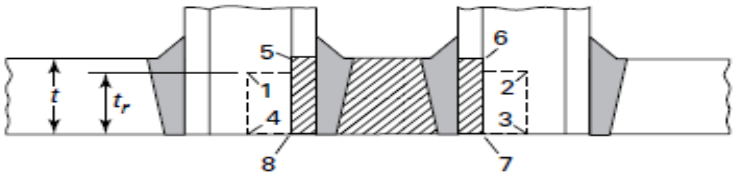

Figure 3.9: Effective and manufactured cross sectional areas between two openings.

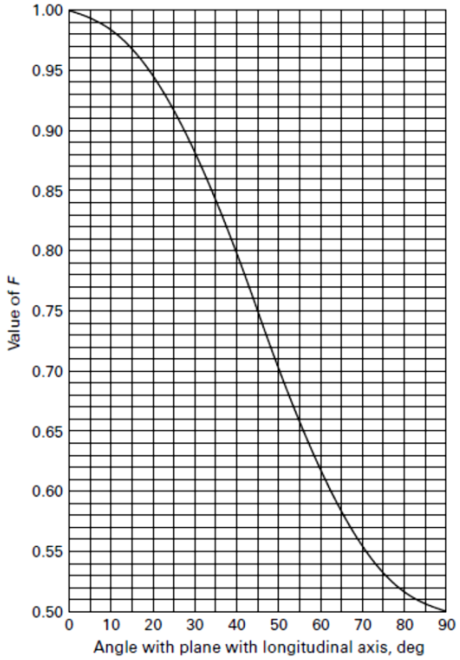

Figure 3.10: Chart for determining the value of the hole attenuation factor *F*.

In many cases, the above method of dimensioning a tube joint is sufficient. Often, however, the joint is subjected to a fluctuating loading, which can cause serious damages and economical losses. Figure 3.11 shows a fatigue failure of a weld at a branch connection of the feed chamber at the lower part of the boiler bank, resulting from vibrations.

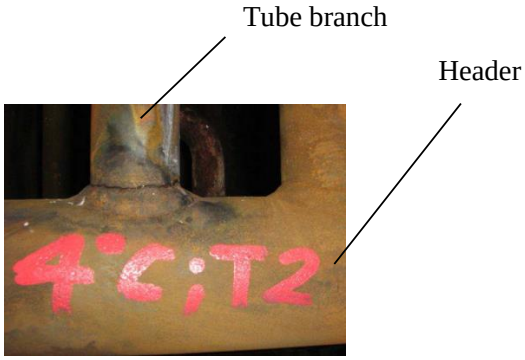

Figure 3.11: A fatigue failure at a branch connection of the header.

4 Measurement of ash mass from the hanger rods

The aim of this section is to describe the function, design, and testing of a measuring device. The function of the device is to measure nominal forces in the hanger rods due to ash mass changes on the platens during sootblowing. Verification of the system function was confirmed using FEM, the developed test equipment, as well as field measurements.

4.1 Approximation of the loads in the hanger rods

The distribution of the forces at the hanging rods can be estimated using different forms of ash mass on the platens. In most cases, it is enough to describe the distribution using a linear combination of three basic forms, an even form and two triangles as shown in Figure 4.1. A more accurate distribution could be obtained from a CFD analysis, for example. In addition, the data of ash density is needed. This varies in each boiler. Typically, the density of ash lies between $300 - 400$ kg $/\mathrm{m}^3$.

For the calculations the upper limit of the ash mass is considered to correspond the situation in which the heat surface is completely blocked. The beam supporting the rods is usually statically underdetermined due to multiple supports. Thus, the rod forces cannot be accurately solved analytically. But using the FE method the hanger rod forces can be calculated accurately enough.

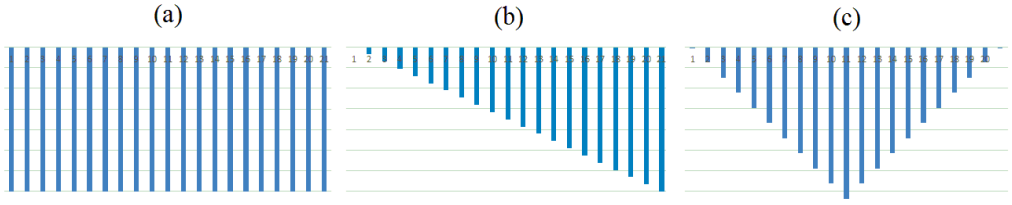

Figure 4.1: Forms for the ash mass distribution on the heat surfaces. Even (a) and triangular forms (b) and (c).

4.2 Preliminary construction of the measurement device

First tests were carried out by measuring support reactions of the tertiary beam. The goal was to obtain information on the 21 unknown hanger rod forces through four measured support reactions. Various algorithms were used to get estimates for the 21 forces. The results showed that the determination of hanger rod specific forces was not possible with required reliability, because the number of the unknown hanger rod forces

was 21 while the number of the measured support reactions was 4. This was an underdetermined system with too little information (Råde, L. & Westergren, B., 2001). It was concluded that each hanger rod force should be measured individually. To reach this goal, the first step was to develop a suitable measuring device for each hanger rod.

The operation of the device was based on the measurement of the axial elongation of a supporting bolt (5). The bolt had internal threads, for connecting it to the end of the hanger rod (2). The cylindrical shell (1) was mounted on the top of the support beam (3). The nut (4) was tightened so that the hanger rod was just lifted off the surface of the beam when the force, acting in the hanger rod, passed through the drive bolt to the upper end of the cylinder and further to the support beam. Strain gages were bonded on the opposite sides of the thin part of the bolt (5).

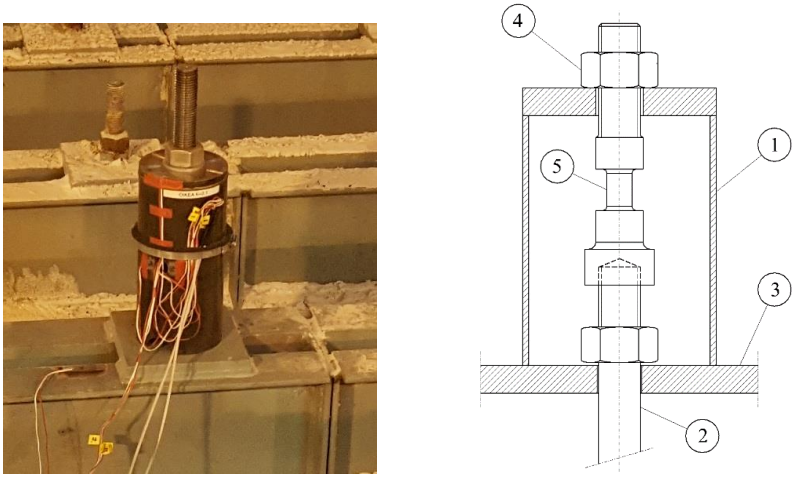

Figure 4.2: The first specimen of the measuring device for the hanger rods.

In Figure 4.3 ash mass values measured from one hanger rod are presented. Different stages can be distinguished from the graph: the ash accumulation and its peeling after sootblowing. The ash mass values are approximate, because the measuring devices were not calibrated. The purpose of the test was to show that a rod-specific measurement is feasible and the results obtained correspond to a reasonable degree of perception of the operation of the sootblowers.

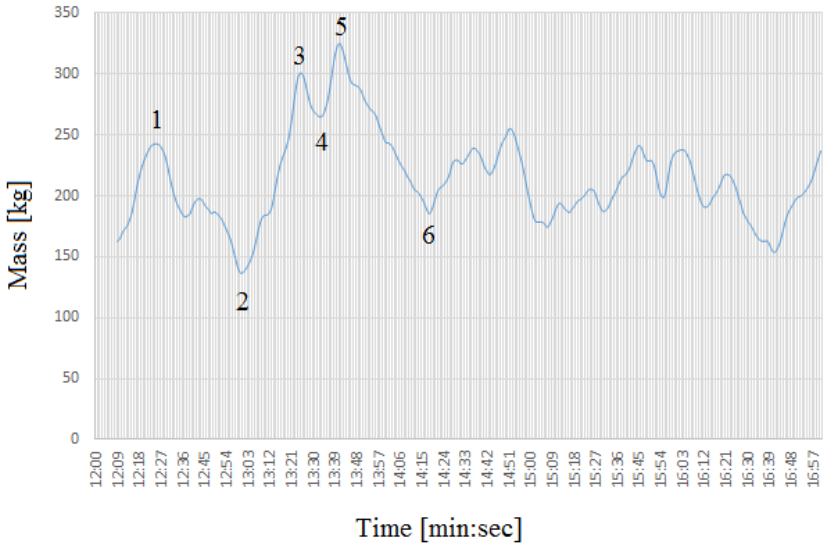

Figure 4.3: Results for the ash mass measured from one hanger rod of the superheater. The trends are: 1-2 sootblowing, 2-3 fouling, 3-4 dropping ash particles, 4-5 fouling, 5-6 sootblowing etc.

The weakness of this construction is its poor ability to measure small changes in the hanger rod forces. Because part 5 is assembled in series with the hanger rod, its diameter has to be almost the same as that of the hanger rod. This reduces the sensitivity of the measurement device. An alternative way is to mount the measuring device parallel to the hanger rod, so that it measures only the changes of the forces in the hanger rod instead of their absolute values.

4.3 New construction of the measurement device

The operation of the new construction of the measuring device is based on the displacement changes between two chosen points of the hanger rod. This information can be transformed to stress values in the device. It consists of a series-connected bar and a circular ring, mounted in parallel with the hanger rod. The displacements in the hanger rod will be transformed via the bar to the ring, which causes stress changes in the ring. The ring is very sensitive to its radial displacements (Timoshenko, et al., 2010). This is discussed later in this chapter. Figure 4.4 shows the essential parts of the new measurement device. The device is made of structural steel, grade S355.

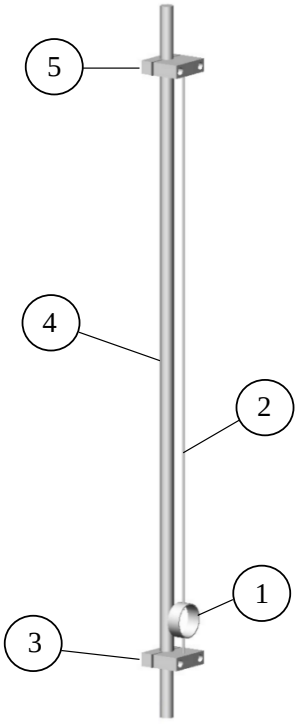

Figure 4.4: The new measurement device.

Table 4.1: Parameter values of the measurement device.

Item	Description	Diameter [mm]	Length [mm]	Width [mm]	Height [mm]
1	circular ring	65.0_{out}, 60.7_{in}		25.0	
2	tension bar	6.0	1000.0		
3	clamp		80.0	85.0	25.0
4	hanger rod	25.0	1700.0		
5	clamp		80.0	85.0	25.0

A hole is drilled through the clamp (5), where the bar (2) can move freely back and forth. At the end of the bar there is a nut, thus the end of the bar can move upwards but not downwards. The tension ring will be pre-tightened to the measured range of the ash weight. There are two criteria in dimensioning the tension ring. The first criterion is that the strain caused by elongation shall not cause yielding at the critical points of the ring. The second criterion is that the strain values need to be large enough to give a legible measuring result. However, the ring shape must remain circular enough in order to avoid the second order effects on strain-deformation behaviour of the ring.

4.4 Analytical design of the measurement device

In the analytical calculations it can be assumed that the tension ring and tension bar are replaced by springs, which are connected in series between the clamps. The spring constant for the springs in series is

$$k_{eq} = \left(\frac{1}{k_1} + \frac{1}{k_2}\right)^{-1} \tag{4.1}$$

The ring is subjected to two opposing forces *P* due to the displacements of the clamps as shown in Figure 4.5.

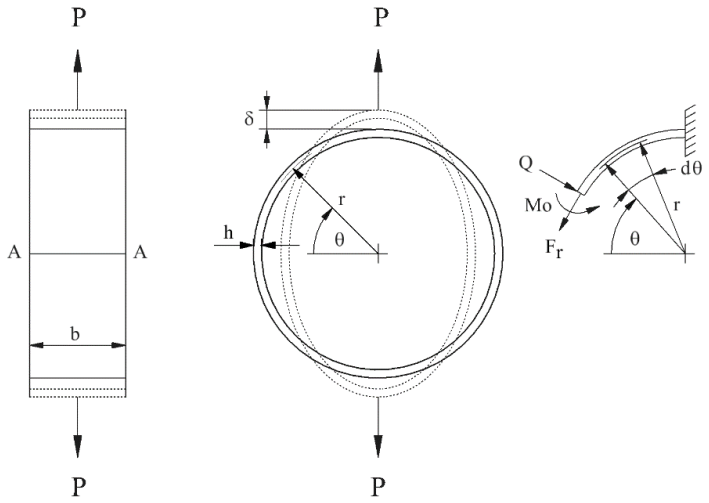

Figure 4.5: The tension ring with two opposing radial forces *P*.

In the ring, strains due to shear and normal forces are very small and can be ignored. (Timoshenko & Goodier, 2010). The total elongation of the half ring in the direction of force *P* can be written as

$$\delta = \frac{P}{2k_1} = \frac{Pr^3}{2EI}\left(\frac{\pi}{4} - \frac{2}{\pi}\right) \tag{4.2}$$

Therefore, the spring constant for the ring is

$$k_1 = \left[\frac{r^3}{EI_1}\left(\frac{\pi}{4} - \frac{2}{\pi}\right)\right]^{-1} \tag{4.3}$$

where I_1 is the area moment of inertia of the ring cross-section about its principal axis

$$I_1 = \int_{-\frac{h}{2}}^{\frac{h}{2}} \frac{y^2}{1+\frac{y}{r}} b dy \tag{4.4}$$

The spring constant for the tension bar is

$$k_2 = \frac{EA_{bar}}{L_{bar}} \tag{4.5}$$

where A_{bar} is the cross-sectional area and L_{bar} the length of the bar. At the section A-A shown in Figure 4.8, corresponding to $\theta = 0$ in Figure 4.5, the bending moment M has its maximum value

$$M = \frac{1}{2} \cdot k_{eq} \cdot \Delta_{hr} \cdot r \cdot \left[1 - \frac{2}{\pi\left(1+\frac{I_1}{Ar^2}\right)}\right] \tag{4.6}$$

where Δ_{hr} is the displacement between the clamps in the hanger rod and r the mid radius of the ring. Stress values at the inner and outer surfaces of the ring can be calculated (Ylinen, 1975) as

$$\sigma_{inn} = \frac{N}{A} + \frac{M}{rA} - \frac{M}{I_1} \cdot \frac{a_{inn}}{1-\frac{a_{inn}}{r}} \tag{4.7}$$

$$\sigma_{out} = \frac{N}{A} + \frac{M}{rA} + \frac{M}{I_1} \cdot \frac{a_{out}}{1+\frac{a_{out}}{r}} \tag{4.8}$$

where $N = \frac{P}{2}$

The ring should be designed so that it functions reliably without plastic yielding at possible overloads. The safety margin should be over 2, that is

$$Z = \frac{\sigma_{yield} - \sigma_b}{\sigma_b} + 1 > 2 \tag{4.9}$$

This is based on the assumption of falling ash particles. Namely, in some cases the sootblowing can remove a large amount of ash from the heat surface which can hit the adjacent surfaces.

4.5 Numerical analysis

The geometry of the structure was modelled according to the dimensions shown in Table 4.1. The length of the hanger rod in the model was 1700 mm, which corresponds to the length used in the tests. Modelling of parts 2-5 was done using a linear 8-node brick element (linear hexahedral). The average element size was about 5.0 mm. The ring was modelled using 4-node shell elements (Hughes, 2000). The average element size was about 2.0 mm. In the model the modulus of elasticity was 206000 MPa and the effect of gravity was ignored. In Figure 4.6 the FE-model of the test apparatus is presented.

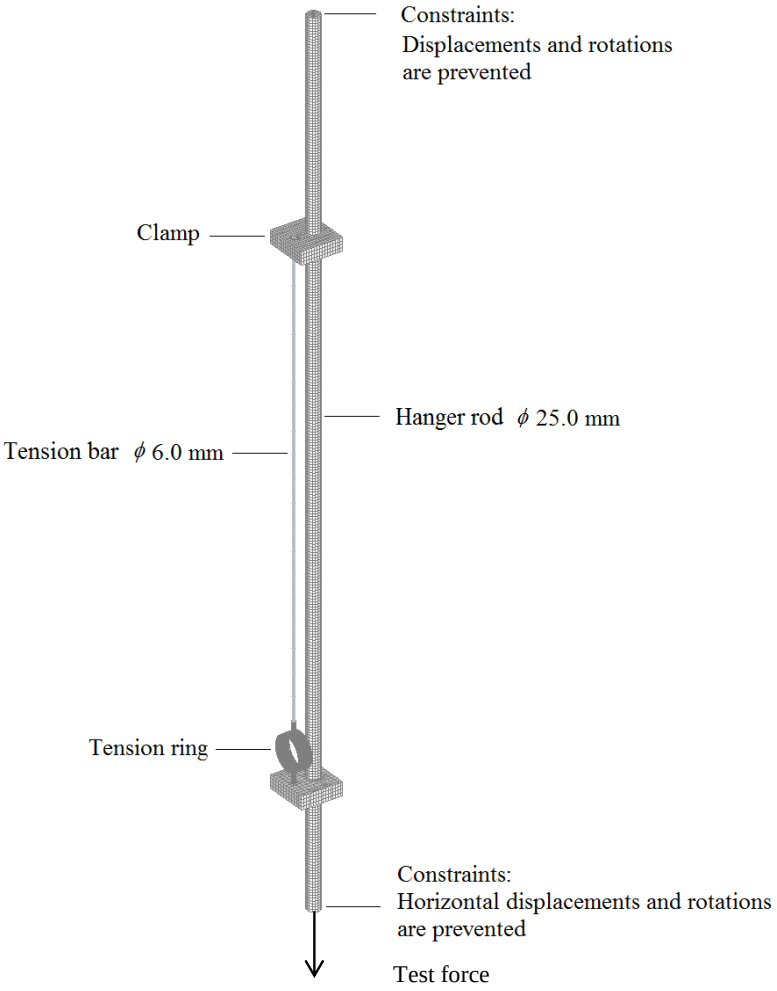

Figure 4.6: FE-model of the measurement device for linear elastic analysis.

4.6 Verification of the measurement system

In addition to the theoretical calculations and FEA, stress and strain values of the tension ring and hanger rod were measured using a test equipment. The magnitude of the acting force in the hanger rod was adjusted by multiplying the internal pressure of the hydraulic cylinder by the effective surface area of the cylinder. Due to the possibility of buckling of the frame, the maximum force in the test was limited to the value of 65 kN in the hanger rod. During the measurements it was observed that for rod forces below 5 kN the noise in the measurement signal increased making the signal indecipherable enough to be discarded.

On the hanger rod two strain gages were bonded on the opposite sides 410 mm above the lower clamp as shown in Figure 4.7. The purpose was to evaluate the significance of the bending stresses, generated in the hanger rod, to the stress results obtained from the tension ring.

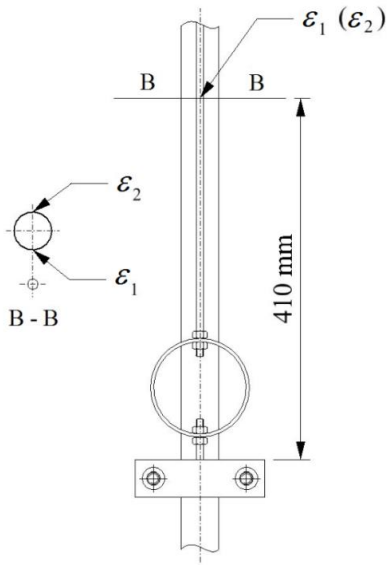

Figure 4.7: Locations of the strain gages on the hanger rod for measuring the strains ε_1 and ε_2.

The axial and bending stresses on the surface of the hanger rod are, respectively,

$$\sigma_a = E \cdot \varepsilon_a = \frac{\varepsilon_1 + \varepsilon_2}{2} E$$
$$\sigma_b = E \cdot \varepsilon_b = \pm \frac{\varepsilon_1 - \varepsilon_2}{2} E \quad (4.10)$$

The best sensitivity to bending stress in the tension ring is achieved using a full Wheatstone bridge, which also provides temperature compensation of strain gages as well as tensile strain compensation (Window, 1992).

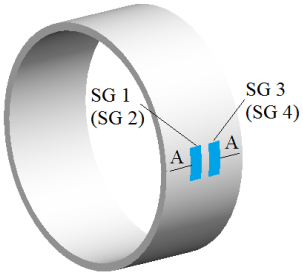

Figure 4.8: Locations of the strain gages on the tension ring. Strain gages SG1 and SG3 are bonded on the outer surface and strain gages SG2 and SG4 on the inner surface of the ring.

Table 4.2: Specification of the strain gages (Kyowa).

Parameter	Value
Type	SKF-23900
Resistance	350 Ω
Gage length	5.0 mm
Gage factor	2.1±1.0%
Gage cement	CC-33A, EP-34B

The data for the strain gages used are given in Table 4.2. More detailed calculations of the tensile strains of the tension ring are presented in Appendix C.

4.7 Results

The verification of the measurement system was carried out by 13 different randomly chosen axial forces in the ϕ 25.0 mm hanger rod. The results of the measured strains and those of FE calculations for the tension ring are summarized in Figure 4.9.

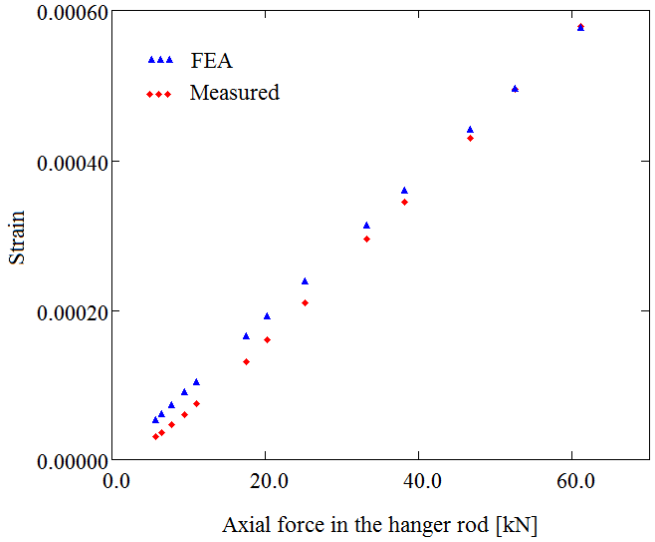

Figure 4.9: Strains at the critical point in the middle of the line A-A of the tension ring.

The results of the theoretical and FE calculations for the tension ring are summarized in Figures 4.10 and 4.11.

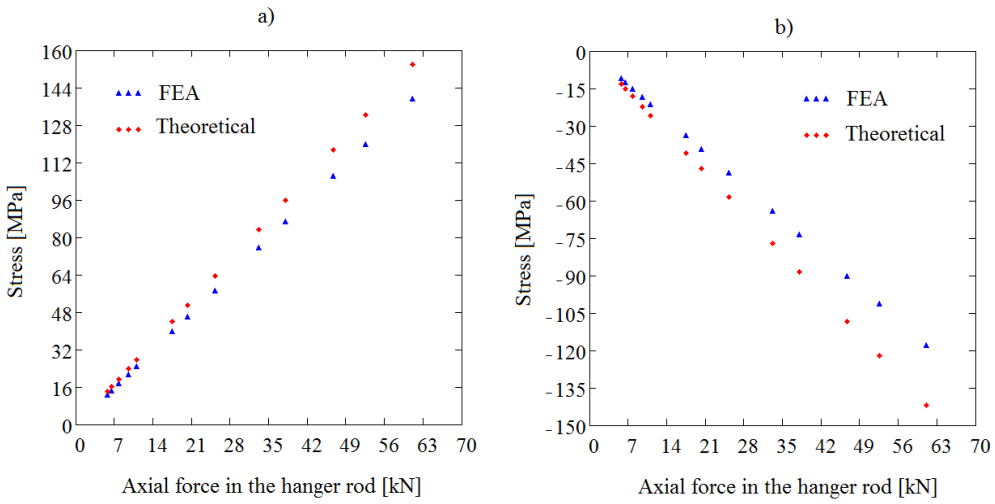

Figure 4.10: Stress in the hoop direction (a) on the inner surface, and (b) on the outer surface in the middle of the line A-A.

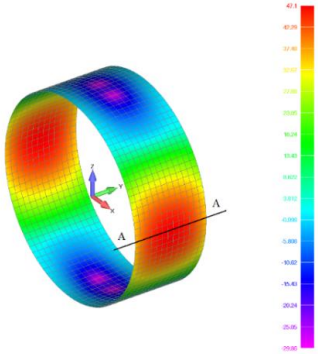

Figure 4.11: The maximum principal stress in the middle of the line A-A on the outer surface of the ring is 46.3 MPa due to a 20.3 kN vertical force in the hanger rod, which is about 33% of the maximum hanger rod force 61.1 kN. The stress distribution is calculated using FEM.

In Figures 4.12 (a) and (b) the measured stress values from the hanger rod on opposite sides of the rod and the corresponding stress values from the FEA and theoretical calculations are presented.

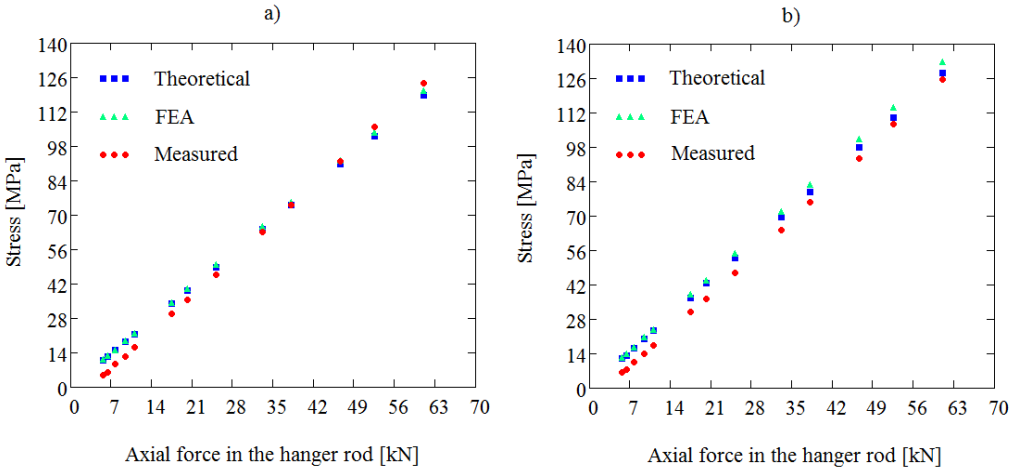

Figure 4.12 : (a) Flexural stress σ_1, and (b) σ_2 in the hanger rod.

Figures 4.13 (a) and (b) show the strain values in the tension ring, calculated by using FEM. The parameters used in the computations are the ring thickness, which ranges from 0.5 mm to 8.0 mm, the distance between the clamps, 1000 mm or 2000 mm, and the diameter of the bar 6.0 or 12.0 millimetres. The width and the outside diameter of the ring, and the axial force in the hanger rod are kept as constants in the computations.

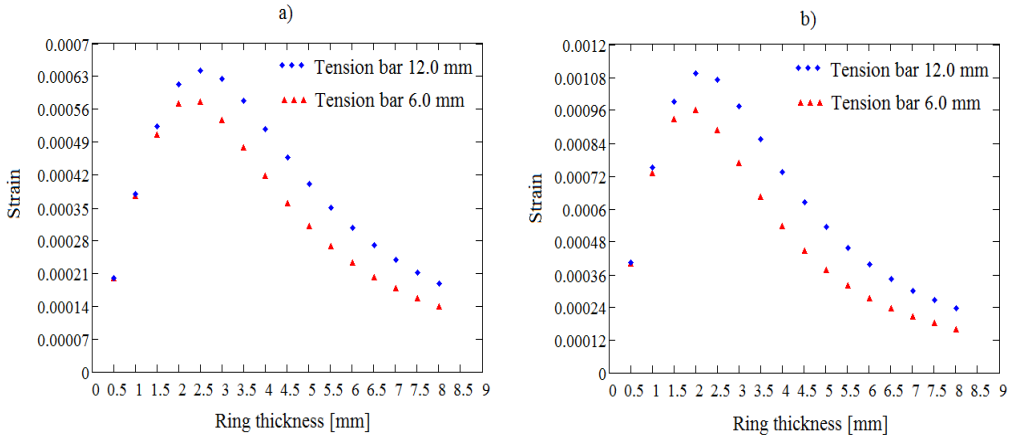

Figure 4.13: Strains due to bending in the middle of line A-A on the outer surface of the tension ring for tension bar diameters 6.0 mm and 12.0 mm. The distance between the clamps is (a) 1000 mm and (b) 2000 mm.

From Figures 4.13 (a) and (b) it can be seen, that increasing the distance between the clamps increases the strains in the ring. The same effect is obtained by increasing the diameter of the tension bar. According to Figures 4.13 (a) and (b), the best sensitivity for the ring and the accompanied Wheatstone bridge is obtained, when the thickness of the ring is 2.5 mm and 2.0 mm, respectively. Figure 4.14 shows a slightly bent hanger rod due to bending moments at the clamps. This is caused by the eccentric force in the tension bar. According to Figs. 4.12(a) and 4.12(b), the effect of the bending moment on the rod is small and can be neglected, especially at large axial forces. This is discussed in more detail in Chapter 6.

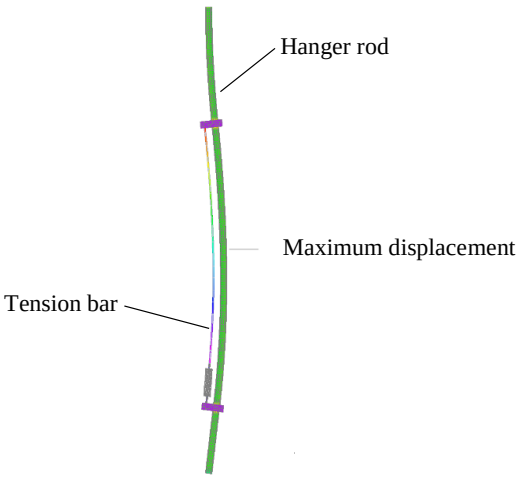

Figure 4.14: Deformed shape of the hanger rod. The maximum horizontal displacement in the plane of the figure is 0.6 mm, when the hanger rod is subjected to an axial force 61.1 kN.

4.8 Preliminary measurements at the site

Two hanger rod assemblies were measured. The goal was to study the reliability of the operation of the measurement device in an actual factory site. Measurement results in terms of weight versus time are shown in Figure 4.15 for the two hanger rods. When fouling increases rapidly the sootblower is activated by its sequence control. These curves show that fouling decreases when the sootblower is actively working to remove fouling. The following conclusion can be drawn. Cost effective soot removal can be achieved utilizing accurate real time information of soot masses supported by the hanger rods. This motivates implementing a measuring device to each rod. Then the sootblowing sequence can be activated to remove first the soot pluggage peaks before they grow too massive, and when they still can be removed safely with low forces. Later in 2018 a new measurement system was installed in which each rod was provided with a measurement device of its own.

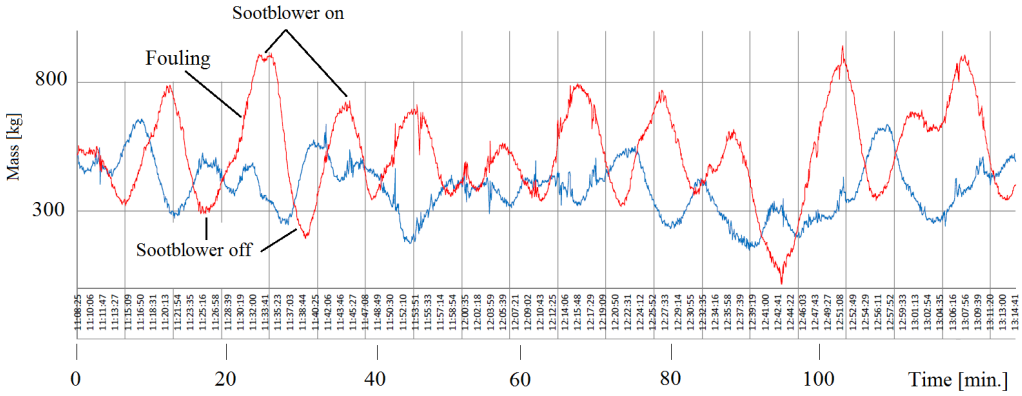

Figure 4.15: Ash mass as a function of time for two hanger rods. The measurement was done during the time range 11:08 – 13:14 . The length of the measurement was 126 minutes. It can be seen that the ash mass decreases rapidly when the sootblower is working.

The measuring device is ready for use immediately after the installation, and the force changes in the hanger rod can be monitored. However, the magnitude of the load can be matched to the actual load only after calibration. This requires water washing of the boiler's heat surfaces. After the water wash, it can be seen from the measurement results that the forces in the hanger rods are reduced for a while before they start to grow again. This is because, when the boiler is standing, the heat surfaces are filled with water and, when heated, the water turns into steam and evaporates away. Especially in the older boilers, the tightness of the hanger rods can vary remarkably. This causes variation in the measurement results. Therefore, the hanger rods must be tightened to the same tightness before installing the measuring device. The measured hanger rod forces give an estimate of the horizontal ash distribution on the heat surface, but so far no vertical distribution. In order to determine the vertical distribution, a project is currently underway to investigate whether the fast Fourier transform (FFT) of measured

vibration data provides sufficient information on the vertical mass distribution of the thermal surface. The frequencies calculated from FFT can be compared to the frequencies caused by different ash distributions in the height direction evaluated by the aid of the numerical models developed in this work.

5 Numerical analysis

The aim of this section is to compare the eigenfrequencies of the heat surfaces obtained by the FEM and by the use of experimental measurements.

The heating surfaces consist of several parallel tubular platens and are supported at upper parts by rods joined to the upper support frame of the recovery boiler as presented in Figure 3.7. The lower parts are joined to the collecting chamber supported by the tubes connected to it. In Table 5.1 the essential dimensions of the platen are shown.

Table 5.1: Main dimensions of the heat surface platen.

Height [mm]	Width [mm]	Pitch of tubes [mm]	Tube outer diameter [mm]	Tube thickness [mm]	Fin [mm]
22715	2836	114.0	51.0	5.6	5.0

The geometry of the heat transfer platen was meshed using linear quadrilateral shell elements only. This first order element has four nodes at each corner and it can resist membrane, shear and bending forces. Proper applications are any structures which are comprised of thin plates or shells (Cook et al., 2002).

The values $2.06 \cdot 10^{11}$ Pa for Young's modulus and $8000\ \mathrm{kg/m^3}$ for the density of steel were used. In the model, a rigid connection on the top of the recovery boiler was assumed. Similarly, the connection of the collection chamber and the tubes was assumed to be rigid. Due to the nature of the eigenmode analysis loadings can be ignored (Weaver & Johnston., 1987). The number of elements in the model was approximately 1.2 millions and the average element size 5-50 mm.

Correspondingly, a more simplified FE-model of the platen was created using beam elements. The linear beam element has one node at both ends and it is determined by material values, the cross-sectional area, the orientation vector, the moments of inertia and torsional stiffness. Both nodes have six degrees of freedom, three displacements and three rotations. In this model, the number of elements was approximately 40 which ensured mode shapes and eigenfrequencies accurate enough.

Figures 5.1 - 5.3 show the eigenmodes and corresponding eigenfrequencies calculated using these two FE-models. In Table 5.2 a summary of the FEA and the experimental modal analysis is presented. In Appendix D the corresponding analytical hand calculations for the frequencies are presented.

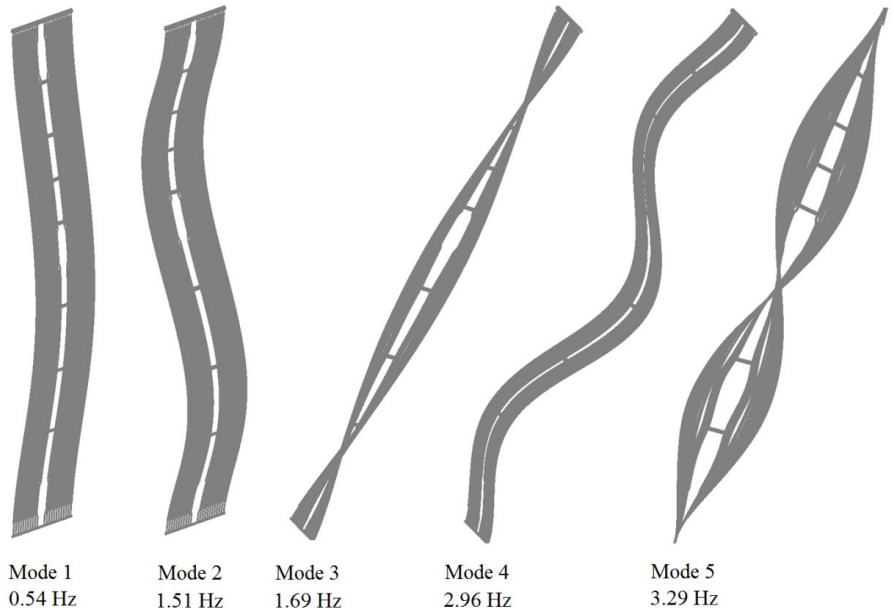

Figure 5.1: Mode shapes and eigenfrequencies of the platen by using shell elements. All translations and rotations are fixed at the boundaries.

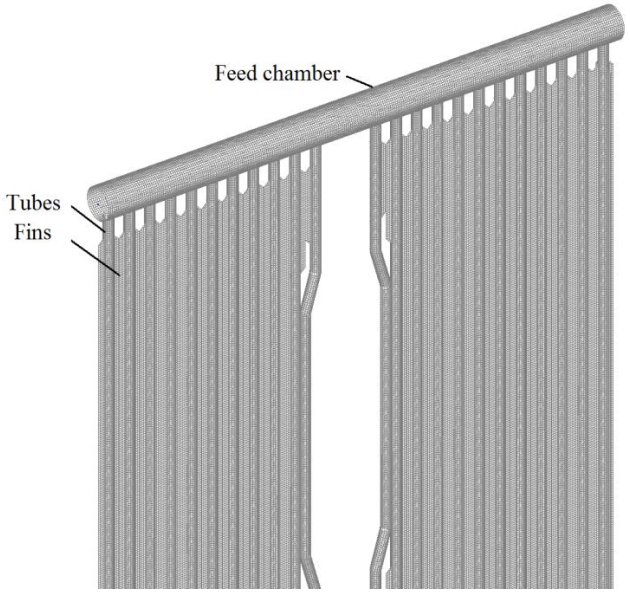

Figure 5.2: A detail of the shell element model of the top of the platen.

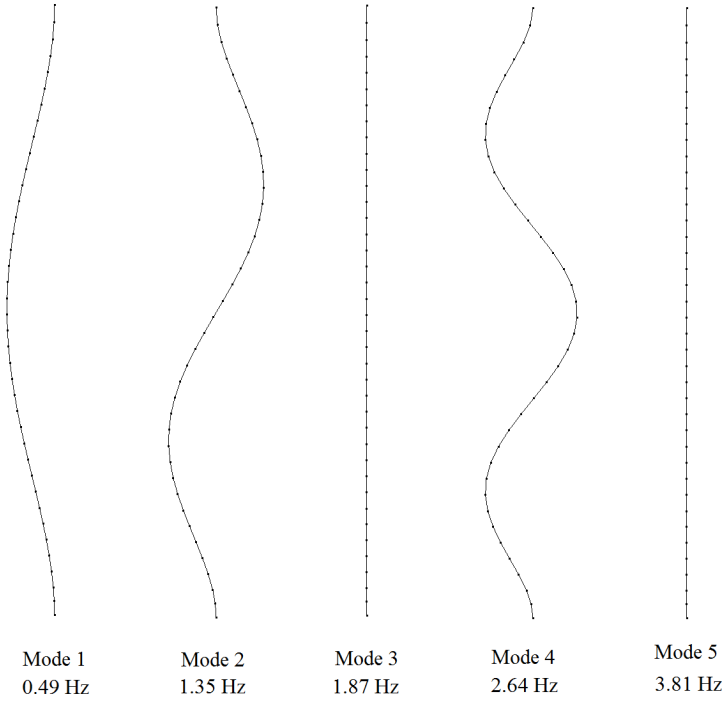

Figure 5.3: Mode shapes and eigenfrequencies of the platen by using beam elements. All translations and rotations are fixed at the boundaries.

Table 5.2: Comparison of the eigenfrequencies (Hz) of the heat transfer platen.

Mode	Experimental modal analysis	Shell model	Beam model	Mode shape
1	0.63	0.54	0.49	bending
2	1.46	1.51	1.35	bending
3	1.90	1.69	1.87	torsion
4	2.68	2.96	2.64	bending
5	3.32	3.29	3.81	torsion

5.1 A predictive FE-model for the fatigue calculations

In many cases, fatigue damages occur in the joints of the tube branches as presented in Section 3.3. The fatigue analysis can be done by meshing the structure with shell elements and solving the problem with an appropriate FE-solver (Martikka, et.al., 2005). This type of element model is often very large and takes a lot of computing time depending on the chosen analysis type. The calculation of the alternating loadings at the joints can be done by using simple beam elements as described in the previous section.

Its advantages include easy modelling and short computing time compared to a complete model of shell elements. Such a beam model gives a good approximation of the loadings at the joints of the tube branches for further fatigue calculations.

When using time history based calculation methods the loads are given as a function of time and the model is solved at each time step. In this study the soot blowing excitations are modelled as impulse forces with a short duration. In all loading cases, the magnitude of the impulse force is chosen as 0.25 kN with a 2.0 s duration.

The soot blowing sequences are defined in terms of the start times to each lance at locations determined by the altitude from a reference level. The used soot blowing sequences are given in Table 5.3. Various sequences can be devised as desired. Here the sequences are chosen randomly for the study.

Table 5.3: Data for the sequences used in the time history analysis.

Sootblower	Altitude [mm]	Sequence 1 [s]	Sequence 2 [s]	Sequence 3 [s]
1	20775	0	60	60
2	17175	40	20	50
3	13575	10	40	40
4	9975	50	0	30
5	6975	20	30	20
6	3975	60	50	10
7	1010	30	10	0

Figure 5.4 shows the loading due to Sequence 1 of Table 5.3. The sootblowers move in the furnace back and forth causing loadings on both sides of the platen as described in Section 3.1.

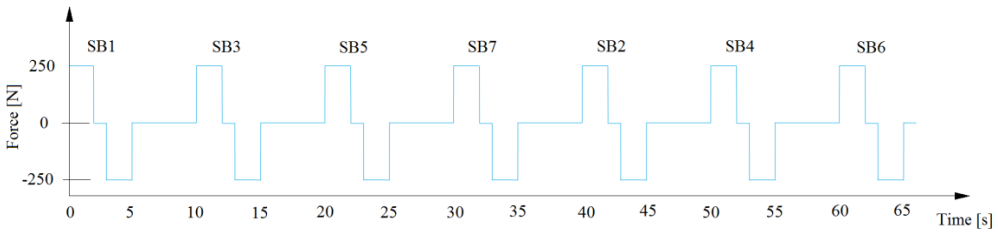

Figure 5.4: Loading on the platen due to steam jets of the sootblowing Sequence 1. After 65 s the loading is zero.

A simplified model of the platen and forces due to sootblowing are shown in Figure 5.5. When the steam jet is between two platens, the steam pressure causes perpendicular forces on the surface of the platens. When the sootblower has bypassed the platen, the direction of the force will be reversed.

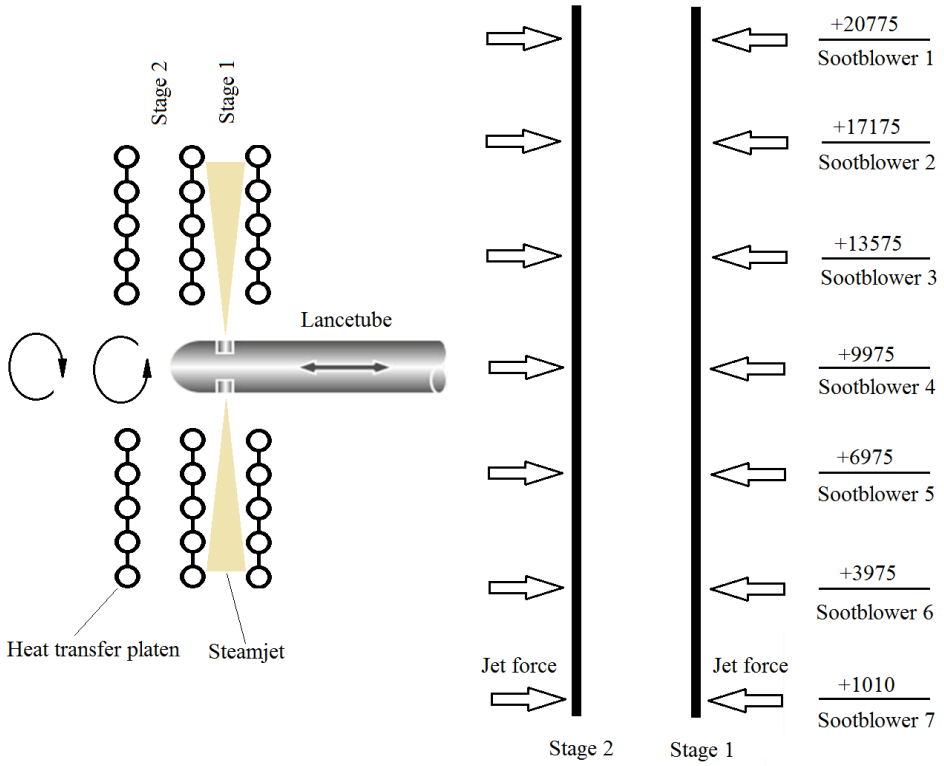

Figure 5.5: Vertical locations of the sootblowers and loadings on the platen due to sootblowing.

The results of the FE-simulation generate ranges of bending moment ΔM_i at the joints of the tube branches at duration of each block loading n_i. This data is processed using Equation 5.1 to obtain an equivalent constant amplitude moment variation range (Kocak, et al., 2008)

$$\Delta M_{eq} = \left(\frac{\sum_{i=1}^{k} \Delta M_i^m n_i}{\sum n_i} \right)^{\frac{1}{m}} \tag{5.1}$$

The calculated results for each sequence are shown in Figures 5.6-5.8 and the corresponding data in Appendix B.

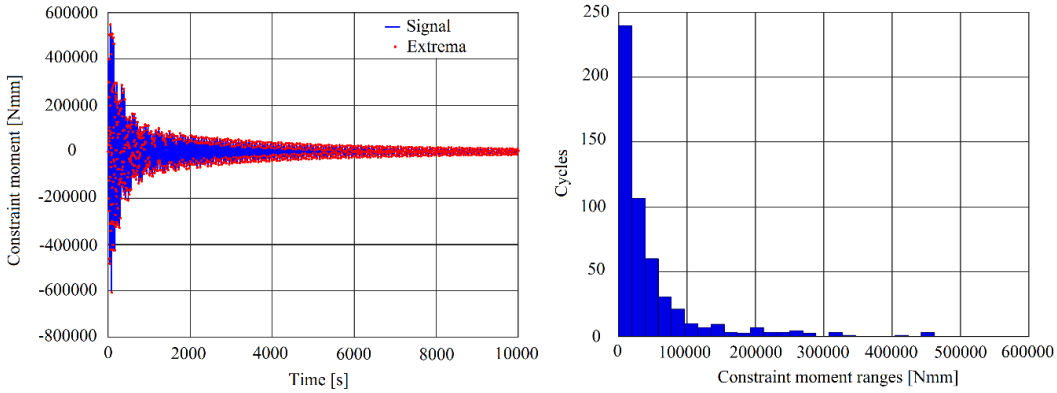

Figure 5.6: Time history of the bending moment for Sequence 1 and the Rainflow histogram of number of cycles versus bending moment. An equivalent constant amplitude bending moment is $\Delta M_{eq} = 133$ Nm.

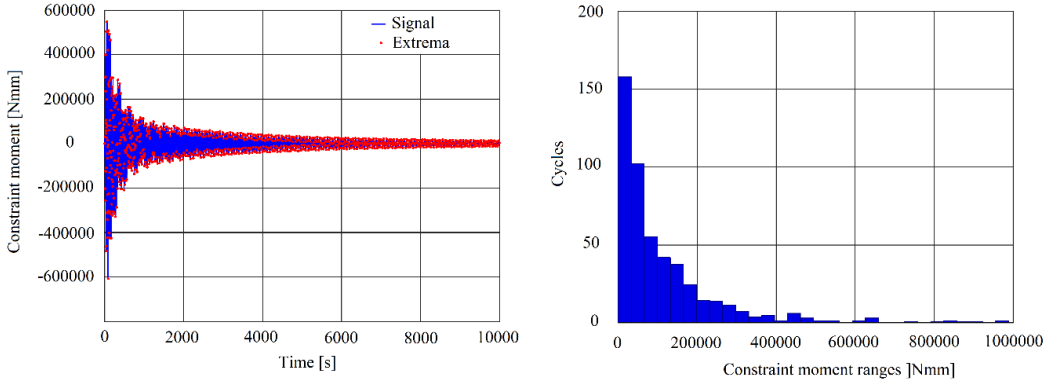

Figure 5.7: Time history of the bending moment for Sequence 2 and the Rainflow histogram of number of cycles versus bending moment. An equivalent constant amplitude bending moment is $\Delta M_{eq} = 247$ Nm.

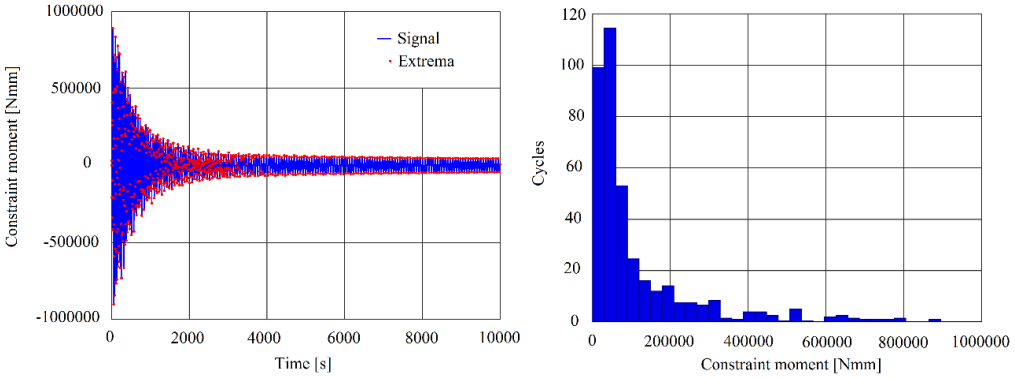

Figure 5.8: Time history of the bending moment for Sequence 3 and the Rainflow histogram of number of cycles versus bending moment. An equivalent constant amplitude bending moment is $\Delta M_{eq} = 259$ Nm.

Note that the value of ΔM_{eq} is much smaller for Sequence 1 than for Sequences 2 and 3. Therefore, in terms of fatigue, Sequence 1 is less detrimental than the other two. The reason for this is that, when using Sequence 1, the consecutive sootblowers cancel the platen vibrations generated by each other more effectively. Such phenomenon has not recognized in prior studies, and provides thus an opportunity to seek for an optimal sootblower sequence (Martikka & Pöllänen, 2015).

5.2 Fatigue strength of the branch connection

In the design of tubular joints a common engineering practise has been to consider the pressure loads only. The dynamic loads such as torsion and shear of the platens have been ignored. The FEM is used to study the influence of branch tubes of different size on the fatigue life. Two approaches have been used: the effective notch stress (ENS) approach and linear elastic fracture mechanics (LEFM). A fully reverse constant amplitude out-of-plane bending moment acts at the end of the branch tube, i.e., the stress ratio R is -1. This assumption is based on an experimental modal analysis of the platen.

The operating internal pressure in the tube is assumed to be constant. Thus, it does not cause a fluctuating loading and can be ignored in the fatigue analyses. In the calculation model, translations and rotations are prevented at the right end of the header. This causes local stresses, which decay rapidly to zero at 20 mm from the restraint. At the symmetry plane (surface 2, see Figure 5.9), only translation in the z-direction is prevented as symmetry requires. The FE model is established by parabolic brick elements. The platens are operated in the temperature range +310 ºC - +335 ºC (Pöllänen, 2009). The decrease of the Young's modulus is taken into account in the models, using 172000 MPa in further calculations.

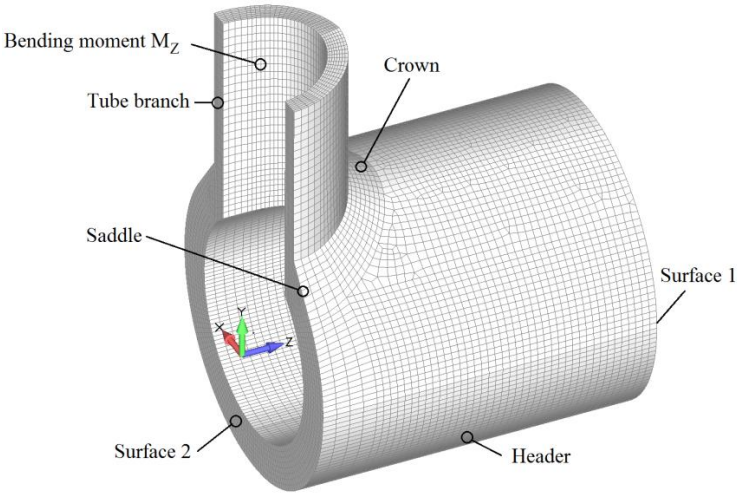

Figure 5.9: Names of the essential parts of the branch connection.

Due to the platen vibrations, the tube joint is subjected to a bending moment M_z that causes bending (σ_b), membrane (σ_m), and nonlinear (σ_{nl}) stress distributions at the weld toe as shown in Figure 5.10.

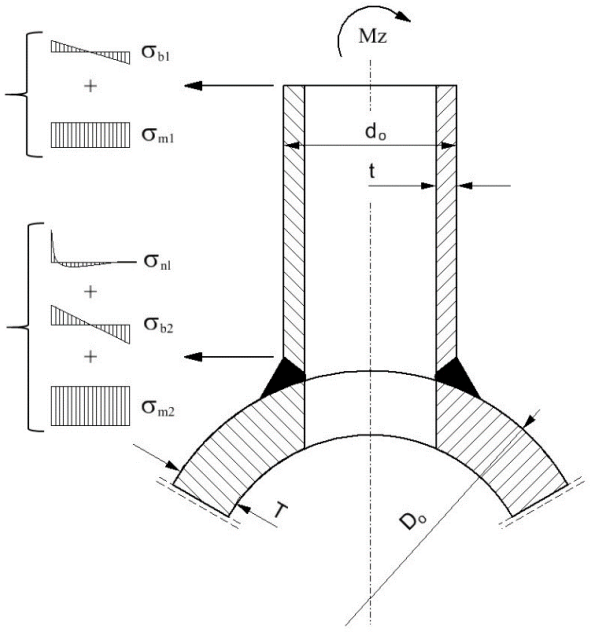

Figure 5.10: Membrane, shell bending, and non-linear peak stresses in the branch tube.

The values for the parameters T, D_0, t and d_0 used in the analyses are presented in Table 5.4.

Table 5.4: Values for the parameters T, D_0, t and d_0 used in the calculations.

Header outer diameter D_o [mm]	Header wall thickness T [mm]	Branch outer diameter d_o [mm]	Branch wall thickness t [mm]
88.9	12.5	33.7	5.0
88.9	12.5	51.0	5.0
88.9	12.5	70.0	5.0
88.9	12.5	33.7	6.3
88.9	12.5	51.0	6.3
88.9	12.5	70.0	6.3
88.9	12.5	33.7	7.1
88.9	12.5	51.0	7.1
88.9	12.5	70.0	8.0

5.2.1 **Effective notch stress approach, ENS**

The ENS approach is applicable to welded joints, which are expected to fail at the weld root or weld toe. The inspection documents (Chile, 2008) reported findings of the cracks on the outer surfaces only. The results of the FE analyses of this thesis confirm this observation. Thus, this study focuses only on the weld toe on the outer surface of the branch connection. The effective notch stress at the weld toe is obtained by using linearly elastic FE analysis. The effect of the higher temperature on the FAT class has been considered by using a stress correction factor (C) for ferritic steel (EN 13445-3, 2014)

$$C = 1.03 - (1.5 \cdot 10^{-4} \cdot T) - (1.5 \cdot 10^{-6} \cdot T^2), \tag{5.2}$$

where T is the elevated temperature (in ^{o}C). Substituting the operating temperature +335 ^{o}C into Equation (5.2), the stress correction factor becomes 0.81. The FAT curve at the elevated temperature can be generated by multiplying values of the FAT_{20} curve (corresponding to 20 ^{o}C) by the stress concentration factor C.

Quite a similar result is achieved by using Equation 5.3 (Hobbacher, 2016a)

$$FAT_{HT} = FAT_{20} \cdot \frac{E_{HT}}{E_{20}}, \tag{5.3}$$

where FAT_{HT} is the reduced value of the fatigue class at an elevated temperature and FAT_{20} the fatigue class at room temperature, and E_{20} and E_{HT} are the corresponding Young's moduli. For the material P265GH used in this study, $E_{20} = 210\,000$ MPa (at +20 ^{o}C) and $E_{HT} = 172\,000$ MPa (at +335 ^{o}C). Substituting these numerical values for the Young's moduli, we get the correction factor 0.82 for FAT_{HT}.

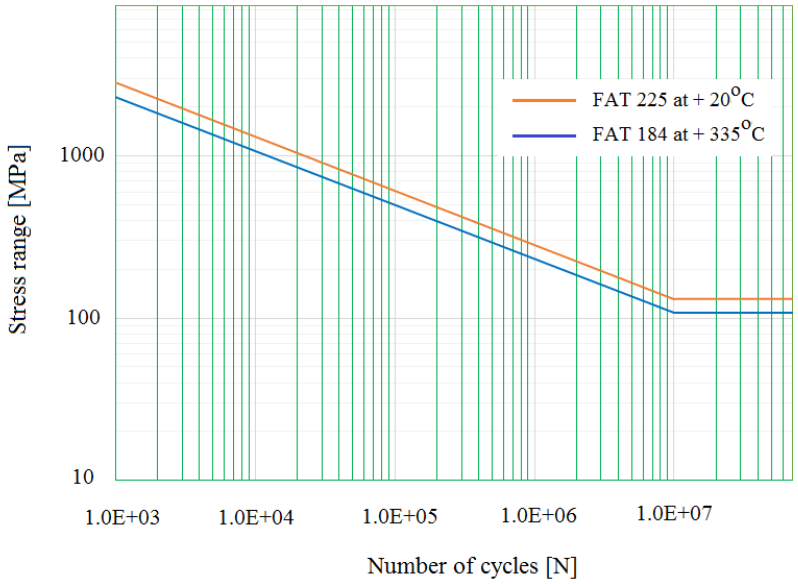

Figure 5.11: The FAT curves at room and elevated temperatures +20 ºC and +335 ºC, respectively. The curves are valid for the effective notch stress method.

According to ENS approach, recommended absolute sizes of elements on the curved surface are ≤ 0.25 mm for parabolic elements and ≤ 0.15 mm for linear elements, respectively, when using the reference radius of $r = 1.0$ mm for the curved surface (Hobbacher, 2016b).

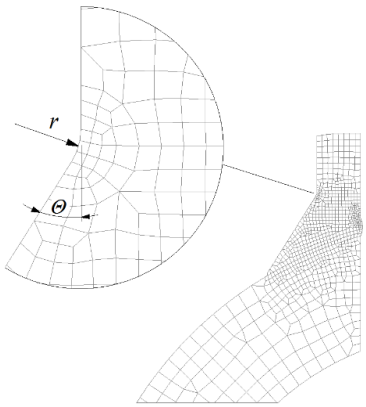

Figure 5.12: A detail of the local fine mesh of the FE model at the junction. The radius $r = 1.0$ mm and the flank $\theta = 32$ °.

5.2.2 Linear elastic fracture mechanics approach, LEFM

The goal in the LEFM approach is to determine stress intensity factors (SIFs) as a function of the crack size, length or depth. The SIFs indicate the probability of cracking. The weight function can be determined from a stress distribution through the wall thickness. The stress values are picked up along the chosen path as shown in Figure 5.13.

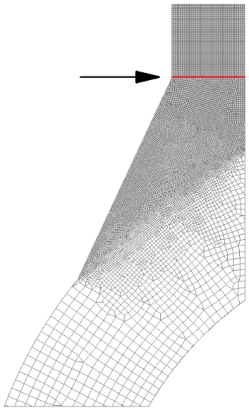

Figure 5.13: Stress distribution path chosen for the LEFM analysis.

The fatigue life is estimated by using an uncracked FE model to get the number of cycles $N_{f,FEM,WF}$ with weight function WF (Hobbacher, 2016c) and using an analytical crack growth based on the Paris model (Dowling, 1999).

The crack length grows from the initial crack length a_i to the final crack length a_f of final fracture. At the elevated temperature HT the elastic modulus decreases relative to the reference $+20\,^{o}\mathrm{C}$ temperature. This temperature effect on the number of cycles $N_{f,WF}$ can be taken into account using the ratio of the Young's moduli. According to the Paris model one gets

$$N_{f,WF} = \int_{a_i}^{a_f} \frac{da}{\left(\frac{E_{20}}{E_{HT}}\right)^{m} \cdot C_0 \cdot [K_a(a)]^m} \tag{5.4}$$

where the stress intensity factor K_a is a function of the current crack length a, m is the appropriate exponent, and C_0 the constant of the power law.

The stress intensity factor has the form

$$K_a(a) = \int_0^a \sigma(x) M_a(x,a) dx \tag{5.5}$$

where $\sigma(x)$ is the stress distribution through the wall thickness as presented in Figure 5.13 and $M_a(x,a)$ the weight function for the intensity factor at the deepest point.

The weight function for the stress intensity factor is ($0 < x < a$)

$$M_a(x,a) = \frac{2}{\sqrt{2\pi(a-x)}} \cdot \left[1 + M_{1,a}\left(1-\frac{x}{a}\right)^{\frac{1}{2}} + M_{2,a}\left(1-\frac{x}{a}\right) + M_{3,a}\left(1-\frac{x}{a}\right)^{\frac{3}{2}}\right] \tag{5.6}$$

where the required constants are (Hobbacher, A.F., 2016)

$$\begin{aligned}
M_{1,a} &= 3.1415 \cdot (4 \cdot Y_0 - 6 \cdot Y_1)/\sqrt{2 \cdot Q} - 24/5 \\
M_{2,a} &= 3 \\
M_{3,a} &= 2 \cdot \left(3.1415 \cdot Y_0/\sqrt{2 \cdot Q} - M_{1,a} - 4\right) \\
Y_0 &= B_0 + B_1 \cdot (a/t)^2 + B_2 \cdot (a/t)^4 \\
Y_1 &= A_0 + A_1 \cdot (a/t)^2 + A_2 \cdot (a/t)^4 \\
Q &= 1 + 1.464 \cdot (a/c)^{1.65} \\
A_0 &= 0.456128 - 0.114206 \cdot (a/c) - 0.046523 \cdot (a/c)^2 \\
A_1 &= 3.022 - 10.8679 \cdot (a/c) + 14.94 \cdot (a/c)^2 - 6.8537 \cdot (a/c)^3 \\
A_2 &= -2.28655 + 7.88771 \cdot (a/c) - 11.0675 \cdot (a/c)^2 + 5.16354 \cdot (a/c)^3 \\
B_0 &= 1.1019 - 0.019863 \cdot (a/c) - 0.043588 \cdot (a/c)^2 \\
B_1 &= 4.32489 - 14.9372 \cdot (a/c) + 19.4389 \cdot (a/c)^2 - 8.52318 \cdot (a/c)^3 \\
B_2 &= -3.03329 + 9.96083 \cdot (a/c) - 12.582 \cdot (a/c)^2 + 53462 \cdot (a/c)^3
\end{aligned} \tag{5.7}$$

In Equations 5.7 the coefficients *a* and *c* are the minor and major axes of the ellipse, respectively.

The nominal fatigue classes (FAT) for each of the cases are solved according to

$$FAT_{,nom} = \sqrt[m]{\frac{N_{f,WF}}{2 \cdot 10^6}} \cdot \sigma_{nom} \tag{5.8}$$

where σ_{nom} is the nominal stress acting far from the branch joint, i.e., $\sigma_{nom} = \sigma_{m1} + \sigma_{b1}$ (see Figure 5.10).

5.3 Results of FEA

In the branch tube the bending moment M_z produces membrane stresses (σ_{m1} , σ_{m2}), bending stresses (σ_{b1} , σ_{b2}), and a non-linear peak stress (σ_{nl}) as shown in Figure 5.10. The membrane stress is the average stress value across the thickness of the solid section. The bending stress is a component of primary stress proportional to the distance from the centroid of the solid. The peak stress (σ_{nl}) is the highest stress at some local point within the considered area. In the effective notch stress approach, this stress is obtained by using an 1.0 mm radius of curvature at the points of interest. The stress concentration factor K_t and stress structural concentration factor K_s at the junction can be deduced from Figure 5.10. The membrane stress concentration factor K_{sm} is

$$K_{sm} = \frac{\sigma_{m2}}{\sigma_{m1} + \sigma_{b1}} = \frac{\sigma_{m2}}{\sigma_{nom}} \tag{5.9}$$

where σ_{m1} and σ_{m2} are the membrane stresses of Figure 5.10. The bending stress concentration factor K_{sb} is

$$K_{sb} = \frac{\sigma_{b2}}{\sigma_{m1} + \sigma_{b1}} = \frac{\sigma_{b2}}{\sigma_{nom}} \tag{5.10}$$

where σ_{b1} and σ_{b2} are the bending stresses of Figure 5.10. The stress value for ENS is the sum of membrane, bending, and non-linear peak stresses including stress concentration factors, that is

$$\sigma_{ENS} = K_{sm}\sigma_{nom} + K_{sb}\sigma_{nom} + \sigma_{nlp} \quad (r = 1 \text{ mm}) \tag{5.11}$$

The total notch stress concentration factor K_t is

$$K_t = \frac{\sigma_{ENS}}{\sigma_{HS}} \tag{5.12}$$

where σ_{HS} is the structural hot-spot stress. Above, the nominal stress range σ_{nom} is due to a varying bending moment M_z. For ENS-applications one can write (see Equation (5.1))

$$\Delta M_{eq} = \left(\frac{\sum_{i=1}^{k} \Delta M_i^m n_i}{\sum n_i} \right)^{\frac{1}{m}} \tag{5.13}$$

The total structural concentration factor K_s can be deduced in a similar manner. The non-linear peak stress, however, is ignored. Thus

$$K_s = \frac{\sigma_{HS}}{\sigma_{nom}} \tag{5.14}$$

The hot-spot stress σ_{HS} can be determined by two different ways. The most accurate way is to determine a stress distribution through the thickness and integrate the membrane and bending stresses from the stress distribution. The sum of the integrated stresses represents the structural stress, i.e., the hot-spot stress.

The membrane stresses σ_{m1} and σ_{m2} are obtained from the equation $(i = 1,2)$

$$\sigma_{mi} = \frac{1}{t} \cdot \int_0^t \sigma(x, y_i) \cdot dx \tag{5.15}$$

and the shell bending stresses σ_{b1} and σ_{b2} from the equation $(i = 1,2)$

$$\sigma_{bi} = \frac{6}{t^2} \cdot \int_0^t [\sigma(x, y_i) - \sigma_{mi}] \cdot \left(\frac{t}{2} - x\right) \cdot dx \tag{5.16}$$

From the fatigue life predictions obtained using WF and ENS approaches, the following FAT classes at two million cycles can be obtained for the nominal stress and structural hot-spot stress approaches. The nominal fatigue class of ENS is

$$FAT_{nom,ENS} = \sqrt[m]{\frac{N_{f,ENS}}{2 \cdot 10^6}} \cdot \sigma_{nom} \tag{5.17}$$

whereas the nominal fatigue class of WF is

$$FAT_{nom,WF} = \sqrt[m]{\frac{N_{f,WF}}{2 \cdot 10^6}} \cdot \sigma_{nom} \tag{5.18}$$

Similarly, the hot-spot class of ENS is

$$FAT_{HS,ENS} = \sqrt[m]{\frac{N_{f,ENS}}{2 \cdot 10^6}} \cdot \Delta\sigma_{HS} \tag{5.19}$$

whereas the hot-spot class of WF is

$$FAT_{HS,WF} = \sqrt[m]{\frac{N_{f,WF}}{2 \cdot 10^6}} \cdot \Delta\sigma_{HS} \tag{5.20}$$

where $\Delta\sigma_{HS}$ is the stress amplitude obtained from the hot-spot method. In Tables 5.5 and 5.6 the FAT classes and stress concentration factors for each branch tube size (see Table 5.4) are presented.

Table 5.5: FAT classes at weld toes for each branch tube size.

outside diameter [mm]	wall thickness [mm]	$FAT_{nom,ENS}$	$FAT_{nom,WF}$	$FAT_{HS,ENS}$	$FAT_{HS,WF}$
33.7	5.0	88	52	151	89
33.7	6.3	89	56	139	88
33.7	7.1	88	58	133	88
51.0	5.0	71	45	147	92
51.0	6.3	74	48	142	91
51.0	7.1	76	50	137	90
70.0	5.0	90	52	161	93
70.0	6.3	81	50	149	92
70.0	8.0	76	46	154	93

Table 5.6: Stress concentration factors K_t and K_s and the degree of bending (DOB) for each branch tube size.

outside diameter [mm]	wall thickness [mm]	K_t	K_s	$K_t K_s$	DOB
33.7	5.0	1.32	1.71	2.27	0.49
33.7	6.3	1.43	1.57	2.25	0.47
33.7	7.1	1.51	1.51	2.28	0.47
51.0	5.0	1.36	2.06	2.80	0.53
51.0	6.3	1.42	1.90	2.70	0.52
51.0	7.1	1.46	1.79	2.62	0.50
70.0	5.0	1.25	1.78	2.23	0.42
70.0	6.3	1.34	1.83	2.45	0.44
70.0	8.0	1.30	2.01	2.61	0.51

Figures 5.14 and 5.15 present the membrane stress, bending stress and non-linear peak stress distributions in the through thickness direction at the weld toe of the branch tube for the tube with the dimensions d_o and t (Figures 5.10 and 5.13). Normalized values are determined by dividing calculated stress value with nominal stress value.

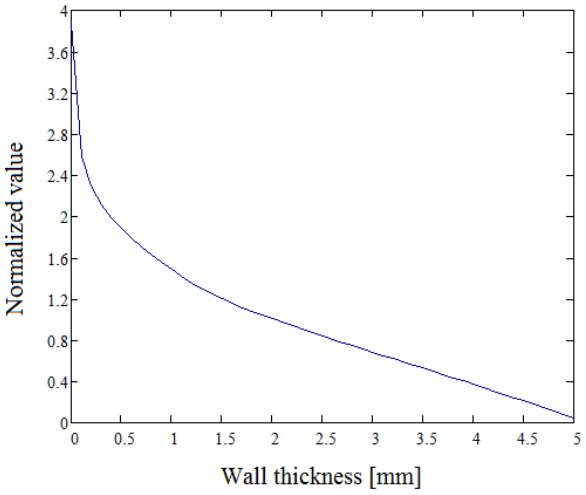

Figure 5.14: Longitudinal stress distribution along the line thru the tube wall (see Figure 5.13) for $D_o = 88.9$ mm, $T = 12.5$ mm, $d_o = 51.0$ mm. For other values of d_o the curve is almost similar.

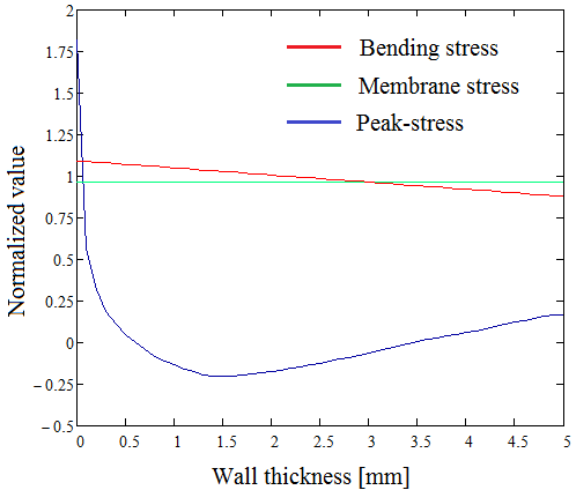

Figure 5.15: Stress components calculated from the longitudinal stress distribution of Figure 5.14. The non-linear peak stress occurs due to the discontinuity of the geometry.

It can be concluded from Figure 5.15 that the stresses are higher on the outer surface of the shell. This means that fatigue lives are less on the outer surface than on the inner surface. This phenomenon was noted in Section 3.4 (Figure 3.11).

5.4 Sensitivity analysis

The aim of this section is to obtain a useful regression model to predict the value of the stress concentration factor *K* for different diameter and thickness ratios of the header and branch tube in the neighbourhood of previously solved cases. The diameter and thickness ratios of the header and branch tube and the function for the stress concentration factor are denoted by

$$x = \frac{D_0}{d_0} \quad , \quad y = \frac{T}{t} \quad , \quad K_t K_s = K(x, y) \tag{5.21}$$

The model for the function *K* can be derived using a statistical non-linear regression model. Non-linear terms increase the accuracy of model predictions, but the model is not easy to solve. Therefore, the non-linear regression model is transformed into a linear one by adding extra variables. It is easy to solve, since its parameters can be solved by inversion of a square matrix (Montgomery et al., 2005). The required data for the regression model is given in Table 5.7.

Table 5.7: Data for the regression model taken from Table 5.6 (D_0 = 88.9 mm, T = 12.5 mm).

Branch tube d_o [mm]	Branch tube t [mm]	D_o/d_o [-]	T/t [-]	K *) [-]
33.7	5.0	2.64 = x_{11}	2.50 = x_{12}	2.27 = K_1
33.7	6.3	2.64 = x_{21}	1.98 = x_{22}	2.25 = K_2
33.7	7.1	2.64 = x_{31}	1.79 = x_{32}	2.28 = K_3
51.0	5.0	1.74 = x_{41}	2.50 = x_{42}	2.80 = K_4
51.0	6.3	1.74 = x_{51}	1.98 = x_{52}	2.70 = K_5
51.0	7.1	1.74 = x_{61}	1.79 = x_{62}	2.62 = K_6
70.0	5.0	1.25 = x_{71}	2.50 = x_{72}	2.23 = K_7
70.0	6.3	1.25 = x_{81}	1.98 = x_{82}	2.45 = K_8
70.0	8.0	1.25 = x_{91}	1.56 = x_{92}	2.61 = K_9

*) The following notation has been used: $x_{i1} = x_i$, $x_{i2} = y_i$, $K_i = K(x_i, y_i)$ for $i = 1, \dots, 9$.

The general second order non-linear model is linearized by extending the number of variables in the following way:

$$\begin{bmatrix} x_{i1} \\ x_{i2} \\ x_{i3} \\ x_{i4} \\ x_{i5} \end{bmatrix} = \begin{bmatrix} x_{i1} \\ x_{i2} \\ x_{i1}x_{i1} \\ x_{i2}x_{i2} \\ x_{i1}x_{i2} \end{bmatrix} \quad (i = 1, \dots, 9) \tag{5.22}$$

The linear regression model is now

$$K_i = b_0 + \sum_{j=1}^{5} x_{ij} b_j + \ \epsilon_i \quad (i = 1, \dots, 9) \tag{5.23}$$

where the quantities b_j are model parameters and ϵ_i modelling errors. This can be written compactly as

$$\mathbf{K} = \mathbf{Xb} + \boldsymbol{\epsilon} \tag{5.24}$$

and the optimal **b**-vector is solved as

$$\hat{\mathbf{b}} = (\mathbf{X}^{\mathrm{T}}\mathbf{X})^{-1}\mathbf{X}^{\mathrm{T}}\mathbf{K} \tag{5.25}$$

The fitted regression model with minimal error is

$$\hat{\mathbf{K}} = \mathbf{X}\hat{\mathbf{b}} \tag{5.26}$$

The structure of these equations can be illustrated explicitly as

$$\boldsymbol{K} = \begin{bmatrix} K_1 \\ K_2 \\ K_3 \\ K_4 \\ K_5 \\ K_6 \\ K_7 \\ K_8 \\ K_9 \end{bmatrix} = \begin{bmatrix} 1 & x_{11} & x_{12} & x_{13} & x_{14} & x_{15} \\ 1 & x_{21} & x_{22} & x_{23} & x_{24} & x_{25} \\ 1 & x_{31} & x_{32} & x_{33} & x_{34} & x_{35} \\ 1 & x_{41} & x_{42} & x_{43} & x_{44} & x_{45} \\ 1 & x_{51} & x_{52} & x_{53} & x_{54} & x_{55} \\ 1 & x_{61} & x_{62} & x_{63} & x_{64} & x_{65} \\ 1 & x_{71} & x_{72} & x_{73} & x_{74} & x_{75} \\ 1 & x_{81} & x_{82} & x_{83} & x_{84} & x_{85} \\ 1 & x_{91} & x_{92} & x_{93} & x_{94} & x_{95} \end{bmatrix} \begin{bmatrix} b_0 \\ b_1 \\ b_2 \\ b_3 \\ b_4 \\ b_5 \end{bmatrix} \tag{5.27}$$

The above problem can be solved using a suitable algorithm. In this case a built in function in the Excel software was used (Excel, 2013).

In this way, the solved function for K becomes

$$K(x, y) = 2.15 + 2.64x - 1.77y - 0.83x^2 + 0.29\,y^2 + 0.24xy \tag{5.28}$$

In the figure below the surface obtained using Equation (5.28) is presented.

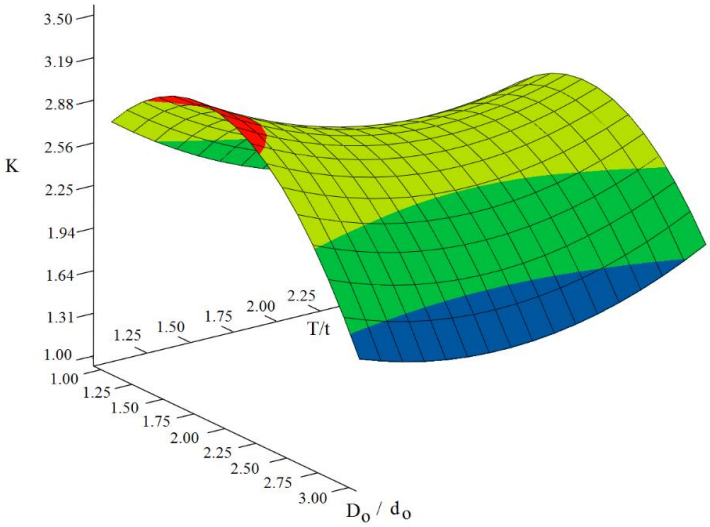

Figure 5.16: 3D surface for *K* as a function of D_o/d_o and T/t.

The correctness of Equation 5.28 was verified by a new FE model. The values $d_o =$ 42.4 mm and $t = 5.5$ mm for the calculation were chosen. By substituting these values into Equations 5.21 and 5.28 we get 2.66 for the stress concentration factor while the corresponding value from FEA is 2.71.

6 Discussion

The aim of this section is to summarize the findings and critically evaluate the importance, accuracy and reliability of the achieved results. The efficiency of the recovery boiler is partly based on a successful sootblowing. An optimal result is a trade-off between the amount of removed ash and the fatigue durability of the tube joints. The amount of ash can be controlled by indirect measurements from the hanger rods, and the accumulation of damage by the developed theoretical calculation models. The goal is to analyze separately the accuracy of the measurement device and the reliability of the computational models. At the end of this chapter, some goals for future research projects are presented.

6.1 Ash measurements of the heat surfaces

Presently, the amount of sooting is monitored using external measurements of various quantities, such as the pressure drop in the exhaust ducts, the rotation speed changes of the exhaust gas fans, the output temperatures of the boiler banks and the superheaters, and the amount of cooling water of the superheated steam (Penttinen, 2018). By using the results of the above mentioned measurements, a rough approximation for the amount of ash to be removed by soot blowing can be determined mathematically.

A much more accurate estimate is obtained by measuring directly the changes of strains in the hanger rods. These strains are proportional to the loading masses. By combining the measurement information obtained from each hanger rod, it is possible to obtain information on the ash distribution on the heat surfaces in the horizontal direction. This data shows also in real time the amount of ash to be removed. Most control systems allow manual controlling of the individual sootblowers. By this method it is possible to monitor the ability of each sootblower to remove ash from their apportioned target areas.

There are many different factors involved in the operation of a recovery boiler, which can cause inaccuracy to the measured results of the hanger rods. It is not always possible to eliminate all of these factors beforehand due to the demanding environment. The factors that can cause errors in measurement results are the heat surface displacements and twists caused by uneven heat distribution, elastic behaviour of supporting beams etc.

It was discovered in this study that the own weight of the thermal surfaces has a positive effect on the measurement results. This was evident in the tests carried out by loading the hanger rod with different test forces. According to Figure 4.9, the results of the elongation of the tension ring at higher force values correspond well to the results obtained from the FE calculations. Moreover, the full-scale measurements at the site showed that some of the hanger rods were loosened after prolonged use and they had not been re-checked for tension after the boiler was put into operation. In these cases, the ash mass on the thermal surfaces was distributed over those hanger rods that had remained tight. No results could be obtained from the loosened hanger rods. Therefore,

all the hanger rods must be pre-tightened similarly before installing the measuring device.

The device gives measurement results which are approximate due to various factors. In Chapter 4 the design principle of the ring was described. It is based on the theory of curved beams. According to theoretical models, the influence of the shear and normal forces on the total strain at the measurement location is less than 1 % and they can be ignored. Therefore, their effect in the measurement results can be neglected. The effect of the changes in the ambient temperature can be eliminated by manufacturing the device from the same material as the hanger rod. By this choice the thermal length changes of the bar and ring, and the hanger rod, are always the same and do not affect the measurement results.

However, these results are still sufficiently accurate for the evaluation of the efficiency of the soot blowers. In general, it is more important to view the graphs of trends in ash mass change rather than to examine the exact amount of ash that has been removed. The reliability of the measurement results becomes more accurate the longer the data is collected and analysed for.

The disadvantage of the current measuring device is that it cannot be used to determine the location of the ash on the heat transfer surfaces in vertical direction. Theoretically, the location of ash can be determined from the measured data of the hanger rods by using the Fourier transform. However, this method has not been used in this study. In addition to the Fourier method, other measured data from the boiler, such as pressure, temperature, and composition of the combustion gases can be used for determining the location of the ash. It is more likely to achieve a better result by combining different measured data than using just one measurement result.

During testing disturbances were observed when the steam lance jet hit the heat surfaces and excited the platens, which caused vibrations in the thin tension bars attached to the tension rings. This phenomenon showed up clearly as a disturbance in the measurement signal, and it was reduced notably by attaching an additional sliding support between the clamps. It allowed the bar to move back and forth in the axial direction of the tension bar preventing effectively horizontal movements.

The conclusion to be drawn is that the joint between the tension bar and tension ring should be designed so as to function cinematically as a ball joint which does not transmit any bending moments. In the present version of the device the joint is made so that the ring is between two nuts. Excessive tightening of the nuts deforms the ring from circle to ellipse. This causes the measured strains to deviate from the theoretically correct value based on the circle form. Best results in reducing the disturbances were obtained by attaching the tension bar to the tension ring so that there was an air gap of approximately 0.1 mm between the nut and the ring. Then the device was pretightened using the nut inside the ring.

Based on the results, it was found that increasing the diameter of the tension bar improves the sensitivity of the measuring device. The sensitivity of the measuring device can also be improved by increasing the distance between the attachment points,

which is directly proportional to the translations between them. The applied force in the tension bar, and the distance between the tension bar and the hanger rod try to bend the hanger rod causing errors in the measurement results. This effect can be decreased by making the clamp more rigid, i.e., increasing the thickness of the clamp and minimizing the distance between the tension bar and the hanger rod. The related calculations are presented in Appendix A.

According to the theory of curved beams (Timoshenko, 2010), the tensile ring can be regarded as a slightly curved beam and the simple theory of straight beams can be applied. The numerical error of this approximation is negligible due to the small ring thickness used. According to the straight beam model, the absolute values of the inner and outer beam stresses are equal. By multiplying the measured strains by the elastic modulus of the ring, the ring stresses on both surfaces are obtained. The relevant calculations are presented in Appendix A.

In the studied case the strain gages were attached to the opposite sides of the ring to form a full bridge. Advantages obtained by this arrangement are temperature compensation, elimination of the effect of the normal force, and improved sensitivity. An alternative or even better arrangement is to attach the strain gages to both sides of the ring. Using such an arrangement, it is possible to eliminate the errors in the bending stress of the ring due to the eccentric assembly of the bar. However, this option would have been much more expensive since it would have necessitated an additional protection to the wire.

Testing was used to study the influence of a possible assembly misalignment of the device on the measurement results. The clamps around the hanger rod were rotated to effect on angular deviation of the axis of the tension bar from the axis of the hanger rod. The measurement results for this intentionally incorrect assembly were compared with those of a correct assembly with parallel axes. It was observed that the angular deviations influenced the results significantly only when they were larger than 3°. In order to remove the error, a special accessory equipment has been developed to minimize the effect of the eccentricity. Using it the assembly can be adjusted accurately enough with an angular deviation of $\pm 0.1°$ only. In addition, there are several sources of error such as misalignment of strain gages, long wiring, bridge voltage, accuracy of the DAQ etc. These errors can be minimized by calibrating each measurement device separately with a known exact weight.

The measured data can be utilized in various applications. However, consideration of those prospects is outside the scope of this work. One promising prospect is the possibility to increase the efficiency of burning. For the time being, the measurement device can be utilized profitably to estimate the amount of ash on the heat surfaces. The distribution of soot vertically along the platens is not feasible by this method.

6.2 A surrogate beam model

When a complete detailed shell element FE model is used, the solution time usually becomes long. A small improvement to the solution speed can be achieved by changing control parameters such as the time step etc. A much more efficient approach is obtained by using a surrogate beam model. The results between the shell and beam model have been compared and the difference in the calculated equivalent constant bending amplitude moment values at the tube branch joint is about 5 %. In addition, five lowest eigenfrequencies and mode shapes are solved using the beam and shell models. These values are very close to the measured values. The results are presented in Table 5.2.

In some cases it may be justified to write a script for a commercial software such as MATLAB or Mathcad instead of using the FE programs. This is very useful, for example, when studying cases with several different sootblowing sequences. In Appendix D the stiffness and mass matrices, including the distortion effect due to torsion, and a closed form solution for the warping constant are derived.

6.3 Fatigue damages

The fatigue endurance of the tube branch joints was estimated by three different methods, the effective notch method, linear fracture mechanics, and the hot spot method. Nine different cases were considered. The geometric variables in the FEM calculations were chosen as the outer diameter and wall thickness of the branch tube. According to the FE analyses, the crack initiation location was along the boundary line starting at the saddle point. This prediction of the crack initiation location agreed with the results of failure reports. By studying various loading cases it was observed that this damage was caused by the bending moment acting on the branch pipe.

The fatigue calculations for the branches were conducted using a constant amplitude moment load. Its magnitude was changed to such a value that in all cases it produced the same 100 MPa nominal stress to the branch joint. The goal of this procedure was to make the results comparable with each other. In practice, it is difficult to obtain reliable estimates for the loads on the branch joints by measurements.

Using the calculated results, the fatigue class (FAT) for each tube joint geometry was determined by using different fatigue approaches. A comparison of the results shows that the calculated fatigue class value for each approach changes consistently with the size of the single branch tube. The lowest values of the fatigue class were obtained by a combination of nominal stress and weight function used in fracture mechanics. The highest values for fatigue classes were obtained by a combination of hotspot and effective notch stresses. These two methods are based on different assumptions, which can have a remarkable effect on the results. In fracture mechanics, the structure has presumably an initial crack and the computation proceeds to propagate the crack. Therefore, the weight function does not take into account the initiation of crack propagation. In the weight function method, in turn, the selection of the initial crack

size has a significant effect on the results. In this study, the excitations were chosen by a random selection of the loading sequences. Naturally, the real excitations should be used when they are available. According to the calculated results, the selection of the soot blowing sequence influences greatly the fatigue life. In the studied cases, the most non-optimal sequence gave only 39% of the life time of the optimal sequence.

6.4 Sensitivity analysis

In practice, the internal diameter of the tubes is determined by using criteria from process engineering, and the tube wall thickness will be calculated by using the design values of pressure, material and temperature analyses. Depending on the case, several options for the diameter and thickness ratios of the tube branch joints are possible. For this reason, the sensitivity analysis was developed to find out the stress concentration factor for the chosen diameter and thickness ratios. The result of Equation 5.28 was compared to the result of the corresponding FE-model and it was found that the results are close to each other.

6.5 Future work

In future projects, the goal may be to obtain measured data from the hanger rods using a long enough measurement time to increase the reliability of the results. One project can be activated to find out whether the measured data can be used to calculate the ash distribution also in the vertical direction along each heat surface. Some preliminary calculations have been made and the results are promising. In this work it was studied how the branch tube diameter and wall thickness influenced the fatigue life of the joint. In future projects the goal is to study possibilities for increasing the fatigue life of the joint by changing the present circular cross section of the branch tube to an elliptic one.

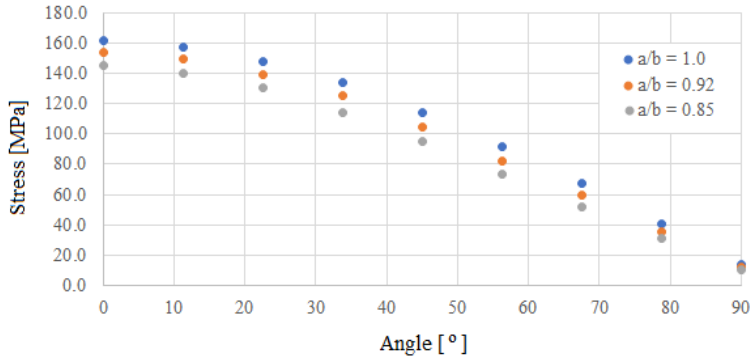

Figure 6.1: Maximum principal stress along the red line from the saddle point to the crown point (see Figure 6.3) for different ratios *a*/*b*.

According to preliminary calculations, this cross section shape change increases notably the fatigue life. Figure 6.1 shows stress results obtained from a joint subjected to a bending moment. The bending moment produced a nominal stress of 100 MPa at the branch tube. The maximum principal stress is shown as a function of the angle from the saddle point to the crown point. Three different values for the ratio *a*/*b* of the minor to major axis of the ellipse are used (*a*/*b* =1 means circular). In the FE analyses the branch tube diameter was 51.0 mm and the wall thickness 5.0 mm.

Figure 6.2 shows the maximum principal stress for three different values of the ratio *a*/*b* of the branch tube. The stress is read starting from the saddle point along the branch tube about 70.0 mm upwards. Figure 6.3 shows the paths along which the stress values are read.

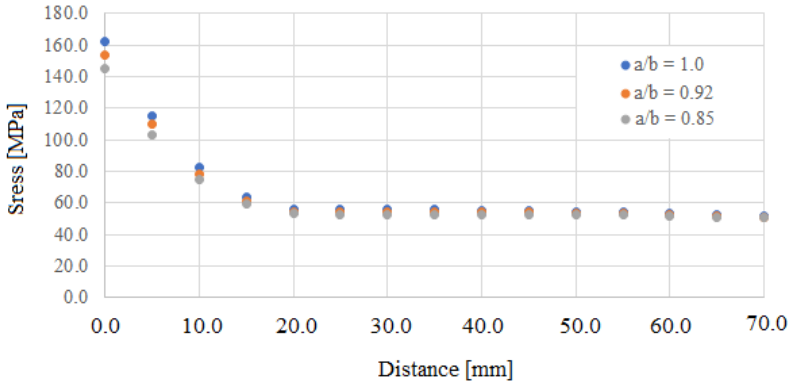

Figure 6.2: Maximum principal stress from the saddle point upwards along the branch tube (blue line in Figure 6.3) for different ratios *a*/*b*.

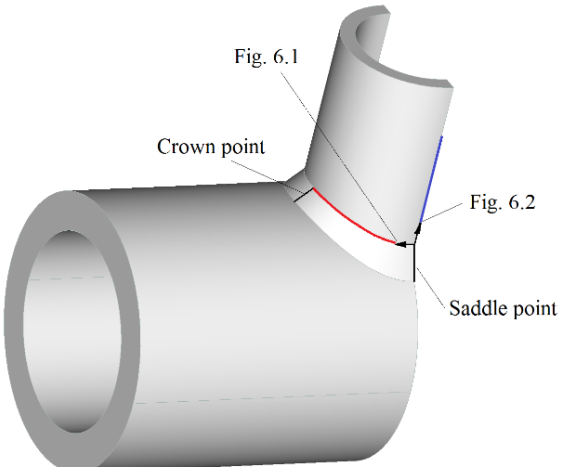

Figure 6.3: Paths along which the stress values are read.

It can be seen from Figures 6.1 and 6.2 that the saddle point is the most critical point with respect to fatigue failures when the branch tube is subjected to a fluctuating bending moment caused by the bending vibrations of the heat surface. The results show that the stress values at the saddle point are decreasing for smaller *a*/*b*- ratios. For the ratio *a*/*b* = 0.85, the fatigue durability increases approximately 32% compared with a circular cross section.

Tests were carried out by using the circular ring only as discussed in Chapter 4. Based on the FEA results, it can be seen that the geometric discontinuities increase the strain values in the hoop direction of the rings. Three different options are shown in Figure 6.4. It can be seen that the ring of the case (c) is the most sensitive in terms of hoop strain.

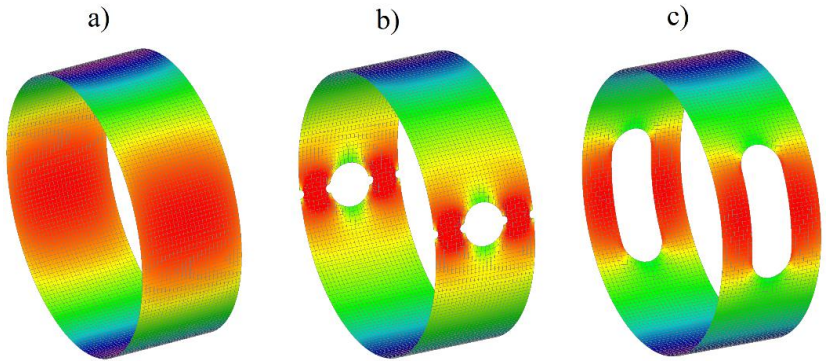

Figure 6.4: Strains in tension rings including geometric discontinuities in the form of holes.

The ratios of the maximal strains in the hoop direction of the cases (a), (b) and (c) are 1.0 : 8.2 : 23.3, respectively. In Figure 6.4 only a few possibilities for improving the sensitivity of the tension ring are illustrated and they may not represent the most optimal solution.

The measuring device has been installed in two recovery boilers in Finland. The analysis of the measured data is still at an early stage the potential of which will be explored further. Using artificial intelligence (AI) with the measured data can be one way to improve the cleaning procedure of heat transfer surfaces.

7 Conclusions

This thesis examined the control and safety of sootblowing, i.e., removal of deposits from recovery boiler heat surfaces. The thesis had several goals. The technical goal of this thesis was to develop a measurement device to predict the need for sootblowing by using information of the measured ash mass changes on the heat surfaces. Generally speaking, it is more important to control the function of the sootblowers with a measured trend, than to accurately evaluate the ash mass in kilograms on the heat surfaces. This goal was achieved well as proved by the results of this thesis. By the aid of the measurement device a targeted soot blowing operation can be performed.

In addition, other precise requirements were set for the measurement device as a simple construction to be manufactured, installed and operated. Preliminary tests showed that there are a few important things to be considered in the use of the device. Especially, in older recovery boilers some hanger rods may have become loose and they must be tightened before installing the measurement device. Calibration can be done after water washing of the heat surfaces, when the boiler has achieved the normal operation circumstances.

The excitation due to sootblowing leads to vibrations of the heat surfaces, which can lead to fatigue damages in the tube branches. The risk of the damages can be estimated and reduced using the user-friendly FE-software developed for this purpose in this thesis. The cost-effective version of this model utilized effectively the warping stiffness and mass matrices, and the warping constant in closed mathematical form, derived in this thesis. It can be used to analyze different load variations quickly and to select the optimal solution based on them. In particular, an optimal sooting sequence can be found by the aid of this dynamical model. In usual engineering practice, the dimensions of the tube branches are chosen mainly based on the process design data, so that the dimensioning is not specifically against fluctuating loadings. In this thesis, an optimal design against fluctuating loadings was achieved by using the diameter and wall thickness ratios of the header and the branch tube as design variables. The result was a general regression model for stress concentration. Below is the summary of the key points based on experimental measurements together with statistical analysis and numerical FE modelling:

- Real- time ash mass changes on the heat surfaces can be monitored by measuring devices, which are installed on the hanger rods.

- A computational algorithm was developed for analyzing the effect of the excitation due to sootblowing. This algorithm will give an approximation for the loadings accurate enough for further durability analyses of the heat surfaces at the critical locations, reducing significantly the calculation time.

- There are many alternatives to manufacture the tube joints by using different geometric variables, such as the tube diameter or thickness. By using sensitivity analysis, based on the FEA of the tube branch connections, the stress concentration factor can be determined for the case under consideration without the need for a special FE analysis.

- The fatigue durability of the tube branch connection can be increased by forming the cross section of the branch tube. According to FEA, even a weakly elliptical shape can significantly improve the fatigue resistance.

The scope of this work led to the exclusion of many interesting subjects, such as estimating the vertical ash mass distribution on the heat surfaces, and measuring the excitation caused by the steam of the sootblowers. These will be explored in future research projects.

References

1. Adams, V. & Askenazi, A., 1999. Building better products with Finite Element Analysis. OnWord Press, Santa Fe, NM 87505-4835 USA, pp. 84-86.
2. Almar-Næss, A., 1999. Fatigue Hanbook. Offshore Steel Structures. Tapir trykkeri, pp. 204-205.
3. Anderson, T.L., 2005. Fracture Mechanics. Fundamentals and Applications, pp. 12-21.
4. ASME 2009., Boiler & Pressure Vessel Code. Part I, rules for construction of power boilers. The American Society of Mechanical Engineers.
5. Bajpai, P., 2017. Pulp and paper industry. Elsevier 2017, p.260.
6. Bathe, K-J., 1996. Finite Element procedures. Prentice-Hall International, Inc., pp. 796-800.
7. Blevins, R.D., 2001. Flow-Induced Vibration, 2nd edition. Krieger publishing company. Malabar, Florida, 2001, pp. 326-327.
8. Capablo, J. & Salvadó, J., 2016. Estimating heat transfer losses caused by alkali salt deposits in biomass combustion. Renewable Energy, Vol. 105, May 2017, pp. 449–457.
9. Chapra, S.C. & Canale, R.P., 2006. Numerical Methods for Engineering, 5th edition. Mc Graw Hill, pp. 85-89.
10. Cook, R.D., Malkus, D.S., Plesha, M.E. & Witt, R.J., 2002. Concepts and applications of finite element analysis, 4th edition. John Wiley & Sons, Inc., pp. 574-583.
11. Doroudi, S., Pophali, A., Bussmann, M., Tandra, D., Tran, H. Modelling sootblower jet effectiveness with Ansys fluent., 2015. ResearchGate, p. 7
12. Dowling, N. E., 1999. Mechanical behavior of materials. Engineering Methods for Deformation, Fracture, and Fatigue, Second Edition, pp. 488-497.
13. EN 13445-3, 2014. Unfired pressure vessels- Part 3: Design. Brussels: European Committee for Standardization (CEN).

14. Excel, 2013. Microsoft Office Excel software 2013.

15. Frederick, W. J. Jr. & Vakkilainen, E. K., 2002. Control and prediction of fouling in large recovery boilers. 7th International Conference on New Available Technologies, SPCI 2002, Stockholm, p. 5.

16. Frederick, W. J. Jr. & Vakkilainen, E. K., 2003. Sintering and structure development in alkali metal salt deposits formed in kraft recovery boilers. Energy & Fuels, Vol. 17, No. 6, November 2003, pp. 1501–1509.

17. Gullichsen, J. & Fogelholm, C-J., 2000. Chemical pulping, Book 6B. Gummerus printing, pp. 95-99.

18. Hobbacher, A.F., 2016a. Recommendations for Fatigue Design of Welded Joints and Components, Second Edition. International Institute of Welding, p. 71.

19. Hobbacher, A.F., 2016b. Recommendations for Fatigue Design of Welded Joints and Components, Second Edition. International Institute of Welding, p. 29.

20. Hobbacher, A.F., 2016c. Recommendations for Fatigue Design of Welded Joints and Components, Second Edition. International Institute of Welding, pp. 125-126.

21. Hughes, T., 2000. The Finite Element Method. Linear Static and Dynamic Finite Element Analysis. Dover Publications, Inc. pp. 120-126.

22. Jameel, M.I., Cormack, D.E., Tran, H. & Moskal, T.E., 1994. Sootblower optimization. Part I: Fundamental hydrodynamics of a sootblower nozzle and jet. Tappi Journal, May 1994, Vol. 77: no.5.

23. Kaliazine, A.L., Piroozmand, F., Cormack, D.E. & Tran, H.N., 1997. Sootblower optimization. Part II: Deposit and sootblower interaction. Tappi Journal, November 1997, Vol. 80: no.11.

24. Koçak, M., Webster, S., Janosch, J.J., Ainsworth, R.A. & Koers, R., 2008. Fitness for service. Vol.1, Fracture, fatigue, creep, corrosion, p. 7-74.

25. Krotscheck, A. W. & Sixta, H., 2006. Recovery, in Sixta, Herbert ed., Handbook of Pulp. Wiley-VCH Verlag GmbH & Co. KGaA, Weinheim.

26. Mao, X., Tran, H. & Cormack, D.E., 2001a. Effects of chemical composition on the removability of recovery boiler fireside deposits. Tappi Journal, June 2001, Vol. 84: no.6.

27. Martikka, H., Pöllänen, I. & Simonen, J., 2006. Design of optimally safe recovery boilers against occurrence and consequences of internal explosion. SUSI 2006, pp. 227-236.

28. Martikka, H. & Pöllänen, I., 2015. Tube branch design with beam matrix dynamics. Machine design 2015, The monograph of faculty of technical sciences, University of Novi SAD.

29. Martikka, H., Pöllänen, I., Taitokari, E., 2005. Optimal design of fatigue loaded piping branch connections. Computer aided optimum design in Engineering IX, WIT Press, Southampton, Boston, pp. 391-400.

30. Miikkulainen, P., 2011. Measurement of sootblower jet strength in kraft recovery boilers- Part II: Results of the 3rd and 4th field trials. Peers, pp. 1051-1058.

31. Montgomery, D.C., Peck, E.A. & Vining, G.G., 2012. Introduction to linear regression analysis, fifth edition. A John Wiley & Sons, Inc., Publication, pp. 389-399.

32. Moskal, T.E., Bunton, M.A., Patel, R.L., 1997. Power Engineering JUN97, Vol. 101, Issue 6, p.51. ISSN: 00325961.

33. Murray, W.M. & Miller, W.R., 1992. The bonded electrical resistance strain gage. Oxford University Press 1992, pp. 241-242.

34. Nelson, W., Norton, C.L., Gardner, H.S., 1966. Final report (summary of the project) on the Combustion Engineering program for determining the nature of the and remedies for explosive reaction (s) between smelt and water in kraft chemical recovery furnaces to H. S. Gardner. Project 2419, final report, Windsor, Connecticut, Combustion Engineering, Inc., July 19, 1966, 15 p.

35. Nschokin, V., 1979. Engineering thermodynamics and heat transfer. Mir Publishers 1979, p. 395.

36. Ortega, C.R. & Bécar, C., 2008. Pre informe de inspección caldera recuperadora 261-22-001, Chile, pp. 1-3.

37. Penttinen, K., 2018. Master's thesis. Plugging of the recovery boiler, pp. 45-46.

38. Piersol, A.G. & Paez, T.L., 2010. Harri's Shock and Vibration Handbook, 6th edition, pp. 18.1.

39. Pophali, A., Emami, B., Bussmann, M., Tran, H., 2015. Studies on sootblower jet dynamics and ash deposit removal in industrial boilers. Fuel Processing Technology, p. 8.

40. Pöllänen, I., Björk, T. & Martikka, H., 2015. Warping of a tubular mat. Proceedings of the XII Finnish Mechanics Days, 2015.

41. Pöllänen, I., 2009. Beam joints under stress relaxation. Machine design 2009, The monograph of faculty of technical sciences, University of Novi SAD.

42. Radaj, D., Sonsino, C.M. & Fricke, W., 2006. Fatigue assessment of welded joints by local approaches. Woodhead publishing limited, Cambridge England, pp. 105-120.

43. Rao, S.S., 2011. The Finite Element Method in Engineering, 5th edition. Elsevier Inc., pp. 328-333.

44. Rao, S.S., 2007. Vibration of Continuous Systems. John Wiley & Sons, Inc.

45. Råde, L. & Westergren, B., 2001. Mathematics Handbook for Science and Engineering. Studentlitteratur, p. 92.

46. Schijve, J., 2009. Fatigue of Structures and Materials, Elsevier, Vol. 25, 2003, pp. 209-216.

47. Sinkkonen, A., 2011. Master's thesis. Evaluation of novel recovery boiler dust analyzer, pp. 88-104.

48. Svedin, K., Wallin, E., Ahlroth, M, 2008. Sootblowing methods and steam consumption in Swedish recovery boilers. Värmeforsk Service AB, Stockholm, pp. 84.

49. Tamminen, T.I., Kujanpää, J.I., Tikkanen, J.A. & Hupa, M.M., 2001. Continuous dust measurement as an indication of sootblowing performance in a recovery boiler. Tappi Journal, May 2001, Vol. 84: no.5.

50. Tandra, D. & Shah, S., 2010. Extended recovery boiler runtime using smart sootblower. Clyde- Bergemann, Inc. Atlanta, GA, USA.

51. Tandra, D. S., Manay, A. & Jones, A.K., 2010. Mill trial on new sootblower design and strategy to combat plugging in a recovery boiler. 2010 International Chemical Recovery Conference, March 29-April 1, Williamsburg, Virginia, USA.

52. Timoshenko, S.P. & Goodier, J.N., 2010. Theory of Elasticity, 3rd. edition. Mc Graw Hill, pp. 83-88.

53. Vakkilainen, E. K., 2006a. Kraft recovery boilers- High dry solids firing, pp. 4-1-4-6.

54. Vakkilainen, E. K., 2006b. Kraft recovery boilers- High dry solids firing, pp. 7-1-7-16.

55. Vakkilainen, E. K., 2006c. Kraft recovery boilers- High dry solids firing, pp. 7-1-6-15.

56. Välimäki, E., Salmenoja, K., 2004. Measured data for sootblowing optimization. ResearchGate. Conference Paper. November 2004, p.14.

57. Weaver, W. & Johnston, P.R., 1987. Structural Dynamics by Finite Elements. Prentice- Hall, Inc., Englewood Cliffs, New Jersey, pp. 105-106.

58. Window, A.L., 1992. Strain gauge technology. 2nd edition. Elsevier Applied Science, pp. 223- 228.

59. Ylinen, A., 1975. Strength of materials. Part II. Werner Söderström, pp. 517-521.

Appendix A: Measurement device

The following codes can be used to solve the stress values of the ring on the line A-A, stresses in the hanger rod and displacements between the clamps.

Initial data

Mid radius of the tension ring	$r := 31.425\,mm$
Ring thickness	$h := 2.15\,mm$
Ring width	$b := 25\,mm$
Young's modulus	$E := 206000\,MPa$
Diameter of the tension bar	$d := 6.0\,mm$
Lenght of the tension bar	$L_{bar} := 1000\,mm$
Axial force in the hanger rod	$F_{hr} := 61093.0\,N$
Diameter of the hanger rod	$d_{hr} := 25\,mm$

RESULTS (ring)

Ring cross section area

$$A_1 := h \cdot b = 53.75 \cdot mm^2 \tag{A.1}$$

Area moment of inertia of a weakly bent beam

$$I_1 := \int_{-\frac{h}{2}}^{\frac{h}{2}} \frac{y^2}{1 + \frac{y}{r}} \cdot b \, dy = 20.72 \cdot mm^4 \tag{A.2}$$

Spring constant for the ring

$$k_1 := \left[\frac{r^3}{E \cdot I_1} \cdot \left(\frac{\pi}{4} - \frac{2}{\pi} \right) \right]^{-1} = 924.44 \cdot \frac{N}{mm} \tag{A.3}$$

Spring constant for the tension bar

$$k_2 := \frac{E \cdot \pi \cdot d^2}{4 \cdot L_{bar}} = 5824.51 \cdot \frac{N}{mm} \tag{A.4}$$

Equivalent spring constant

$$k_{eq} := \left(\frac{1}{k_1} + \frac{1}{k_2} \right)^{-1} = 797.82 \cdot \frac{N}{mm} \tag{A.5}$$

Displacement between the clamps

$$\Delta_{hr} := \frac{4 \cdot F_{hr} \cdot L_{bar}}{E \cdot \pi \cdot d_{hr}^2} = 0.6 \cdot mm \tag{A.6}$$

Bending moment in the ring

$$M := \frac{1}{2} \cdot k_{eq} \cdot \Delta_{hr} \cdot r \cdot \left[1 - \frac{2}{\pi \cdot \left(1 + \frac{I_1}{A_1 \cdot r^2} \right)} \right] = 2.754 N \cdot m \tag{A.7}$$

Radial force on the ring

$$P := k_{eq} \cdot \Delta_{hr} = 482.01 \, N \tag{A.8}$$

Stress on the inner surface of the ring

$$\sigma_{inn} := \frac{0.5 \cdot P}{A_1} + \frac{M}{r \cdot A_1} - \frac{M}{I_1} \cdot \frac{\frac{h}{2}}{1 - \frac{\frac{h}{2}}{r}} = -141.8 \cdot MPa \tag{A.9}$$

Stress on the outer surface of the ring

$$\sigma_{out} := \frac{0.5 \cdot P}{A_1} + \frac{M}{r \cdot A_1} + \frac{M}{I_1} \cdot \frac{\frac{h}{2}}{1 - \frac{\frac{h}{2}}{r}} = 154.1 \cdot MPa \tag{A.10}$$

RESULTS (hanger rod)

Distance between the hanger rod and the tension bar

$$d_{hr\_bar} := 38.5\,mm \tag{A.11}$$

Moment due to eccentric force

$$Mc := P \cdot d_{hr\_bar} = 18557.47 \cdot N \cdot mm \tag{A.12}$$

Distance between the support points in the hanger rod

$$L_{points\_hr} := 1700\,mm$$

Distance between the support point and the clamp

$$L_{clamp\_hr} := 1350\,mm$$

Factor

$$\alpha := \frac{L_{clamp\_hr}}{L_{points\_hr}} = 0.794 \tag{A.13}$$

Moment value at the clamp

$$Mco := Mc \cdot \alpha \cdot \left(4 - 9 \cdot \alpha + 6 \cdot \alpha^2\right) = 9383\,N \cdot mm \tag{A.14}$$

Final moment value

$$Mcv := Mco - Mc = -9175 \cdot N \cdot mm \tag{A.15}$$

Section modulus of the hanger rod

$$W_{hr} := \frac{\pi \cdot d_{hr}^{\,3}}{32} \tag{A.16}$$

Bending stresses in the hanger rod at the measured points

Point 1

$$\sigma_1 := \frac{4 \cdot F_{hr}}{\pi \cdot d_{hr}^{\,2}} + -\frac{4 \cdot P}{\pi \cdot d_{hr}^{\,2}} - \frac{Mcv}{W_{hr}} = 129.5\,MPa \tag{A.17}$$

Point 2

$$\sigma_2 := \frac{4 \cdot F_{hr}}{\pi \cdot d_{hr}^{\,2}} + -\frac{4 \cdot P}{\pi \cdot d_{hr}^{\,2}} + \frac{Mcv}{W_{hr}} = 117.5\,MPa \tag{A.18}$$

Equally spaced stress in the hanger rod

$$\frac{1}{2} \cdot (\sigma_1 + \sigma_2) = 123.5 \cdot MPa \tag{A.19}$$

RESULTS (displacements between the clamps)

The bending moment Mc causes rotation at the connection point of the clamp. It follows that the ends of the clamps bend towards each other. This effect can be calculated by the following script.

Cross section area of the hanger rod $A = \frac{1}{4}\pi d_{hr}^2$

Area moment of inertia of the hanger rod $I = \frac{\pi d_{hr}^4}{64}$

Element lengths $L = (230 \quad 250 \quad 250 \quad 250 \quad 250 \quad 410)$

The stiffness matrix for one beam element, including the effect of the axial force and bending moment (Rao, 2011)

$$\text{genK}(E,A,L,I) := \begin{pmatrix} \frac{A\cdot E}{L} & 0 & 0 & -\frac{A\cdot E}{L} & 0 & 0 \\ 0 & \frac{12\cdot E\cdot I}{L^3} & \frac{6\cdot E\cdot I}{L^2} & 0 & -\frac{12\cdot E\cdot I}{L^3} & \frac{6\cdot E\cdot I}{L^2} \\ 0 & \frac{6\cdot E\cdot I}{L^2} & \frac{4\cdot E\cdot I}{L} & 0 & -\frac{6\cdot E\cdot I}{L^2} & \frac{2\cdot E\cdot I}{L} \\ -\frac{A\cdot E}{L} & 0 & 0 & \frac{A\cdot E}{L} & 0 & 0 \\ 0 & -\frac{12\cdot E\cdot I}{L^3} & -\frac{6\cdot E\cdot I}{L^2} & 0 & \frac{12\cdot E\cdot I}{L^3} & -\frac{6\cdot E\cdot I}{L^2} \\ 0 & \frac{6\cdot E\cdot I}{L^2} & \frac{2\cdot E\cdot I}{L} & 0 & -\frac{6\cdot E\cdot I}{L^2} & \frac{4\cdot E\cdot I}{L} \end{pmatrix} \tag{A.20}$$

Input data for elements

$$\begin{aligned} k_1 &:= \text{genK}\left(E,A,L_{1,1},I\right) & k_2 &:= \text{genK}\left(E,A,L_{1,2},I\right) \\ k_3 &:= \text{genK}\left(E,A,L_{1,3},I\right) & k_4 &:= \text{genK}\left(E,A,L_{1,4},I\right) \\ k_5 &:= \text{genK}\left(E,A,L_{1,5},I\right) & k_6 &:= \text{genK}\left(E,A,L_{1,6},I\right) \end{aligned} \tag{A.21}$$

The global stiffness matrix can be composed by using the script below

$$\begin{aligned} &K_{\text{global}}(n) := \left| \begin{array}{l} \text{mat} \leftarrow 0 \\ \quad \text{for } i \in 0..n-1 \\ \quad\quad \text{for } y \in 1..6 \\ \quad\quad\quad \text{for } x \in 1..6 \\ \quad\quad\quad\quad kx \leftarrow x + (3i) \\ \quad\quad\quad\quad ky \leftarrow y + (3i) \\ \quad\quad\quad\quad \text{mat}_{kx,ky} \leftarrow \text{mat}_{kx,ky} + \left[k_{(i+1)}\right]_{x,y} \\ \text{mat} \end{array} \right. \\ &\qquad \text{mat} \in \left(\text{rows}(k_1)+(n-1)\cdot\frac{\text{rows}(k_1)}{2}\right)^2 \end{aligned} \tag{A.22}$$

$KG := K_{global}(rows(k))$

"0" removes *i* th row and column from global stiffness matrix **KG**

$cV := (0\ 0\ 0\ 1\ 1\ 1\ 1\ 1\ 1\ 1\ 1\ 1\ 1\ 1\ 1\ 1\ 1\ 1\ 0\ 0)$

```
gauss_elimination(kM) := | y ← 1
                         | for k ∈ 1..rows(kM)
                         |     changeRow ← "false"
                         |     x ← 1
                         |     for j ∈ 1..cols(kM)
                         |         setValue ← "true" if cV_{1,k} = 1 ∧ cV_{1,j} = 1
                         |         setValue ← "false" otherwise
                         |         if setValue = "true"
                         |             reducedMatrix_{y,x} ← kM_{k,j}
                         |             x ← x + 1
                         |             changeRow ← "true"
                         |     y ← y + 1 if changeRow = "true"
                         | reducedMatrix
```

$GKG := gauss\_elimination(KG)$

Load vector includes the axial force $F_{hr} = 61093$ N and bending moment $Mc = 18392.3$ Nmm due to eccentric force

$LV := (0\ \ 0\ \ 18392.3\ 0\ \ 0\ \ 0\ \ 0\ \ 0\ \ 0\ \ 0\ \ 0\ \ 0\ \ 0\ \ 0\ \ -18392.3\ 61093)$

Displacements and rotations of the nodes are obtained from the equation

$$\boldsymbol{u = GKG^{-1}LV}$$

$$\boldsymbol{u} = \{0.139 \quad 0.097 \quad 8.351 \cdot 10^{-4} \quad , \quad , \quad , \quad 0.172 \quad -8.73 \cdot 10^{-4} \quad 0.987\}$$

The values $8.351 \cdot 10^{-4}$ and $-8.73 \cdot 10^{-4}$ represent angular rotation of the clamps. The vertical displacement is obtained by multiplying the rotation angle and the distance h_{hr_bar}, thus the total vertical displacement due to rotation is

$$Disp = 2 \cdot 8.351 \cdot 10^{-4} \cdot 38.5 \text{ mm} = 0.064 \text{ mm}$$

For comparison, Equation A.6 gives the result 0.6 mm for the straight hanger rod, which is subjected to axial force only.

Appendix B: Equivalent constant moment

The matrices below represent results from the dynamic analyses of the heat transfer surface. The dimensions and loadings of the structure are according to Paragraph 5.1. The $\Delta M -$ matrix includes values of the bending moments in the tube joint, obtained by the Rainflow counting method (Næss, 1999) and the $n -$ matrix the number of fatigue cycles, respectively.

$$\Delta M := \begin{pmatrix} 9621.567263 & 16583.31758 & 14921.18126 \\ 28864.58092 & 49542.73275 & 44763.42292 \\ 48107.59457 & 82502.14792 & 74605.66457 \\ 67350.60822 & 115461.5631 & 104447.9062 \\ 86593.62187 & 148420.9783 & 134290.1479 \\ 105836.6355 & 181380.3934 & 164132.3895 \\ 125079.6492 & 214339.8086 & 193974.6312 \\ 144322.6628 & 247299.2238 & 223816.8728 \\ 163565.6765 & 280258.6389 & 253659.1145 \\ 182808.6901 & 313218.0541 & 283501.3561 \\ 202051.7038 & 346177.4693 & 313343.5978 \\ 221294.7174 & 379136.8844 & 343185.8394 \\ 240537.7311 & 412096.2996 & 373028.0811 \\ 259780.7447 & 445055.7148 & 402870.3227 \\ 279023.7584 & 478015.1299 & 432712.5644 \\ 298266.772 & 510974.5451 & 462554.806 \\ 317509.7857 & 543933.9603 & 492397.0477 \\ 336752.7993 & 576893.3754 & 522239.2893 \\ 355995.813 & 609852.7906 & 552081.531 \\ 375238.8267 & 642812.2058 & 581923.7727 \\ 394481.8403 & 675771.6209 & 611766.0143 \\ 413724.854 & 708731.0361 & 641608.256 \\ 432967.8676 & 741690.4513 & 671450.4976 \\ 452210.8813 & 774649.8664 & 701292.7393 \\ 471453.8949 & 807609.2816 & 731134.9809 \\ 490696.9086 & 840568.6968 & 760977.2226 \\ 509939.9222 & 873528.1119 & 790819.4642 \\ 529182.9359 & 906487.5271 & 820661.7059 \\ 548425.9495 & 939446.9423 & 850503.9475 \\ 567668.9632 & 972406.3574 & 880346.1892 \end{pmatrix} \qquad n := \begin{pmatrix} 239.5 & 158 & 99 \\ 106.5 & 102 & 114.5 \\ 60 & 55 & 53 \\ 30.5 & 42 & 24.5 \\ 21 & 37.5 & 16 \\ 10 & 24.5 & 12 \\ 7 & 14.5 & 14 \\ 9.5 & 14 & 7.5 \\ 3 & 11.5 & 7.5 \\ 2.5 & 7.5 & 6.5 \\ 7 & 3.5 & 8.5 \\ 3 & 5 & 1.5 \\ 3.5 & 1.5 & 1 \\ 4.5 & 6 & 4 \\ 2.5 & 3 & 4 \\ 0.5 & 1 & 2.5 \\ 3 & 1 & 0.5 \\ 1 & 0 & 5 \\ 0.5 & 1.5 & 0.5 \\ 0 & 3 & 0 \\ 0 & 0 & 2 \\ 1 & 0 & 2.5 \\ 0.5 & 0.5 & 1.5 \\ 3 & 0 & 1 \\ 0.5 & 0.5 & 1 \\ 0 & 1.5 & 1 \\ 0.5 & 0.5 & 1.5 \\ 0 & 0.5 & 0 \\ 0.5 & 0 & 0 \\ 0.5 & 1.5 & 1 \end{pmatrix}$$

The value of the equivalent constant amplitude moment can be calculated for each case as follows:

Sequence 1

$$\left[\frac{\sum_{i=1}^{rows(n)}\left[\left(\Delta M_{i,1}\right)^{m}\cdot n_{i,1}\right]}{\sum_{i=1}^{rows(n)} n_{i,1}}\right]^{\frac{1}{m}} = 133421 \tag{B.1}$$

Sequence 2

$$\left[\frac{\sum_{i=1}^{rows(n)}\left[\left(\Delta M_{i,2}\right)^{m}\cdot n_{i,2}\right]}{\sum_{i=1}^{rows(n)} n_{i,2}}\right]^{\frac{1}{m}} = 246781 \tag{B.2}$$

Sequence 3

$$\left[\frac{\sum_{i=1}^{rows(n)}\left[\left(\Delta M_{i,3}\right)^{m}\cdot n_{i,3}\right]}{\sum_{i=1}^{rows(n)} n_{i,3}}\right]^{\frac{1}{m}} = 259106 \tag{B.3}$$

where $m = 3.0$ is a material parameter.

Appendix C: Strain calculations by strain gages

The tension ring is subjected to the force F_r and bending moment M_o (see Figure 4.5), which cause elongations to the strain gages on the outer and inner surfaces of the ring. On the outer surface the elongation is

$$\Delta L_{os} = \Delta L_{F_r} + \Delta L_{M_o} \tag{C.1}$$

and on the inner surface

$$\Delta L_{is} = \Delta L_{F_r} - \Delta L_{M_o} \tag{C.2}$$

In the wire, inside the strain gage, the change between the resistance and elongation is linear (Murray, et al.,1992), that is

$$GF = \frac{\frac{\Delta R}{R}}{\frac{\Delta L}{L}} \tag{C.3}$$

where R is the resistance of the strain gage, L is the length of the grid, and GF is the gage factor.

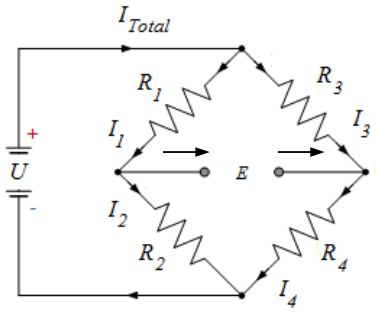

Figure C.1: The Wheatstone bridge circuit.

Using Kirchhoff's current and voltage laws for the Wheatstone bridge, the output voltage E can be written as

$$E = \left[\frac{R_3}{R_3 + R_4} - \frac{R_1}{R_1 + R_2}\right] U \tag{C.4}$$

which after rearranging terms becomes

$$E = \frac{U}{(R_3 + R_4)(R_1 + R_2)}[R_3R_2 - R_1R_4]$$

When the bridge is at balance, i.e., E = 0, one gets the condition $R_3R_2 = R_1R_4$. The output voltage E is a function of four resistances

$$E = f(R_1, R_2, R_3, R_4,)U \tag{C.5}$$

The differential change of E due to changes in R's is

$$dE = \left[\frac{\partial f}{\partial R_1}dR_1 + \frac{\partial f}{\partial R_2}dR_2 + \frac{\partial f}{\partial R_3}dR_3 + \frac{\partial f}{\partial R_4}dR_4\right] U \tag{C.6}$$

Substitution of f here gives for the change of the output voltage E

$$dE = \sum_{i=1}^{4}\left[\frac{\partial}{\partial R_i}\left(\frac{R_3}{R_3 + R_4} - \frac{R_1}{R_1 + R_2}\right)dR_i\right]U \tag{C.7}$$

In the vicinity of the balanced state of the bridge, this may be rearranged to show the sensitivities as

$$dE = \frac{R_2R_1}{(R_1 + R_2)^2}\left[\frac{dR_1}{R_1} - \frac{dR_2}{R_2} + \frac{dR_3}{R_3} - \frac{dR_4}{R_4}\right]U \tag{C.8}$$

Denote the first factor by the symbol H

$$H = \frac{R_2R_1}{(R_1 + R_2)^2} = \frac{r}{(1 + r)^2} \qquad \left(r = \frac{R_2}{R_1}\right) \tag{C.9}$$

The maximum of H is obtained by setting

$$\frac{dH}{dr} = \frac{1}{(1 + r)^2}\left[1 - \frac{2r}{1 + r}\right] = 0 \tag{C.10}$$

from which the maximal sensitivity is obtained at

$$r = 1 \Rightarrow H = \frac{1}{(1 + 1)^2} = \frac{1}{4} \tag{C.11}$$

Now Eq. (C.8) becomes

$$dE = \frac{1}{4}\left[\frac{dR_1}{R_1} - \frac{dR_2}{R_2} + \frac{dR_3}{R_3} - \frac{dR_4}{R_4}\right]U \tag{C.12}$$

The gages measure strain at the outer tensile surface and at the inner compressive surface of the ring. The strain gages R_1 and R_3 at the outer surface give the strain

$$\varepsilon_1 = \varepsilon_3 = \frac{\Delta L_{F_r}}{L} + \frac{\Delta L_{M_o}}{L} = \varepsilon_N + \varepsilon_M \tag{C.13}$$

The strain gages R_2 and R_4 at the inner surface give the strain

$$\varepsilon_2 = \varepsilon_4 = \frac{\Delta L_{F_r}}{L} - \frac{\Delta L_{M_o}}{L} = \varepsilon_N - \varepsilon_M \tag{C.14}$$

The resistance change in a strain gage due to strain in its wire is

$$\frac{dR}{R} = GF\ \varepsilon \tag{C.15}$$

Now the output voltage change of the Wheatstone bridge depends on the measured strains as

$$dE = \frac{GF}{4}[\ \varepsilon_1 - \varepsilon_2 + \varepsilon_3 - \varepsilon_4]U \tag{C.16}$$

Substituting Eqs. (C13) and (C14) above gives

$$dE = \frac{GF}{4}[\ 4\varepsilon_M\ ]U = \quad GF\ \cdot U \cdot \varepsilon_M \tag{C.17}$$

This shows that the measured change *dE* depends only on the strain due to bending of the ring and not on the normal strains. The stress value due to bending in the middle of the line A-A on the outer surface of the ring, i.e., at the critical point, is obtained approximately by multiplying the strain value ε_M, from the DAQ, by the Young's modulus.

Appendix D: Dynamic behavior of the platen

1. Natural frequency analysis of the platen

The free vibration of the undamped system is governed by the equation

$$\big[[k]-\omega^2[m]\big]\{X\}=\{0\} \tag{D.1}$$

where $\{X\}$ is the eigenvector corresponding to the natural frequency ω, $[k]$ is the stiffness matrix and $[m]$ the mass matrix. For a nontrivial solution of the eigenvector $\{X\}$, the determinant of the coefficient matrix must be equal to zero:

$$det\big[[k]-\omega^2[m]\big]=0 \tag{D.2}$$

Eq. (D.2) is a polynomial equation of nth degree in ω^2. The roots of this equation give n eigenvalues, $\omega_1^2, \omega_2^2, \dots, \omega_n^2$. The positive square roots of the eigenvalues yield the natural angular frequencies of the system (Rao, 2007). In many cases the natural frequencies of the platen can be solved by using 2D elements of the FEM. The required stiffness and mass matrices for the bending mode are (Weaver, et.al.,1987):

$$[k_b]=\frac{2EI}{L^3}\begin{bmatrix}6 & 3L & -6 & 3L\\ 3L & 2L^2 & -3L & L^2\\ -6 & -3L & 6 & -3L\\ 3L & L^2 & -3L & 2L^2\end{bmatrix} \tag{D.3}$$

and

$$[m_b]=\frac{\rho AL}{420}\begin{bmatrix}156 & 22L & 54 & -13L\\ 22L & 4L^2 & 13L & -3L^2\\ 54 & 13L & 156 & -22L\\ -13L & -3L^2 & -22L & 4L^2\end{bmatrix} \tag{D.4}$$

The torsion mode consists of the free torsion (i.e., Saint- Venant's torsion) and restrained warping torsion. The stiffness and mass matrices can be formed using the strain and kinetic energies. The total strain energy of the beam is

$$\Pi=\frac{1}{2}\int_0^L\left[E\cdot J_\omega\cdot\left(\frac{d^2\varphi}{dx^2}\right)^2+G\cdot I_p\cdot\left(\frac{d\varphi}{dx}\right)^2\right]dx \tag{D.5}$$

where φ is the angle of twist, I_p the second moment of area and J_ω the warping constant. The angle of twist can be presented as

$$\varphi = \boldsymbol{N}\boldsymbol{u} = [N_1 \quad N_2 \quad N_3 \quad N_4]\begin{bmatrix} u_1 \\ u_2 \\ u_3 \\ u_4 \end{bmatrix} \tag{D.6}$$

where N_1,..., N_4 are the shape functions and u_1,..., u_4 the node displacements and rotations. The shape functions are

$$N_1 = 1 - 3 \cdot \frac{x^2}{L^2} + 2 \cdot \frac{x^3}{L^3}, N_2 = x - 2 \cdot \frac{x^2}{L} + \frac{x^3}{L^2}, N_3 = 3 \cdot \frac{x^2}{L^2} - 2 \cdot \frac{x^3}{L^3}, N_4 = \frac{x^3}{L^2} - \frac{x^2}{L}$$

The $\boldsymbol{u}$ vector includes the unknown displacements and rotations. Substituting the angle of twist into Equation (D.5) we get

$$\Pi_{strain} = \frac{1}{2}\int_0^L \left(E \cdot J_\omega \cdot \boldsymbol{u}^T \boldsymbol{N}''^T \boldsymbol{N}'' \boldsymbol{u} + G \cdot I_p \cdot \boldsymbol{u}^T \boldsymbol{N}'^T \boldsymbol{N}' \boldsymbol{u}\right) dx \tag{D.7}$$

After calculations the stiffness matrices can be identified as

$$[k_{torsion}] = \frac{G \cdot I_p}{30 \cdot L}\begin{bmatrix} 36 & 3L & -36 & 3L \\ 3L & 4L^2 & -3L & -L^2 \\ -36 & -3L & 36 & -3L \\ 3L & -L^2 & -3L & 4L^2 \end{bmatrix} \tag{D.8}$$

and

$$\left[k_{warping}\right] = \frac{E \cdot J_\omega}{L}\begin{bmatrix} \frac{12}{L^2} & \frac{6}{L} & -\frac{12}{L^2} & \frac{6}{L} \\ \frac{6}{L} & 4 & -\frac{6}{L} & 2 \\ -\frac{12}{L^2} & -\frac{6}{L} & \frac{12}{L^2} & -\frac{6}{L} \\ \frac{6}{L} & 2 & -\frac{6}{L} & 4 \end{bmatrix} \tag{D.9}$$

The mass matrices for the free and restrained warping can be composed in a similar way. The corresponding kinetic energy is

$$\Pi_{kinetic} = \frac{1}{2}\int_0^L \left(J_\omega \cdot \left(\frac{d\dot{\varphi}}{dx}\right)^2 + I_p \cdot \dot{\varphi}^2 \right) \rho dx \tag{D.10}$$

After the appropriate manipulations, the mass matrices become

$$[m_{torsion}] = \rho\, I_p \begin{bmatrix} \frac{13L}{35} & \frac{11L^2}{210} & \frac{9L}{70} & \frac{13L^2}{420} \\ \frac{11L^2}{210} & \frac{L^3}{105} & \frac{13L^2}{420} & \frac{L^3}{140} \\ \frac{9L}{70} & \frac{13L^2}{420} & \frac{13L}{35} & -\frac{11L^2}{210} \\ \frac{13L^2}{420} & -\frac{L^3}{140} & -\frac{11L^2}{210} & \frac{L^3}{105} \end{bmatrix} \tag{D.11}$$

and

$$[m_{warping}] = \rho\, J_\omega \begin{bmatrix} \frac{6}{5L} & \frac{1}{10} & -\frac{6}{5L} & \frac{1}{10} \\ \frac{1}{10} & \frac{2L}{15} & -\frac{1}{10} & -\frac{L}{30} \\ -\frac{6}{5L} & -\frac{1}{10} & \frac{6}{5L} & -\frac{1}{10} \\ \frac{1}{10} & -\frac{L}{30} & -\frac{1}{10} & \frac{2L}{15} \end{bmatrix} \tag{D.12}$$

2. Transient response analysis of the platen

The platen is subjected to an excitation that changes with time, thus the solution is also time-varying. When the excitation is explicitly available in the time domain, the transient response analysis is suitable for this problem. For an *n*-degree of freedom system, the general equation of motion is (Adams, et al., 1999)

$$[m]\ddot{x} + [c]\dot{x} + [k]x = f(t) \tag{D.13}$$

where [*c*] is the damping matrix. The overall damping of the structure is difficult to obtain and the only accurate way to determine it is by experiment. In the book by R.D. Blevins (2001) some damping values for different structures are presented. An average value for the tube heat exchanger is 0.0169. Using the model of proportional damping, the damping matrix can be composed as

$$[c] = \alpha[m] + \beta[k] \tag{D.14}$$

where α and β are unknown coefficients, which can be solved as presented in Finite Element Procedures by K.J. Bathe (1996). Equation D.13 can be solved using different methods. A well-known method is direct numerical integration (Chapra & Canale, 2006).

On the next pages a closed form solution for the warping constant J_ω is derived. The result is valid for the cross section of the heat surface which consists of tubes and fins.

When a circular tube is subjected to a torque, each cross section of the tube rotates in its own plane without warping and axial stresses do not occur. This assumption of planarity is not valid when two or more tubes connected by fins are considered. If one or both ends of the structure are restrained, a torque causes shear and axial stresses. At the restrained end the restrained torque is more significant relative to the St Venant torque. At the loaded end, where the warping can occur freely, the restrained torque is zero and the St Venant torque dominates. In Figure D.1 the effect of the restrained torsion in the case of two tubes connected by a fin is illustrated.

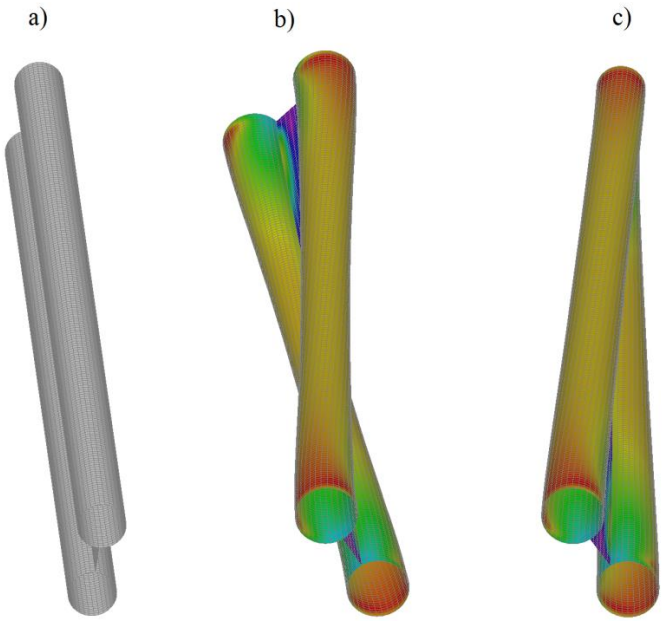

Figure D.1: (a) Undeformed shape, (b) free torsion and (c) restrained torsion of two tubes connected by a fin.

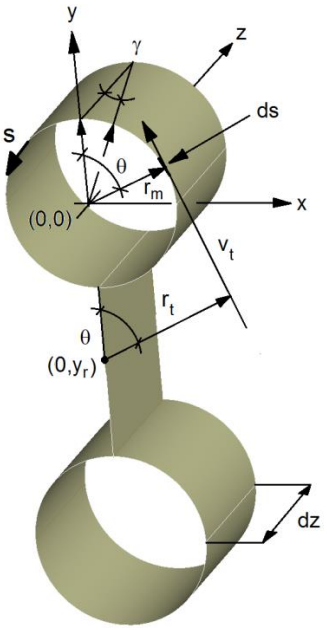

Figure D.2: Simplified model for two tubes and one fin.

Referring to Figure D.2, for a tube circle line element *ds* two relations are obtained

$$\gamma = r_m \frac{d\theta}{dz} \tag{D.15}$$

$$dv_t = r_t d\theta \tag{D.16}$$

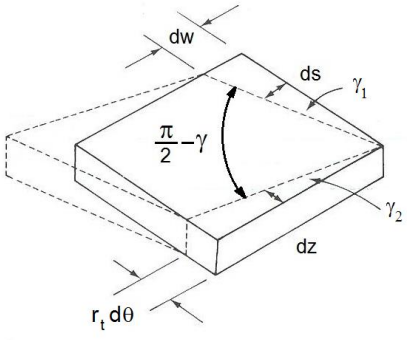

Figure D.3 Tangential and axial components of displacement.

The shear strain becomes

$$\gamma_{sz} = \gamma_1 + \gamma_2 = \frac{dw}{ds} + \frac{r_t\, d\theta}{dz} \tag{D.17}$$

Substituting Equations (D.15) and (D.16) into Equation (D.17) gives

$$\frac{dw}{ds} = r_m \frac{d\theta}{dz} - r_t \frac{d\theta}{dz} \tag{D.18}$$

which after simplifying and rearranging gives

$$dw = -\frac{d\theta}{dz}\left(r_t - r_m\right) ds \tag{D.19}$$

The arc length ds can be expressed in terms of r_m and $d\beta$

$$ds = r_m d\beta \tag{D.20}$$

Substituting Equation (D.20) into (D.19) leads to

$$dw = -\frac{d\theta}{dz}\left(r_t - r_m\right) r_m d\beta \tag{D.21}$$

Integration of both sides with respect to *s* and β gives

$$\int_s dw = -\frac{d\theta}{dz} \int_\beta \left(r_t - r_m\right) r_m d\beta \tag{D.22}$$

The primary warping function is defined as

$$\omega_s = \int_\beta \left(r_t - r_m\right) r_m d\beta + \omega_0 \tag{D.23}$$

The equation of the tube cross section is

$$x^2 + y^2 = r_m^2 \rightarrow y = \pm\sqrt{r_m{}^2 - x^2} \tag{D.24}$$

Differentiating Equation (D.24) with respects to *x* gives for the upper half of the circle

$$\frac{dy}{dx} = -\frac{x}{\sqrt{r_m{}^2 - x^2}} \equiv k \tag{D.25}$$

The equation for a tangent line is

$$y = kx + b \tag{D.26}$$

standard form of which is

$$kx - y + b = 0 \tag{D.27}$$

Using the notations $A = k,\ B = -1$ and $C = b,$ the distance from the point (0,0) to the tangent line is

$$r_m = \frac{|A \cdot 0 + B \cdot 0 + b|}{\sqrt{A^2 + B^2}} = \frac{|b|}{\sqrt{k^2 + 1}} \tag{D.28}$$

From Equation (D.28)

$$b = r_m \cdot \sqrt{k^2 + 1} = r_m \cdot \sqrt{\left(-\frac{x}{\sqrt{r_m{}^2 - x^2}}\right)^2 + 1} = r_m \cdot \sqrt{\frac{x^2}{r_m{}^2 - x^2} + 1}$$

$$= r_m \cdot \sqrt{\frac{r_m{}^2 \cdot \cos^2\beta}{r_m{}^2 - r_m{}^2 \cdot \cos^2\beta} + 1} = r_m \cdot \sqrt{\frac{\cos^2\beta}{\sin^2\beta} + 1} = \frac{r_m}{\sin\beta} \tag{D.29}$$

The distance from the point $(0, y_r)$ to the tangent line is $(y_r < 0)$

$$r_t = \frac{|A \cdot 0 + B \cdot y_r + b|}{\sqrt{A^2 + B^2}} = \frac{|-y_r + b|}{\sqrt{k^2 + 1}} \tag{D.30}$$

Now r_t can be determined for the upper half of the circle

$$\frac{r_m}{r_t} = \frac{|b|}{|-y_r + b|} = \frac{\frac{r_m}{\sin\beta}}{-y_r + \frac{r_m}{\sin\beta}} \quad \rightarrow \quad r_{t1}(\beta) = r_m - y_r \sin\beta \tag{D.31}$$

The lower half of the circle is treated by taking care of the sign of the terms. By squaring both sides of Equation (D.31) and rearranging terms, we obtain

$$r_t = \sqrt{\frac{r_m^{\,2} \cdot \left(-y_r + \frac{r_m}{\sin\beta} \right)^2}{\frac{r_m^{\,2}}{\sin^2\beta}}} = \sqrt{\left(-y_r \cdot \sin\beta + r_m \right)^2} = \left| -y_r \cdot \sin\beta + r_m \right|$$

that is

$$r_{t2}(\beta) = \left| r_m - y_r \cdot \sin\beta \right| \tag{D.32}$$

The value of r_{t2} must be greater than or equal to zero and it has two zero points. The corresponding angle β can be solved from Equation (D.32)

$$r_m - y_r \cdot \sin\beta = 0 \;\rightarrow\; \beta = \arcsin\frac{r_m}{y_r} \tag{D.33}$$

Now the integration around the full circle can be done by using the following intermediate values of the angle β

$$\beta_0 = -\frac{\pi}{2},\ \beta_1 = \arcsin\frac{r_m}{y_r},\ \beta_2 = 0,\ \beta_3 = \frac{\pi}{2},\ \beta_4 = \pi,\ \beta_5 = \pi - \beta_1 \text{ and } \beta_6 = \frac{3\cdot\pi}{2}$$

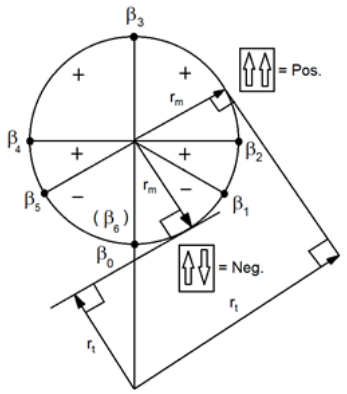

Figure D.4: Integration intervals along the tube.

The integration around the tube circle will be done in parts according to the following rule:

The variable r_t is positive (negative) if a vector along the tangent in the direction of increasing s acts counterclockwise (clockwise) about the shear center. The result of this rule is illustrated in Figure D.4.

$$\begin{aligned}
\omega_{s1}(\beta) &= \int_{\beta_0}^{\beta} (-r_{t2} - r_m) r_m d\beta + \omega_0 \\
\omega_{s2}(\beta) &= \int_{\beta_1}^{\beta} (+r_{t2} - r_m) r_m d\beta + \omega_{s1}(\beta_1) \\
\omega_{s3}(\beta) &= \int_{\beta_2}^{\beta} (+r_{t1} - r_m) r_m d\beta + \omega_{s2}(\beta_2) \\
\omega_{s4}(\beta) &= \int_{\beta_3}^{\beta} (+r_{t1} - r_m) r_m d\beta + \omega_{s3}(\beta_3) \\
\omega_{s5}(\beta) &= \int_{\beta_4}^{\beta} (+r_{t2} - r_m) r_m d\beta + \omega_{s4}(\beta_4) \\
\omega_{s6}(\beta) &= \int_{\beta_5}^{\beta} (-r_{t2} - r_m) r_m d\beta + \omega_{s5}(\beta_5)
\end{aligned} \tag{D.34}$$

The value of r_t has to be always positive, i.e., the blue line in Figure D.5.

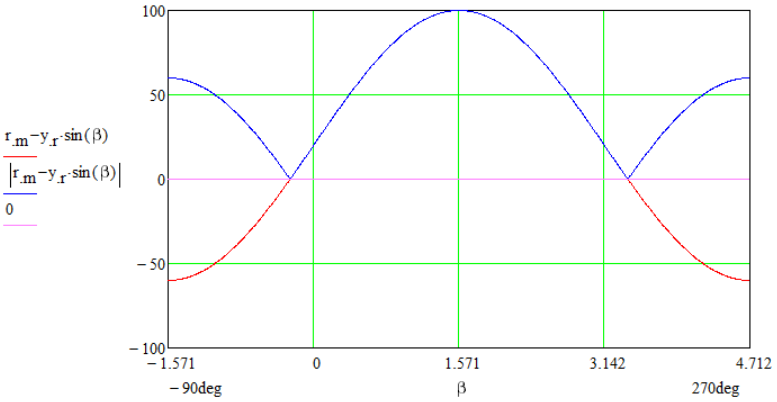

Figure D.5: Values of the length r_t as a function of the angle β.

By substituting the results of Equations (D.31) and (D.32) into Equation (D.34) we obtain

$$\omega_{s1}(\beta)=\int_{\beta_0}^{\beta}(-r_{t2}-r_m)r_m d\beta+\omega_0=$$
$$\int_{\beta_0}^{\beta}\left[-(-r_m+y_r\cdot\sin\beta)-r_m\right]r_m d\beta+\omega_0= \qquad \text{(D.35)}$$
$$\int_{\beta_0}^{\beta}-y_r\cdot r_m\cdot\sin\beta\, d\beta+\omega_0$$

$$\omega_{s2}(\beta)=\int_{\beta_1}^{\beta}(+r_{t2}-r_m)r_m d\beta+\omega_{s1}(\beta_1)=$$
$$\int_{\beta_1}^{\beta}(r_m-y_r\cdot\sin\beta-r_m)r_m d\beta+\omega_{s1}(\beta_1)= \qquad \text{(D.36)}$$
$$\int_{\beta_1}^{\beta}-y_r\cdot r_m\cdot\sin\beta d\beta+\omega_{s1}(\beta_1)$$

$$\omega_{s3}(\beta)=\int_{\beta_2}^{\beta}(+r_{t1}-r_m)r_m d\beta+\omega_{s2}(\beta_2)=$$
$$\int_{\beta_2}^{\beta}(r_m-y_r\cdot\sin\beta-r_m)r_m d\beta+\omega_{s2}(\beta_2)= \qquad \text{(D.37)}$$
$$\int_{\beta_2}^{\beta}-y_r\cdot r_m\cdot\sin\beta d\beta+\omega_{s2}(\beta_2)$$

$$\omega_{s4}(\beta)=\int_{\beta_3}^{\beta}(+r_{t1}-r_m)r_m d\beta+\omega_{s3}(\beta_3)=$$
$$\int_{\beta_3}^{\beta}(r_m-y_r\cdot\sin\beta-r_m)r_m d\beta+\omega_{s3}(\beta_3)= \qquad \text{(D.38)}$$
$$\int_{\beta_3}^{\beta}-y_r\cdot r_m\cdot\sin\beta d\beta+\omega_{s3}(\beta_3)$$

$$\omega_{s5}(\beta)=\int_{\beta_4}^{\beta}(+r_{t2}-r_m)r_m d\beta+\omega_{s4}(\beta_4)=$$

$$\int_{\beta_4}^{\beta}(r_m-y_r\cdot\sin\beta-r_m)r_m d\beta+\omega_{s4}(\beta_4)= \qquad \text{(D.39)}$$

$$\int_{\beta_4}^{\beta}-y_r\cdot r_m\cdot\sin\beta d\beta+\omega_{s4}(\beta_4)$$

$$\omega_{s6}(\beta)=\int_{\beta_5}^{\beta}(-r_{t2}-r_m)r_m d\beta+\omega_{s5}(\beta_5)=$$

$$\int_{\beta_5}^{\beta}[-(-r_m+y_r\cdot\sin\beta)-r_m]r_m d\beta+\omega_{s5}(\beta_5)= \qquad \text{(D.40)}$$

$$\int_{\beta_5}^{\beta}-y_r\cdot r_m\cdot\sin\beta\, d\beta+\omega_{s5}(\beta_5)$$

The results of Equations (D.35 – D.40) can be reduced to one equation:

$$\omega_s(\beta)=\int_{\beta_0}^{\beta}-y_r\cdot r_m\cdot\sin\beta\, d\beta \qquad \text{(D.41)}$$

Integration of Equation (D.41) gives

$$\omega_s(\beta)=y_r\cdot r_m\cdot(\cos\beta-\cos\beta_0) \qquad \text{(D.42)}$$

At the junction of the fin and the tube $\beta_0=-\frac{\pi}{2}$ so that

$$\omega_s(\beta)=y_r\cdot r_m\cdot\cos\beta \qquad \text{(D.43)}$$

The result is presented graphically below.

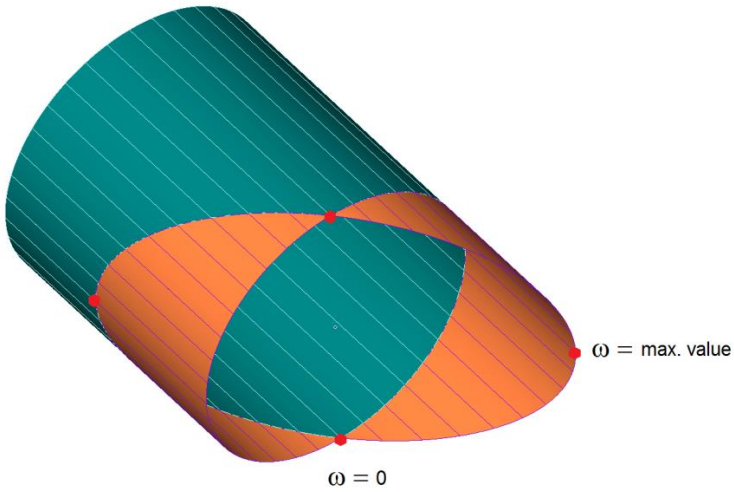

Figure D.7: Plotted ω-values for one tube. The parameter values used are $r_m = 1$ and $y_r = -1.1$.

According to the definition, the primary warping constant is

$$\Gamma_{1\_tube} = t\int_s \omega_s^2 ds \tag{D.44}$$

Substituting here from Equations (D.43) and (D.20) leads to

$$\Gamma_{1\_tube} = t\int_\beta \left(y_r \cdot r_m \cdot \cos\beta\right)^2 r_m \, d\beta \tag{D.45}$$

which after integration gives

$$\Gamma_{1\_tube} = \pi \cdot r_m^3 \cdot y_r^2 \cdot t \tag{D.46}$$

The secondary warping constant is defined as

$$\Gamma_{2\_tube} = \int_A \omega_n^2 \, dA \tag{D.47}$$

where

$$\omega_n = r_n \cdot n \tag{D.48}$$

The normal radius r_n can be calculated as

$$r_n = \begin{Vmatrix} \hat{i} & \hat{j} & \hat{k} \\ r_m \cdot \cos\beta & -y_r + r_m \cdot \sin\beta & 0 \\ \cos\beta & \sin\beta & 0 \end{Vmatrix} = \left| y_r \cdot \cos\beta \right| \tag{D.49}$$

Substituting Equation (D.49) into Equation (D.47) we obtain

$$\Gamma_{2\_tube} = \int_S \int_0^{\frac{t}{2}} n^2 \cdot y_r^2 \cdot \cos^2\beta \, dn ds = \int_{-\frac{\pi}{2}}^{0} \int_0^{\frac{t}{2}} r_m \cdot n^2 \cdot y_r^2 \cdot \cos^2\beta \, dn d\beta = \frac{\pi \cdot r_m \cdot t^3 \cdot y_r^2}{96} \tag{D.50}$$

This result is for one quarter of the circle and half of the tube wall thickness. Thus, the result must be multiplied by 8 leading to

$$\Gamma_{2\_tube} = 8 \cdot \frac{\pi \cdot r_m \cdot t^3 \cdot y_r^2}{96} = \frac{\pi \cdot r_m \cdot y_r^2 \cdot t^3}{12} \tag{D.51}$$

It can be shown that the primary warping constant of the fin is zero, but it has a non-zero secondary warping constant. This can be calculated in the same manner as for the tube, that is

$$\Gamma_{2\_fin} = \int_A \omega_n^2 \, dA \tag{D.52}$$

where

$$\omega_n = r_n \cdot n \tag{D.53}$$

The normal radius r_n can be calculated as

$$r_n = \begin{Vmatrix} \hat{i} & \hat{j} & \hat{k} \\ 0 & s & 0 \\ 1 & 0 & 0 \end{Vmatrix} = \left| s \right| \tag{D.54}$$

Substituting Equation (D.54) into Equation (D.52) we obtain

$$\Gamma_{2\_fin} = \int_0^h \int_0^{\frac{t}{2}} n^2 \cdot s^2 \cdot dn ds = \frac{h^3 t^3}{72} \tag{D.55}$$

This result is for half of the tube wall thickness. Thus, the result must be multiplied by two, which gives

$$\Gamma_{2\_fin} = \frac{h^3 \cdot t^3}{36} \tag{D.56}$$

Note that here h is half of the length of the whole fin between the two tubes. The warping constant J_ω can be written as

$$J_\omega = \Gamma_{1\_tube} + \Gamma_{2\_tube} + \Gamma_{1\_fin} + \Gamma_{2\_fin} \tag{D.57}$$

Finally, we can write the warping constant for one tube and half of a fin in the form

$$J_\omega = \pi \cdot r_m^3 \cdot y_r^2 \cdot t + \frac{\pi \cdot r_m \cdot y_r^2 \cdot t^3}{12} + \frac{h^3 \cdot t^3}{36} \tag{D.58}$$

This result can be easily generalized for a whole heat transfer surface containing n tubes and $n - 1$ fins.

ACTA UNIVERSITATIS LAPPEENRANTAENSIS

854. POPOVIC, TAMARA. Quantitative indicators of social sustainability applicable in process systems engineering. 2019. Diss.

855. RAMASAMY, DEEPIKA. Selective recovery of rare earth elements from diluted aqueous streams using N- and O –coordination ligand grafted organic-inorganic hybrid composites. 2019. Diss.

856. IFTEKHAR, SIDRA. Synthesis of hybrid bio-nanocomposites and their application for the removal of rare earth elements from synthetic wastewater. 2019. Diss.

857. HUIKURI, MARKO. Modelling and disturbance compensation of a permanent magnet linear motor with a discontinuous track 2019. Diss.

858. AALTO, MIKA. Agent-based modeling as part of biomass supply system research. 2019. Diss.

859. IVANOVA, TATYANA. Atomic layer deposition of catalytic materials for environmental protection. 2019. Diss.

860. SOKOLOV, ALEXANDER. Pulsed corona discharge for wastewater treatment and modification of organic materials. 2019. Diss.

861. DOSHI, BHAIRAVI. Towards a sustainable valorisation of spilled oil by establishing a green chemistry between a surface active moiety of chitosan and oils. 2019. Diss.

862. KHADIJEH, NEKOUEIAN. Modification of carbon-based electrodes using metal nanostructures: Application to voltammetric determination of some pharmaceutical and biological compounds. 2019. Diss.

863. HANSKI, JYRI. Supporting strategic asset management in complex and uncertain decision contexts. 2019. Diss.

864. OTRA-AHO, VILLE. A project management office as a project organization’s strategizing tool. 2019. Diss.

865. HILTUNEN, SALLA. Hydrothermal stability of microfibrillated cellulose. 2019. Diss.

866. GURUNG, KHUM. Membrane bioreactor for the removal of emerging contaminants from municipal wastewater and its viability of integrating advanced oxidation processes. 2019. Diss.

867. AWAN, USAMA. Inter-firm relationship leading towards social sustainability in export manufacturing firms. 2019. Diss.

868. SAVCHENKO, DMITRII. Testing microservice applications. 2019. Diss.

869. KARHU, MIIKKA. On weldability of thick section austenitic stainless steel using laser processes. 2019. Diss.

870. KUPARINEN, KATJA. Transforming the chemical pulp industry – From an emitter to a source of negative CO2 emissions. 2019. Diss.

871. HUJALA, ELINA. Quantification of large steam bubble oscillations and chugging using image analysis. 2019. Diss.

872. ZHIDCHENKO, VICTOR. Methods for lifecycle support of hydraulically actuated mobile working machines using IoT and digital twin concepts. 2019. Diss.

873. EGOROV, DMITRY. Ferrite permanent magnet hysteresis loss in rotating electrical machinery. 2019. Diss.

874. PALMER, CAROLIN. Psychological aspects of entrepreneurship – How personality and cognitive abilities influence leadership. 2019. Diss.

875. TALÁSEK, TOMÁS. The linguistic approximation of fuzzy models outputs. 2019. Diss.

876. LAHDENPERÄ, ESKO. Mass transfer modeling in slow-release dissolution and in reactive extraction using experimental verification. 2019. Diss.

877. GRÜNENWALD, STEFAN. High power fiber laser welding of thick section materials - Process performance and weld properties. 2019. Diss.

878. NARAYANAN, ARUN. Renewable-energy-based single and community microgrids integrated with electricity markets. 2019. Diss.

879. JAATINEN, PEKKO. Design and control of a permanent magnet bearingless machine. 2019. Diss.

880. HILTUNEN, JANI. Improving the DC-DC power conversion efficiency in a solid oxide fuel cell system. 2019. Diss.

881. RAHIKAINEN, JARKKO. On the dynamic simulation of coupled multibody and hydraulic systems for real-time applications. 2019. Diss.

882. ALAPERÄ, ILARI. Grid support by battery energy storage system secondary applications. 2019. Diss.

883. TYKKYLÄINEN, SAILA. Growth for the common good? Social enterprises' growth process. 2019. Diss.

884. TUOMISALO, TEEMU. Learning and entrepreneurial opportunity development within a Finnish telecommunication International Venture. 2019. Diss.

885. OYEDEJI, SHOLA. Software sustainability by design. 2019. Diss.

886. HUTTUNEN, MANU. Optimizing the specific energy consumption of vacuum filtration. 2019. Diss.

887. LIIKANEN, MIIA. Identifying the influence of an operational environment on environmental impacts of waste management. 2019. Diss.

888. RANTALA, TERO. Operational level performance measurement in university-industry collaboration. 2019. Diss.

889. LAUKKANEN, MINTTU. Sustainable business models for advancing system-level sustainability. 2019. Diss.

890. LOHRMANN, CHRISTOPH. Heuristic similarity- and distance-based supervised feature selection methods. 2019. Diss.

891. ABDULLAH, UMMI. Novel methods for assessing and improving usability of a remote-operated off-road vehicle interface. 2019. Diss.

ISBN 978-952-335-476-0
ISBN 978-952-335-477-7 (PDF)
ISSN-L 1456-4491
ISSN 1456-4491
Lappeenranta 2019